学位論文

Theoretical study on diversity and evolution of climate of Earth-like planets in habitable zone

(ハビタブルゾーンにおける地球類似惑星の
気候の多様性及び進化に関する理論的研究)

平成28年12月博士（理学）申請

東京大学大学院理学系研究科
地球惑星科学専攻

門屋 辰太郎

Abstract

The climate of the Earth is thought to have been warm throughout the history although the Earth is expected to be globally ice-covered owing to the low luminosity of the young Sun, assuming that the atmospheric composition is as same as that of the present Earth. This discrepancy is known as the "faint young Sun paradox". The key mechanism to resolve the paradox is the carbonate-silicate geochemical cycle which controls the atmospheric carbon dioxide and keeps the Earth warm with its negative feedback (the "Walker feedback"). However, recent studies revealed that the Walker feedback does not always work efficiently: for example, a CO_2 degassing rate of 10 times smaller than that at the present may cause the snowball Earth events. Hence, it is implied that there is a limit of application of the Walker feedback to maintain the Earth's climate warm, but the condition for the applicable limit is still unclear. In addition, global glaciations (snowball Earth events) occurred repeatedly in the Neoproterozoic, although the reason for that is uncertain. In this study, with a climate model coupled with a carbon cycle model, the limit of application for the Walker feedback mechanism of the Earth is investigated in terms of insolation (orbital semi-major axis) and a CO_2 degassing rate (index of internal activities of the Earth). In addition, the evolutionary track of the Earth is investigated based on the stellar and planetary thermal evolutions in order to reveal the reasons why the Earth has been warm throughout the history and also the snowball Earth events occurred repeatedly at the Neoproterozoic era.

Focusing on the hypothetical Earth orbiting within the habitable zone (HZ), the climate of the hypothetical Earth with the carbon cycle is classified into three climate modes: the warm climate, snowball cycle, and warm climate cycle modes. In the warm climate mode, the climate is controlled by the Walker feedback mechanism, and both the balances of energy and CO_2 are achieved. The climate of the Earth at present corresponds to this climate mode.

In other climate modes, the balance of CO_2 is not achieved, hence the climate is not in a steady state. The climate of the planet in the snowball cycle mode oscillates between the warm and snowball states. This is because there is no liquid water on the planetary surface, hence CO_2 should accumulate in the atmosphere without being consumed, and the snowball state would end finally owing to the greenhouse effect of dense CO_2 atmosphere. The climate is, however, not in a steady state because the CO_2 balance is not achieved, resulting in a decrease in $p\mathrm{CO}_2$ and surface temperature; the large ice-cap instability due to the ice-albedo feedback finally occurs owing to the decrease in surface temperature, resulting in a snowball state again.

There is another climate mode: the warm climate cycle mode in which the climate oscillates between ice-free and partially ice-covered states owing to imbalance of energy budget and the positive feedback caused by H_2O atmosphere.

At the critical condition between the warm climate and snowball cycle modes, $p\mathrm{CO}_2$ increases with a decrease in the insolation while the globally-averaged surface temperature stays around ~ 273 K. This relation between the insolation and the critical $p\mathrm{CO}_2$ depends mainly on the relation between $p\mathrm{CO}_2$ and the planetary radiation, which determines the critical CO_2 degassing rate between the warm and snowball cycle modes. Hence, the critical CO_2 degassing rate increases with a decrease in insolation, and the condition under which the Earth is in the warm climate mode is limited only to the part of the HZ especially when the CO_2 degassing rate is low: for example, when the CO_2 degassing rate is as much as that of the present Earth, more than 0.8 times of the present insolation is necessary for the Earth to be in the warm climate mode.

In addition, there are two different outer limits of the HZ: one is the minimum insolation at which the climate of the Earth is able to be in the warm climate mode, and the another is the minimum insolation at which the climate of the Earth is able to recover from the snowball state. These two different limits are caused by the difference in the surface albedos of the planet of the warm and snowball state, and a planet whose insolation is between these limits has hysteresis in its climate mode.

The Earth was in the warm climate mode owing to high CO_2 degassing rate which may relate to high mantle temperature in the past while the insolation was lower then. The Earth has been in the warm climate mode during the history

because a decrease in a CO_2 degassing rate due to the cooling of the planetary interior has been compensated by an increase in the insolation due to the evolution of the Sun. Continental growth (i.e., an increase in the continental size with time) would have been responsible for the warm climate mode Earth in the past. Considering the hypothetical Earth of which orbit is farther from the Sun than the real Earth, the warm climate has been maintained for the first several giga years owing to initially high CO_2 degassing rate, but it shifts to the snowball cycle mode owing to the decrease in the CO_2 degassing rate with time. The timescale of the shift to the snowball cycle mode depends mainly on the evolution of the CO_2 degassing rate, in other words, the evolution of the planet. This timescale is, therefore, roughly the same for the planets with different orbital semi-major axis in the outer HZ, and even when a type of the central star is different (i.e., the timescale of the stellar evolution is different). In the snowball cycle mode, the hypothetical Earth is more likely in the snowball state than in the warm climate state; therefore, the hypothetical Earth (i.e., an extra-solar Earth-like planet) in the outer HZ around old star is supposed to be observed as a snowball planet.

The Earth has been in the warm climate mode during its history as explained above. However, a certain perturbation to the carbon cycle system could have moved the Earth's climate to the snowball cycle mode. Comparing the critical condition between the warm and snowball cycle modes with the evolutionary track of the climate of the Earth on the diagram of the insolation and the CO_2 degassing rate, it is about 700 million years ago, which corresponds to the Neoproterozoic era in the Earth's history, that the conditional distance to the snowball cycle mode becomes minimum throughout the evolution of the Earth. This might explain the reason why the snowball Earth events repeated twice within a relatively short period of time (< 100 million years) during the Neoproterozoic, although, besides the Neoproterozoic snowball Earth events and another one event in the Paleoproterozoic, there is no other snowball Earth event occurred during the whole history of the Earth.

Acknowledgments

I express my sincere thanks to Prof. Eiichi Tajika for over 6 years of academic guidance. It is his insightful advice and encouragement that have led me to the completion of this study.

I wish to thank Dr. Y. Sekine, Prof. K. Kurita, Prof. K. Kuramoto, and Dr. M. Ikoma for their critical reviews and helpful comments. I gratefully acknowledge the research group at the University of Tokyo, Dr. M. Harada, Dr. H. Kuwahara, and Mr. Y. Chang for their discussion and fruitful advices. I sincerely thank Mr. T. Kodama, Mr. Y. Takao, Mr. Y. Watanabe, Mr. S. Fukushima, Mr. T. Fujita, Mr. Y. Ito, Mr. A. Nakayama, Mr. S. Kurokawa, and Ms. Y. Kawashima: I have received a lot of assistances, discussions, and friendship from them. I am grateful to Prof. J. F. Kasting, Dr. Y. Kanzaki, and the research group at the Pennsylvania State University for accepting and encouraging me.

I owe my deepest gratitude Mr. T. Suzuki, Mr. K. Yano, Ms. M. Sato, and Ms. M. Ishikawa: they give me warm encouragement. I also appreciate financial support by Grant-in-Aid for JSPS Research Fellow.

Finally, I would like to express the deepest appreciation to my family for their unceasing support and encouragement.

Contents

Section 1

Introduction

1.1 Earth climate system and the Walker feedback

The climate of the Earth has been warm sufficient to hold liquid water ocean on the surface throughout the history based on geological evidences (e.g., Nutman et al., 1984; Eriksson, 1982; Mojzsis et al., 2001; Wilde et al., 2001), although there are short episodes of snowball Earth events, that is, the Makganyene (2.34 billion years ago, or Ga), Sturtian (700 million years ago, or Ma), and Marinoan (650 Ma) glaciations (e.g., Kirschvink, 1992; Hoffman et al., 1998; Kirschvink et al., 2000; Hoffman and Schrag, 2002). On the other hand, according to the standard model of stellar evolution (e.g., Iben, 1967; Gough, 1981), the luminosity of the Sun has increased with time. If the atmospheric composition of the Earth (in other words, the amount of greenhouse gases) had been as same as that of today, the Earth would have been globally ice-covered (i.e., a snowball state) in the past owing to the low luminosity. This problem has been known as the "faint young Sun paradox" (e.g., Sagan and Mullen, 1972). The faint young Sun paradox can be resolved if the amounts of some greenhouse gases such as carbon dioxide (CO_2), methane (CH_4) and ammonia are larger than those of today (e.g., Sagan and Mullen, 1972). The large amounts of greenhouse gases in the past, which warmed the Earth, has decreased to the present levels as the luminosity of the Sun has increased. The decreases in the greenhouse gases can be controlled by a negative feedback mechanism associated with carbonate-silicate geochemical cycle (so-called the "Walker feedback") (Walker et al., 1981).

In the carbonate-silicate geochemical cycle, carbon is degassed to the atmosphere and ocean as CO_2 through volcanic activity. The CO_2 reacts with silicate minerals, that is, chemical weathering of silicate minerals (or silicate weathering), which can be written as follows:

$$CaSiO_3 + 2\,CO_2 + H_2O \longrightarrow Ca^{2+} + 2\,HCO_3^- + SiO_2. \tag{1.1}$$

The silicate weathering occurs usually on land surface, and ions are carried into the oceans through. In the oceans, these ions react with each other to precipitate as carbonate minerals as follows:

$$Ca^{2+} + 2\,HCO_3^- \longrightarrow CaCO_3\downarrow + CO_2 + H_2O. \tag{1.2}$$

Hence, the whole reaction is

$$CaSiO_3 + CO_2 \longrightarrow CaCO_3 + SiO_2. \tag{1.3}$$

The carbonate minerals precipitated onto the seafloor moves with an oceanic plate, and a part of them may accrete to the continents, but the rest should subduct into the mantle or degas to the atmosphere again as CO_2 via subduction zone volcanism.

The rate of silicate weathering depends on the surface temperature while the degassing of CO_2 via volcanic activity would be independent from the surface temperature, resulting in the Walker feedback. For example, if the surface temperature increases above the one in a steady state, the reaction rate of silicate weathering increases. The increase in the silicate weathering rate decreases the amount of the atmospheric CO_2, and as a result, the surface temperature decreases to the steady state. An increase (decrease) in other greenhouse gases, such as methane and/or ammonia, decreases (increases) the amount of CO_2 through the same mechanism. In this way, the surface temperature of the Earth is maintained at a steady state. This mechanism is called the "Walker feedback"

The degassing of CO_2 via volcanic activity also plays an important role in recovering the Earth from a snowball state. CO_2 uptake via silicate weathering needs liquid water (Equation 1.1). Thus, if the Earth is globally ice-covered, the silicate weathering does not occur, resulting in an accumulation of CO_2 in the atmosphere, which results in melting of global covered ice (e.g., Hoffman et al.,

1998).

1.2 Toward a comprehensive view of a climate evolution of Earth-like planets: the role of the CO_2 degassing and internal evolution

The carbonate-silicate geochemical cycle and the Walker feedback have been a basis for the concept that the climate of Earth-like planets orbiting within the habitable zone (HZ) around stars may also be warm like the climate of the Earth (e.g., Kasting et al., 1993; Kopparapu et al., 2013). Here, the HZ is the concentric region around main-sequence stars where Earth-like planets can have liquid water on their surface (e.g., Kasting et al., 1993; Kopparapu et al., 2013). It is supposed that the Walker feedback may control the amount of CO_2 in the atmosphere and maintain the greenhouse effect sufficient for maintaining warm climate (e.g., Kasting et al., 1993; Kopparapu et al., 2013).

However, Tajika (2003, 2007) revealed that, even if the carbonate-silicate geochemical cycle and the Walker feedback mechanism work, the Earth may be in a snowball state if the CO_2 degassing rate becomes smaller (or the efficiency of the CO_2 uptake rate via silicate weathering becomes higher) than a critical value. The critical values have been examined for the cases the insolation corresponding to the values of the present Earth and of the Paleo- and Neo-proterozoic snowball Earth events (Tajika, 2003, 2007). However, the critical values for other conditions have not been examined. Thus, a comprehensive view of a climate of the Earth and Earth-like planets is still unclear, especially in terms of the CO_2 degassing rate.

According to the results of Tajika (2003, 2007), the climate of the Earth depends on the CO_2 degassing rate (and/or the efficiency of the CO_2 uptake rate via silicate weathering) in addition to the insolation. The insolation has increases owing to the increase in the luminosity of the central star (Iben, 1967; Gough, 1981). On the other hands, after a catastrophic degassing event early in the Earth history (e.g., Zhang, 2014), the rate of CO_2 degassing has decreased with time owing to the cooling of the planetary interior (e.g., Tajika and Matsui, 1992). The rate of CO_2 degassing depends on the melt generation depth under the mid-ocean ridges

and the seafloor spreading rate, which, in turn, depends on the mantle temperature and heat flow. The degassing history is, therefore, determined by the thermal evolution of the planetary interior. According to the classical studies of thermal evolution of the Earth, both the melt generation rate and seafloor spreading rate decreases with time (e.g., Schubert et al., 1979, 1980; Richter and McKenzie, 1981; Schubert and Spohn, 1981; Stevenson et al., 1983; McGovern and Schubert, 1989), although it is also suggested that the seafloor spreading rate could be relatively constant during the Earth's history (e.g., Christensen, 1985; Tajika and Matsui, 1992, 1993a; Korenaga, 2008, 2011). Recent studies on the thermal evolution of the Earth, it is suggested that the high mantle temperature promotes the dehydration from the mantle, resulting in a stiffening of a lithosphere and a decreasing of the heat flow relative to the classical estimate (Korenaga, 2008, 2011). Considering these evolutions of the luminosity and CO_2 degassing rate, the evolution track of the climate of the Earth and Earth-like planets can be investigated. Tajika (1992) investigated the evolution of the Earth's climate, and showed that the warm climate can be maintained throughout the Earth's history owing to the Walker feedback mechanism. However, the evolutionary tracks of the climate for other cases, for example, the orbital semi-major axis is different from the one for the Earth, have not been investigated so far. Such a study will reveal the limit of application of the Walker feedback mechanism in a wide range of space and time regions, which may reveal the orbital region and age conditions where the Walker feedback is indeed able to maintain the Earth and Earth-like planets warm, i.e., the internal structure of the HZ. It will contribute to the understanding of the climate evolution of the Earth itself, and also the climate evolution of the Earth-like planet in the HZ of the planetary systems.

The Earth has, indeed, experienced the snowball Earth events, at least, three times in its history (e.g., Kirschvink, 1992; Hoffman et al., 1998). The termination of these events can be explained by a buildup of CO_2 in the atmosphere (e.g., Kirschvink, 1992). To the contrary, the initiations of these events have not been known well. The Paleoproterozoic (Makganyene) snowball Earth event (~ 2.34 Ga) might have been triggered by a collapse of methane greenhouse due to accumulation of molecular oxygen released by oxygen-producing photosynthetic bacteria (cyanobacteria), which might have emerged just before the glaciation (Kasting et al., 2001; Kopp et al., 2005). If it were the case, the Paleoproterozoic

snowball Earth event might have been caused by the evolution of life. In contrast to the Paleoproterozoic event, there are two discrete snowball Earth events occurred within a very short period of time (< 100 million years, or Myr) in the Neoproterozoic, i.e., the Sturtian (717–660 Ma) and Marinoan (639–635 Ma) snowball Earth events (Rooney et al., 2015; Prave et al., 2016). The causes of these two events are uncertain although several hypotheses have been proposed such as the CO_2 drawdown due to an increase in the productivity of phytoplankton in the oceans (Hoffman et al., 1998), due to a break-up of the supercontinent Rodinia (Donnadieu et al., 2004a), due to a reduction in the CO_2 degassing rate (Tajika, 2003, 2007, 2013), or the formation and collapse of methane greenhouse (Schrag et al., 2002; Pavlov et al., 2003). However, the problem is the reason why these two snowball events occurred repeatedly within a very short period of time during the Neoproterozoic, and why the snowball Earth event did not occur during the other geological ages (excepts for the Paleoproterozoic snowball Earth event, which might have been caused by the emergence of cyanobacteria) although the processes which may have caused the Neoproterozoic snowball Earth events could have also occurred during the other geological ages in the history of the Earth.

1.3 Scope and strategy of the present study

In order to reveal the application limit of the Walker feedback mechanism and to gain a comprehensive view of the diversity and evolution of the climate of the Earth and Earth-like planets (hereafter, collectively called as the "hypothetical Earths"), it is necessary to investigate the climate of the Earth in a steady state for a very wide range of parameter space of the orbital semi-major axis throughout the HZ and the time evolution of the planet and the central star. Here, assumed parameters and their ranges as follows: insolation (0.35 to 1.05 times the present solar constant, which corresponds to the insolation range of the HZ (Kasting et al., 1993; Kopparapu et al., 2013)), a CO_2 degassing rate (lower than 100 times the CO_2 degassing rate of the present Earth, which corresponds to the CO_2 degassing rate of the early Earth in Tajika and Matsui (1992)), partial pressure of atmospheric CO_2 (pCO_2) (lower than 10 bar, which roughly corresponds to the pCO_2 at the outer limit of the HZ (Kasting et al., 1993; Kopparapu et al., 2013)), and surface temperature (lower than 400 K, which roughly corresponds to the surface temperature at the inner

limit of the HZ (Kasting et al., 1993; Kopparapu et al., 2013)). For this purpose, a one-dimensional energy balance climate model (1D-EBM) is used in this study. Although the 1D-EBM can reproduce the climate condition of the present Earth, it may have uncertainty especially under very different conditions from that of the present Earth because the 1D-EBM does not consider atmospheric dynamics. It is however the only model which can apply to this purpose because more realistic models such as GCMs cannot be used for such a large number of parameter studies owing to heavy computational cost.

The climate of the Earth in a steady state can be obtained when the CO_2 degassing rate is given with a given insolation through calculating the CO_2 uptake via silicate weathering because the CO_2 degassing should balance with the CO_2 uptake. For calculating the climate in a steady state, factors other than the kinetic limitation of the silicate weathering, which is responsible for the Walker feedback mechanism, are not considered in this study because other factors, such as a soil biological efficiency (e.g., Berner, 1991, 1994) and/or transport limitation (e.g., Kump et al., 2000), decreases the efficiency of CO_2 uptake rate, resulting in the warming of the hypothetical Earth. A difference in the efficiency of the CO_2 uptake rate is equivalent to a difference in the CO_2 degassing rate: for example, an increase in the efficiency of the CO_2 uptake rate by a factor of 2 corresponds to a decrease in the CO_2 degassing rate by a factor of 2. Therefore, the application limit of the Walker feedback mechanism is estimated here in terms of the CO_2 degassing rate and insolation assuming that the efficiency of the CO_2 uptake rate is equal to that of the present Earth.

The climate of the hypothetical Earth evolves owing to a luminosity increase, a decrease in the CO_2 degassing rate, and an increase of the efficiency of the CO_2 uptake rate. The CO_2 degassing rate tends to decreases with time owing the thermal evolution of the planetary interior on a timescale of 10^9 years although it may fluctuate owing to changes in the seafloor spreading rate due to the Wilson cycle on a shorter timescale of 10^8–10^7 years (Wilson, 1966). In this study, the long-term trend of the decrease in the CO_2 degassing rate is focused on, and the effect of the shorter-term fluctuations of the CO_2 degassing rate will be discussed in the Section 4.

The timescale of the long-term trend of the decrease in the CO_2 degassing rate (10^9 years) is long enough to compare with the residence time of CO_2 in the

atmosphere-ocean system (10^6 years). Therefore, the climate is estimated from the luminosity and CO_2 degassing rate, assuming that the climate is always in a steady state. The efficiency of the CO_2 uptake rate could have increased owing to the continental growth, evolution of life on land and so on, which results in the cooling of the climate of the hypothetical Earth (e.g., Schwartzman and Volk, 1989; Tajika and Matsui, 1992, 1993b; Berner, 1991, 1994; Berner and Kothavala, 2001). In this study, the efficiency of the CO_2 uptake rate is assumed to be constant at that of the present Earth (i.e., the relatively high efficiency of the CO_2 uptake rate during the Earth's history) as a standard case in order to estimate the lower limit of the conditions for the warm climate of the hypothetical Earth. The effect of the continental growth on the climate evolution will be discussed later. The different timescale of the luminosity evolution (i.e., the different stellar type of the central star) is supposed to affect the evolution of the climate of the hypothetical Earth (Kasting et al., 1993). The effect of the timescale of the luminosity evolution is also revisited with considering the evolution of the CO_2 degassing rate.

1.4 Purposes and structure of this thesis

To summarize, the main purposes of this study are to reveal the application limit of the Walker feedback mechanism and also to reveal the evolutionary tracks of the climate of the hypothetical Earth throughout the HZ in the solar systems. The reason why the Earth has been globally ice-covered repeatedly in the Neoproterozoic is also discussed.

This paper is organized as follows. In Section 2, models used in this study are introduced. In Section 3, the results of the standard case are explained: the climate modes of the hypothetical Earth in the HZ are described and the application limits of the Walker feedback are shown, and the evolutions of the CO_2 degassing rate and luminosity and the evolutionary tracks of the climate of the hypothetical Earth are described. In Section 4, structures of the climate modes in the HZ, parameter studies for the evolutionary track of the Earth's climate, and the effect of the timescale of the luminosity evolution are discussed. Conclusions are summarized in Section 5. 5

Section 2

Model

2.1 Climate Model

2.1.1 One-dimensional energy balance climate model

We assume the planetary atmosphere composed of CO_2, water vapor (H_2O), and 1 bar background gas which is non-condensable and transparent to infrared radiation, such as N_2 and O_2. The climate model used in this study is a meridionally one-dimensional energy balance climate model (1D-EBM). The basic equation of 1D-EBM is described as follows:

$$(1 - A(T, p\mathrm{CO_2}))Q(\varphi) - I(T, p\mathrm{CO_2}) + F(T, p\mathrm{CO_2}) = 0 \tag{2.1}$$

where T is surface temperature, $p\mathrm{CO_2}$ is partial pressure of atmospheric CO_2, φ is latitude, A is planetary albedo, Q is insolation, I is infrared radiation, and $F$is meridional heat transport.

The numerical data of infrared radiation and planetary albedo estimated by Kopparapu et al. (2013, 2014) are used in this study. The original data are obtained from a one-dimensional radiative-convective model with cloud-free atmosphere, which uses new H_2O and CO_2 absorption coefficients derived from the HITRAN 2008 and HITEMP 2010 line-by-line database. The model atmosphere contains 1 bar of N_2 and CO_2, and is saturated with H_2O. The infrared radiation depends on $p\mathrm{CO_2}$ and T, and the planetary albedo depends on $p\mathrm{CO_2}$, T, surface albedo (A_s), and solar zenith angle (Z). The original data of the infrared radiation are

calculated over a parameter space spanning 1×10^{-5} bar $< p\mathrm{CO}_2 <$ 35 bar and 150 K $< T <$ 350 K. The parameter spaces of $p\mathrm{CO}_2$ and T of the planetary albedo are as same as those of the infrared radiation, and those of A_s and $0.2 < A_\mathrm{s} < 1$ and $0° < Z < 90°$, respectively.

The model infrared radiation is fitted by a polynomial function of T and $p\mathrm{CO}_2$ expressed as follows;

$$I(T, p\mathrm{CO}_2) = I_0 \begin{pmatrix} 1 & \tau & \tau^2 & \tau^3 & \tau^4 & \tau^5 & \tau^6 \end{pmatrix} \mathrm{B} \begin{pmatrix} 1 & p & p^2 & p^3 & p^4 \end{pmatrix}^t \tag{2.2}$$

where $\tau = 0.01 \times (T - 250)$. When $p\mathrm{CO}_2 < 1$ bar, p and A are represented as follows;

$$p = 0.2 \times \log_{10} p\mathrm{CO}_2 \tag{2.3}$$

$$\mathrm{B} = \begin{pmatrix} 87.8373 & -311.289 & -504.408 & -422.929 & -134.611 \\ 54.9102 & -677.741 & -1440.63 & -1467.04 & -543.371 \\ 24.7875 & 31.3614 & -364.617 & -747.352 & -395.401 \\ 75.8917 & 816.426 & 1565.03 & 1453.73 & 476.475 \\ 43.0076 & 339.957 & 996.723 & 1361.41 & 612.967 \\ -31.4994 & -261.362 & -395.106 & -261.600 & -36.6589 \\ -28.8846 & -174.942 & -378.436 & -445.878 & -178.948 \end{pmatrix}. \tag{2.4}$$

When $p\mathrm{CO}_2 > 1$ bar, p and A are represented as follows;

$$p = \log_{10} p\mathrm{CO}_2 \tag{2.5}$$

$$\mathrm{B} = \begin{pmatrix} 87.8373 & -52.1056 & 35.2800 & -1.64935 & -3.42858 \\ 54.9102 & -49.6404 & -93.8576 & 130.671 & -41.1725 \\ 24.7875 & 94.7348 & -252.996 & 171.685 & -34.7665 \\ 75.8917 & -180.679 & 385.989 & -344.020 & 101.455 \\ 43.0076 & -327.589 & 523.212 & -351.086 & 81.0478 \\ -31.4994 & 235.321 & -462.453 & 346.483 & -90.0657 \\ -28.8846 & 284.233 & -469.600 & 311.854 & -72.4874 \end{pmatrix}. \tag{2.6}$$

The average and maximum of absolute errors between the original data and the fitted values is 0.6 W/m^2 and 3.3 W/m^2, respectively. Figure 2.1 shows the model infrared radiation and original data of Kopparapu et al. (2013, 2014). As shown

in Figure 2.1, an increase in the surface temperature results in an increase in the infrared radiation while an increase in $p\mathrm{CO}_2$ results in a decrease in the infrared radiation. I_0 is adjusted so as to reproduce the present Earth's surface distribution.

For the planetary albedo, the original data (Kopparapu et al., 2013, 2014) is fitted by a cubic spline interpolation. Figure 2.2 shows the relation between the planetary albedo and surface temperature when Z is assumed to be the average zenith angle at the equator (i.e., 50°). The planetary albedo changes around $T = 273.15\,\mathrm{K}$ owing to the melting/forming of $\mathrm{H_2O}$ ice. In addition, an increase in T results in a decrease in the planetary albedo owing to an increase in absorption of infrared radiation from the Sun due to an increase in $p\mathrm{H_2O}$. On the other hand, when T is below the freezing point of $\mathrm{CO_2}$ which is explained below, the planetary albedo changes stepwise owing to the condensation of $\mathrm{CO_2}$.

The surface albedo is expressed as follows (Williams and Kasting, 1997):

$$A_\mathrm{s} = (1 - f_\mathrm{c}) \left[f_\mathrm{o} A_\mathrm{o} + (1 - f_\mathrm{o})\, A_\mathrm{l} \right] + f_\mathrm{c} A_\mathrm{c}. \tag{2.7}$$

where f_c is a fraction of area covered by cloud which is assumed to be 0.5 in this study, f_o is a fraction of ocean area (ocean fraction), A_o is ocean albedo, A_l is land albedo, and A_c is cloud albedo. As a standard case, f_o is constant at 0.7 for any latitude. The ocean albedo is expressed as follows:

$$A_\mathrm{o} = \begin{cases} A_\mathrm{ice} & T < 264.8\,\mathrm{K} \\ f_\mathrm{ice} A_\mathrm{ice} + (1 - f_\mathrm{ice}) A'_\mathrm{o} & 264.8\,\mathrm{K} < T < 273.15\,\mathrm{K} \\ A'_\mathrm{o} & T > 273.15\,\mathrm{K} \end{cases} \tag{2.8}$$

where f_ice is fraction of area covered by ocean ice, A_ice is ice albedo, and A'_o is unfrozen ocean albedo. The unfrozen albedo is assumed to be the fraction of insolation reflected by a smooth oceanic surface ($n = 1.33$) through the Fresnel reflectance formulae (Williams and Kasting, 1997). The fraction of area covered by sea ice is modeled here based on the Hadley Centre sea ice and sea surface temperature data set as follows (Rayner et al., 2003):

$$t_\mathrm{ice} = \frac{273.15 - T}{8.35}, \tag{2.9}$$

$$f_\mathrm{ice} = -0.004 t_\mathrm{ice}^3 + 3.556 t_\mathrm{ice}^4 - 2.552 t_\mathrm{ice}^5. \tag{2.10}$$

The land albedo is expressed as (Kondrat'ev, 1969; Williams and Kasting, 1997):

$$A_{\rm l} = \begin{cases} A_{\rm ice} & T < 273.15\,{\rm K} \\ 0.2 & T > 273.15\,{\rm K} \end{cases} \tag{2.11}$$

The ice albedo is modeled by a band-dependent ice albedo as follows (Haqq-Misra et al., 2016; Warren et al., 1990):

$$A_{\rm ice} = \begin{cases} 0.35 & T < T_{\rm ice,co2} \\ F_{\rm vis}A_{\rm ice} + (1 - F_{\rm vis})A_{\rm nir} & T > T_{\rm ice,co2} \end{cases} . \tag{2.12}$$

The ice albedo for visible light, $A_{\rm ice}$, is 0.8, and the ice albedo for near-infrared radiation, $A_{\rm ice}$, is 0.5 (Pollard and Kasting, 2005). The contribution of visible light, $F_{\rm vis}$, is 52 % for the energy flux emitted from the Sun (Allard et al., 2007). When surface temperature is below the freezing temperature of CO_2 ($T_{\rm ice,co2}$), the H_2O ice is assumed to be covered by the CO_2 ice. So, $A_{\rm ice}$ is set to be the albedo of CO_2 ice (0.35; Warren et al., 1990). The cloud albedo is expressed as a function of Z as follows (Jacobowitz et al., 1979):

$$A_{\rm c} = -0.078 + 0.65Z. \tag{2.13}$$

Heat is assumed to be transported meridionally by diffusion:

$$F = \frac{1}{\cos\varphi}\frac{\partial}{\partial\varphi}\left[D\left(p{\rm CO_2}, p{\rm H_2O}\right)\cos\varphi\frac{\partial T}{\partial\varphi}\right] \tag{2.14}$$

Assuming that the heat is transported by the baroclinic instability (Gierasch and Toon, 1973), thermal diffusion coefficient, D, is assumed to be proportional to the total pressure of the atmosphere:

$$D(p{\rm H_2O}, p{\rm CO_2}) = (P_{\rm air} + p{\rm H_2O} + p{\rm CO_2})D_0 \tag{2.15}$$

where $P_{\rm air}$ is the partial pressure of the background atmospheric gases, which is assumed to be 1 bar and has no greenhouse effect in this model, and $p{\rm H_2O}$ is assumed to be saturated water vapor pressure. The constant, D_0 is adjusted so as to reproduce the distribution of the surface temperature of the present Earth.

Insolation, Q, depends on orbital elements and latitude, in addition to the

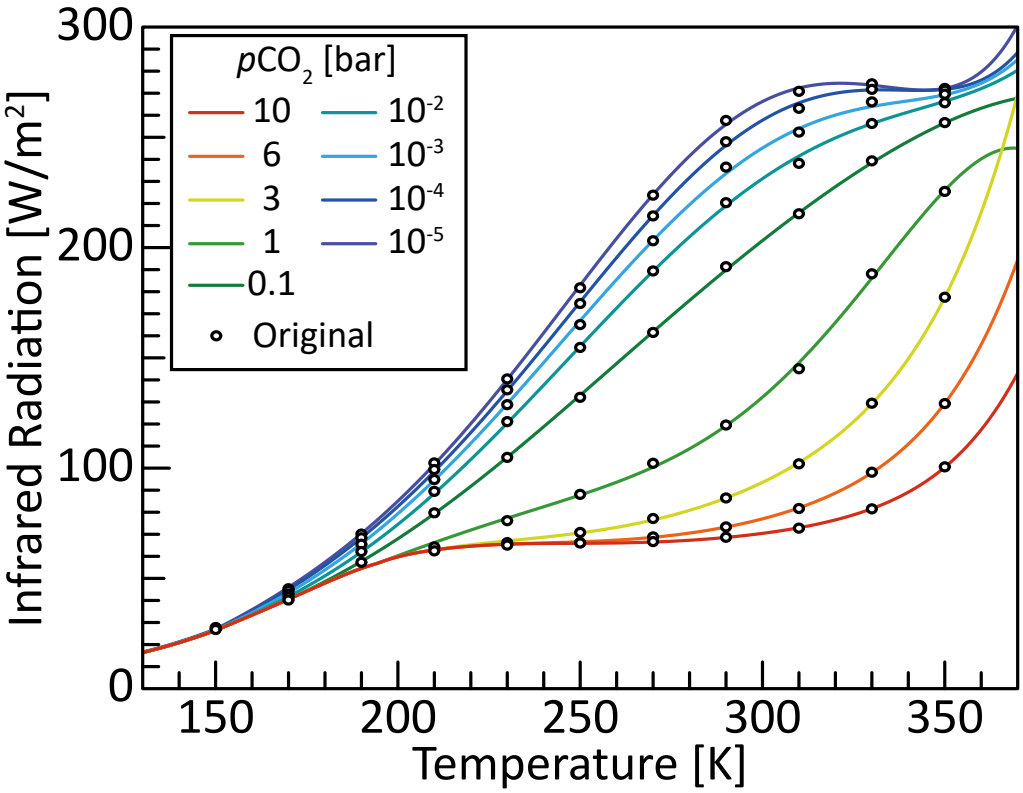

Figure 2.1: The relation between the temperature and the infrared radiation. The black circles are the original data calculated by (Kopparapu et al., 2013, 2014)

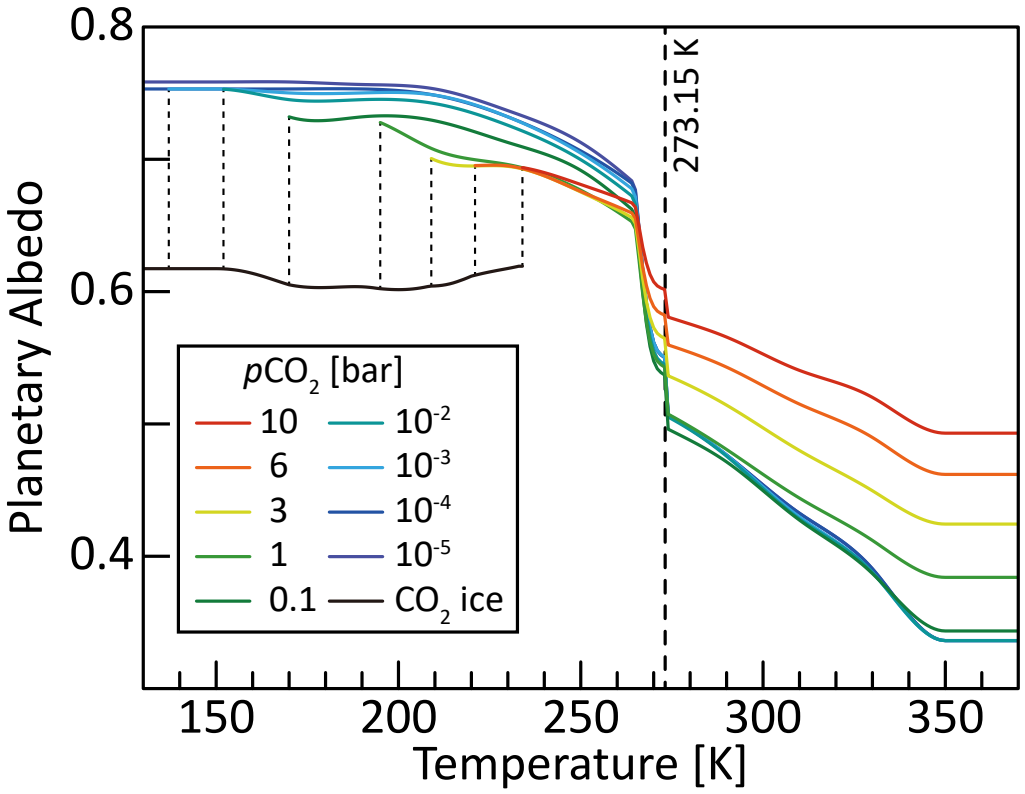

Figure 2.2: The relation between the temperature and the planetary albedo. The planetary albedo changes around $T = 273.15\,\mathrm{K}$ owing to the melting/forming of H_2O ice. In addition, an increase in T results in a decrease in the planetary albedo owing to the increase in pH_2O. On the other hand, when T is below the freezing point of CO_2, the planetary albedo changes stepwise owing to the condensation of CO_2. Note that the freezing point of CO_2 depends on pCO_2.

luminosity of the central stars, L. These effects are summarized as follows:

$$Q(\phi, t) = \frac{F_{\mathrm{ZA}}(\varphi, t)}{r(t)^2} S \tag{2.16}$$

where F_{ZA} is the factor related to a zenith angle, r is the distance between the central star and the planet, and S is insolation. The expression of F_{ZA} is based on the previous works (e.g., Williams and Kasting, 1997) as follows:

$$F_{\mathrm{ZA}}(\varphi, t) = \sin\varphi \sin\delta(t) + \cos\varphi \cos\delta(t) \cos h(t), \tag{2.17}$$

where δ is the solar declination, and h is the solar hour angle. The solar declination, δ, depends on the obliquity, δ_0, orbital longitude, L_{s}, and the time of perihelion passage, L_{s}^*:

$$\sin\delta(t) = \sin\delta_0 \sin\left(L_{\mathrm{s}}(t) + L_{\mathrm{s}}*\right) \tag{2.18}$$

The longitudinal distribution of insolation is assumed to be diurnally averaged in this study. This is modeled as follows:

$$\overline{F_{\mathrm{ZA}}} = \frac{1}{\pi} \int_{-H(t)}^{H(t)} F_{\mathrm{ZA}}(\varphi, t) dh \tag{2.19}$$

where H is the radian half-day length given by

$$\cos H(t) = -\tan\varphi \tan\delta(t), \quad \text{for } 0 < H < \pi. \tag{2.20}$$

The orbital longitude, L_{s}, is expressed with eccentric anomaly, u, as follows:

$$\tan\frac{L_{\mathrm{s}}}{2} = \sqrt{\frac{1+e}{1-e}} \tan\frac{u(t)}{2}. \tag{2.21}$$

The eccentric anomaly, u, depends on time, t, as follows:

$$u(t) - e\sin u(t) = \frac{2\pi t}{T_{\mathrm{p}}} \tag{2.22}$$

where e is the orbital eccentricity, and T_{p} is the revolution period. When $t = 0$, the planet is at perihelion. The distance between the central star and the planet, r, is

expressed with the eccentric anomaly as follows:

$$r(t) = 1 - e\cos u(t) \tag{2.23}$$

In the 1D-EBM, the obliquity and eccentricity are set to be 23.4° and 0, respectively, supposing the present Earth, and the annual mean insolation which is calculated with Equation 2.16 is used for simplicity.

The relation between the freezing point of CO_2 ($T_{\mathrm{ice,co2}}$ in K) and pressure ($P_{\mathrm{ice,co2}}$ in bar) is calculated with the following formulae (Ambrose, 1956; Vukalovich and Altunin, 1968): when $T < 216.56\,\mathrm{K}$,

$$\log_{10} P_{\mathrm{ice,co2}} = 6.760956 - \frac{1.284\,07 \times 10^3}{T_{\mathrm{ice,co2}} - 4.718} + 1.256 \times 10^{-4}\left(T_{\mathrm{ice,co2}} - 143.15\right), \tag{2.24}$$

and when $T > 216.56\,\mathrm{K}$,

$$\log_{10} P_{\mathrm{ice,co2}} = 3.128082 - \frac{867.2124}{T_{\mathrm{ice,co2}}} + 1.865\,612 \times 10^{-2} T_{\mathrm{ice,co2}} - 7.248\,820 \times 10^{-5} T_{\mathrm{ice,co2}}^2 + 9.3 \times 10^{-8} T_{\mathrm{ice,co2}}^3. \tag{2.25}$$

The amount of the atmospheric CO_2 should decrease owing to condensation of CO_2 (e.g., Haberle et al., 1994; Nakamura and Tajika, 2001). In this study, when the minimum surface temperature is below the saturation temperature, pCO_2 is assumed to equal to the saturation pressure, and the excess CO_2 accumulates as CO_2 ice.

CO_2 clouds may form under a certain condition. However, because radiative property of CO_2 clouds depends on a size distribution of the cloud particle and also because there are large ambiguities of the cloud cover, location, height, and optical depth (e.g., Forget and Pierrehumbert, 1997; Mischna et al., 2000), we do not consider the effect of CO_2 clouds in this study. Instead, the conditions for the formation of CO_2 clouds will be shown for reference in the results. The surface temperature under which CO_2 clouds can be formed at a latitude is formulated by

Caldeira and Kasting (1992) as follows;

$$\psi = \log_{10}\left\{\frac{p\mathrm{CO_2}}{3\times10^{-4}}\right\} \tag{2.26}$$

$$T_{\mathrm{cloud}} = 281 + 68.2\psi + 15.4\psi^2 + 1.34\psi^3. \tag{2.27}$$

2.1.2 Carbon cycle and CO_2 mass balance model

The supply of CO_2 via volcanic degassing, F_{D}, is assumed to be equal to the uptake of CO_2 via silicate weathering, W, which is followed by precipitation of carbonate minerals in the ocean:

$$F_{\mathrm{D}} - W = 0 \tag{2.28}$$

The CO_2 Uptake rate via silicate weathering is expressed as follows (Walker et al., 1981; Schwartzman and Volk, 1989, 1991; Berner, 1991, 1994; Berner and Kothavala, 2001; Tajika, 2003, 2007; Menou, 2015):

$$W(p\mathrm{CO_2}, T) = \int W_0\left(\frac{p\mathrm{CO_2}}{p\mathrm{CO_2^{ref}}}\right)^n \exp\left\{\frac{-\Delta E}{RT(\varphi)}\right\} Area(\varphi)d\varphi. \tag{2.29}$$

In the formulation, ΔE is activation energy (= 63 kJ) (Berner, 1994), $p\mathrm{CO_2^{ref}}$ is the reference $p\mathrm{CO_2}$ (= 3×10^{-4} bar). R is gas constant, n is the dependence on $p\mathrm{CO_2}$. We adopt $n = 0.3$ for the exponent of $p\mathrm{CO_2}$ as a standard value (e.g., Walker et al., 1981; Volk, 1987; Tajika, 2003, 2007; Menou, 2015). $Area$ is the areal ratio of land without ice cover to the surface of each latitude, where the silicate weathering occurs (Kirschvink, 1992):

$$Area = \begin{cases} 0 & T < 273.15\,\mathrm{K} \\ 1 - f_{\mathrm{o}} & T > 273.15\,\mathrm{K} \end{cases} \tag{2.30}$$

For the rate of CO_2 degassing via volcanism, the value of the present Earth, F_{D0}, is adopted as a standard, and equates with the rate of CO_2 uptake by chemical weathering.

2.2 Climate evolution model

The long-term evolution of surface environment of the Earth or an Earth-like planet was calculated from the climate model coupled with the simplified carbon cycle model which estimates a decrease of $p\mathrm{CO}_2$ in the atmosphere with time, as a result of a decrease of the CO_2 degassing rate from the mantle owing to the thermal evolution of the planetary interior, and also, coupled with the results from a stellar evolution model which estimates an increase of the luminosity of the Sun with time. In this section, the models for the thermal evolution of the Earth and for the luminosity evolution of the Sun are introduced.

2.2.1 Thermal evolution model

The CO_2 degassing from the interior of the Earth depends on the activity of plate tectonics through the igneous processes at mid-ocean ridges and at subduction zones. In other words, the CO_2 degassing rate can be approximated to depend on the seafloor spreading rate (e.g., Berner et al., 1983; McGovern and Schubert, 1989; Tajika and Matsui, 1992; Berner, 1991, 1994). Evolution of the seafloor spreading rate may be estimated from the thermal evolution of the planet (e.g., Tajika and Matsui, 1992). In this study, the models of Tajika and Matsui (1992) are adopted to estimate the evolution of the seafloor spreading rate, and then, that of the CO_2 degassing rate.

The evolution of an average mantle temperature is calculated with a parameterized convection model (e.g., Sleep, 1979; Schubert et al., 1980; Stevenson et al., 1983; Christensen, 1985; McGovern and Schubert, 1989; Tajika and Matsui, 1992; Sandu et al., 2011; Korenaga, 2006, 2011; Schaefer and Sasselov, 2015). The equation of conservation of energy is expressed as follows:

$$\rho C_\mathrm{m} \frac{dT_\mathrm{m}(t)}{dt} = -\frac{3R_\mathrm{m}^2}{R_\mathrm{m}^3 - R_\mathrm{c}^3} q(t) + Q(t), \tag{2.31}$$

where T_m is the average mantle temperature, ρC_m is the heat capacity, R_m and R_c are the radii of the mantle and the core, respectively, and q is the heat flow from the mantle. Q_m is the energy production by decay of radiogenic heat sources in

the mantle which is expressed as follows:

$$Q_{\rm m}(t) = Q_0 \exp\{-\lambda t\} \tag{2.32}$$

where λ is the average decay constant. The constant, Q_0, is set to be 2.276×10^{-7} W/m^3 so as to reproduce the heat flow from the mantle of the Earth today, 101 mW/m^2 (Turcotte and Schubert, 2002) at $t = 4.6 \times 10^9$ year. The heat flow from the mantle, q, is parameterized in terms of the Rayleigh number, Ra, as follows:

$$q(t) = \frac{k(T_{\rm m} - T_{\rm s})}{R_{\rm m} - R_{\rm c}} \left(\frac{Ra(t)}{Ra_{\rm cr}} \right)^{\beta} \tag{2.33}$$

$$Ra = \frac{g\alpha(T_{\rm m} - T_{\rm s})(R_{\rm m} - R_{\rm c})^3}{\kappa\nu} \tag{2.34}$$

where k is the thermal conductivity, g is the gravitational acceleration, α is the coefficient of thermal expansion rate, κ is the thermal diffusivity. The exponent of the Rayleigh number, β, is one third as a standard case. The viscosity, ν, is assumed to depend on the average mantle temperature, and it is expressed as follows:

$$\nu(T) = \nu_0 \exp \frac{A_{\rm m}}{T_{\rm m}} \tag{2.35}$$

where ν_0 is 5.7876×10^6 m^2/s based on McGovern and Schubert (1989), and $A_{\rm m}$ is set to be 5.79×10^4 K in the same way as Q_0.

The seafloor spreading rate, SR, is modeled as a function of the heat flow from the mantle when a cooling of the oceanic plate is modeled as a cooling of a semi-infinite half space (e.g., McGovern and Schubert, 1989; Tajika and Matsui, 1992). Assuming the cooling of the semi-infinite half space, the heat flow from the mantle is expressed as (Turcotte and Schubert, 2002):

$$q = \frac{2k\Delta T}{\sqrt{\pi\kappa\tau_{\rm o}}}, \tag{2.36}$$

where ΔT is the difference in the temperature across the upper boundary layer and modeled as the difference between the surface temperature and the potential temperature of the mantle (i.e., $\Delta T \sim T_{\rm p} - T_{\rm s}$) (Tajika and Matsui, 1992). The

average residence time of the oceanic plate, τ_o, is expressed as:

$$\tau_o = \frac{S_o}{SR(t)} \tag{2.37}$$

where S_o is the area of the ocean floor, which is assumed to be 0.7 times of the surface area of the Earth. Therefore, the seafloor spreading rate is expressed as follows:

$$SR(t) = \frac{\pi \kappa S_o}{[2kT_p - T_s]^2} q(t)^2. \tag{2.38}$$

The potential temperature of the mantle, T_p, can be scaled by the average mantle temperature, T_m, assuming an adiabatic temperature gradient in the convective mantel as follows:

$$T_p = \frac{\int \rho C_p r'^2 dr'}{\int \rho C_p \exp\left(\int \frac{g\alpha}{C_p} dr'\right) r'^2 dr'} T_m = \gamma_p T_m \tag{2.39}$$

where γ_p is estimated to be 0.7 (Tajika and Matsui, 1992). The melt generation depth, d_m, is estimated from the potential temperature of the mantle, and the solidus temperature of mantle materials as follows:

$$T_{sol} = -5.104 P_{sol}^2 + 132.899 P_{sol} + 1120.661 \tag{2.40}$$

where T_{sol} is in °C, and P_{sol} is in GPa (Hirschmann, 2000).

The melt generation rate, V_m, is estimated from SR multiplied by d_m (i.e., $V_m(t) = SR(t) d_m(t)$). The CO_2 degassing rate depends on the melt generation rate and the mantle content of carbon. In this study, however, the mantle content of carbon is assumed to be constant for simplicity. The CO_2 degassing rate, F_D, is, therefore, expressed as follows:

$$F_D(t) = f_{CO2} V_m, \tag{2.41}$$

where f_{CO2} is the degassing fraction of CO_2 which is defined as the fraction of CO_2 that degases to the surface compared to the total amount of CO_2 that is originally included in the mantle degassing volume. It is estimated to be 0.32 (Tajika and

Matsui, 1992).

The parameters for the thermal evolution model are summarized in Table 2.1.

2.2.2 Luminosity evolution model

The luminosity of the main sequence star increases with time. In this study, the results of the luminosity evolution of the main sequence stars obtained from the theoretical study by Pols et al. (1998), which is fitted and formulated by Tout et al. (1996) and Hurley et al. (2000), are used. The luminosity evolution of the main sequence star is expressed as follows:

$$\log \frac{L(t)}{L_{\rm ZAMS}} = \alpha_{\rm L}\tau + \beta_{\rm L}\tau^{\eta} + \left(\frac{L_{\rm TMS}}{L_{\rm ZAMS}} - \alpha_{\rm L} - \beta_{\rm L}\right)\tau^2 - \Delta L(\tau_1^2 - \tau_2^2) \tag{2.42}$$

where τ is a time divided by a main sequence time, $\tau_{\rm MS}$, $L_{\rm ZAMS}$ and $L_{\rm TMS}$ are luminosity at zero-age main-sequence and at the end of main-sequence, respectively. The parameters, such as $\tau_{\rm MS}$, $L_{\rm ZAMS}$, $L_{\rm TMS}$, and others, are the functions of the stellar mass and the metallicity though only the effect of the stellar mass is focused on in this study. Hereafter, M is represented in the unit of $M_{\rm sun}$.

$L_{\rm ZAMS}$ and $L_{\rm TMS}$ are represented as follows:

$$L_{\rm ZAMS} = \frac{a_1 M^{5.5} + a_2 M^{11}}{a_3 + M^3 + a_4 M^5 + a_5 M^7 + a_6 M^8 + a_7 M^{9.5}} \tag{2.43}$$

$$L_{\rm TMS} = \frac{a_8 M^3 + a_9 M^4 + a_{10} M^{a_{13}+1.8}}{a_{11} + a_{12} M^5 + M^{a_{13}}}, \tag{2.44}$$

and $t_{\rm MS}$ is a function of a time taken to reach a base of the giant branch, $t_{\rm BGB}$, and a time taken to reach a hydrogen-exhausted phase gap, $t_{\rm hook}$. $t_{\rm hook}$ itself is also a function of $t_{\rm BGB}$. These timescales are expressed as follows:

$$t_{\rm MS} = \max\left(t_{\rm hook}, 0.95 t_{\rm BGB}\right) \tag{2.45}$$

$$t_{\rm BGB} = \frac{a_{14} + a_{15} M^4 + a_{16} M^{5.5} + M^7}{a_{17} M^2 + a_{18} M^7} \tag{2.46}$$

$$t_{\rm hook} = \mu t_{\rm BGB} \tag{2.47}$$

$$\mu = \max\left[0.5, 1 - 0.01 \max\left(\frac{a_{19}}{M^{a_{20}}}, a_{21} + \frac{a_{22}}{M^{a_{23}}}\right)\right]. \tag{2.48}$$

The hydrogen-exhausted phase gap appears if the stellar mass is larger than 1.0185 ($\equiv M_{\rm hook}$), and an increase in the luminosity at the hydrogen-exhausted phase gap is represented by ΔL, τ_1, and τ_2; these parameters are expressed as follows:

$$\Delta L = \begin{cases} 0 & M \leq M_{\rm hook} \\ a_{24} \times \left(\frac{M - M_{\rm hook}}{1.4 - M_{\rm hook}}\right)^{0.4} & M_{\rm hook} < M < 1.4 \end{cases} \tag{2.49}$$

$$\tau_1 = \min\left(1, \frac{t}{t_{\rm hook}}\right) \tag{2.50}$$

$$\tau_2 = \max\left\{0, \min\left[1, \frac{100t - 99t_{\rm hook}}{t_{\rm hook}}\right]\right\}. \tag{2.51}$$

The remaining factors, $\alpha_{\rm L}$ and $\beta_{\rm L}$, are expressed as follows:

$$\alpha_{\rm L} = \begin{cases} a_{25} & M < 0.5 \\ a_{25} + 5(0.3 - a_{25})(M - 0.5) & 0.5 \leq M \leq 0.7 \\ 0.3 + (a_{26} - 0.3)(M - 0.7)/(a_{29} - 0.7) & 0.7 \leq M \leq a_{29} \\ a_{26} + (a_{27} - a_{26})(M - a_{29})/(a_{30} - a_{29}) & a_{29} \leq M \leq a_{30} \\ a_{27} + (a_{28} - a_{27})(M - a_{30})/(2 - a_{30}) & a_{30} \leq M \leq 2 \end{cases} \tag{2.52}$$

$$\beta_{\rm L} = \max(0, a_{31} - a_{32} M^{a_{33}}) \tag{2.53}$$

Coefficients for the equations above are summarized in Table 2.2.

In this study, we assume the Sun: in other words, we assume the metallicity so that the luminosity of solar-mass ($M_{\rm sun}$) star may evolve to the solar luminosity at 4.6 Gyr.

2.3 Numerical procedures

The free parameters (I_0, D_0, and W_0) for the climate and carbon cycle models are adjusted so as to reproduce the present Earth's conditions (the globally averaged surface temperature is 288 K, $p{\rm CO_2}$ is 3.5×10^{-4} bar, and the globally averaged surface albedo is 0.31 under the condition that the insolation and CO_2 degassing rate are the present values of the present Earth, i.e., 1366 W/m^2 (e.g., Liou, 2002) and 6.65×10^{12} mol/yr (e.g., Berner, 1994), respectively). Figure 2.3 shows the

Table 2.1: Values of the constants for the thermal evolution model (Tajika and Matsui, 1992)

Constant	Value	Remarks
ρC_{m}	$4.2 \times 10^{6}\,\mathrm{J/m^3K}$	volumetric specific heat
R_{m}	$6.271 \times 10^{3}\,\mathrm{km}$	mantle radius
R_{c}	$3.471 \times 10^{3}\,\mathrm{km}$	core radius
λ	$3.4 \times 10^{-10}\,/\mathrm{yr}$	average decay constant
Ra_{cr}	1100	critical Rayleigh number
k	$4.2\,\mathrm{W/mK}$	thermal conductivity
κ	$10^{-6}\,\mathrm{m^2/s}$	thermal diffusivity
g	$9.8\,\mathrm{m/s^2}$	gravitational acceleration
α	$3 \times 10^{-5}\,/\mathrm{K}$	thermal expansivity
β	1/3	Nusselt-Rayleigh exponent
A_{m}	$5.79 \times 10^{4}\,\mathrm{K}$	activation temperature

Table 2.2: Coefficients for the luminosity evolution model (Tout et al., 1996; Hurley et al., 2000)

a_1	$3.970\,417 \times 10^{-1}$	a_{19}	$1.949\,814 \times 10^{1}$
a_2	$8.527\,626$	a_{20}	$4.903\,830$
a_3	$2.554\,600 \times 10^{-4}$	a_{21}	$5.212\,154 \times 10^{-2}$
a_4	$5.432\,889$	a_{22}	$1.312\,179$
a_5	$5.563\,579$	a_{23}	$8.073\,972 \times 10^{-1}$
a_6	$7.886\,606 \times 10^{-1}$	a_{24}	$1.673\,625 \times 10^{-1}$
a_7	$5.866\,85 \times 10^{-3}$	a_{25}	1.45×10^{-1}
a_8	$3.980\,613 \times 10^{3}$	a_{26}	2.4000×10^{-1}
a_9	$4.027\,603 \times 10^{3}$	a_{27}	3.3000×10^{-1}
a_{10}	$7.859\,573 \times 10^{2}$	a_{28}	$1.954\,969 \times 10^{-1}$
a_{11}	$3.858\,911 \times 10^{3}$	a_{29}	1
a_{12}	$2.888\,720 \times 10^{2}$	a_{30}	1.1
a_{13}	$7.196\,580$	a_{31}	$3.855\,707 \times 10^{-1}$
a_{14}	$1.593\,890 \times 10^{3}$	a_{32}	$3.579\,064 \times 10^{-1}$
a_{15}	$2.706\,708 \times 10^{3}$	a_{33}	$9.587\,587 \times 10^{-1}$
a_{16}	$1.466\,143 \times 10^{2}$		
a_{17}	$4.141\,960 \times 10^{-2}$		
a_{18}	$3.426\,349 \times 10^{-1}$		

surface temperature distribution calculated by the models of this study and that of the Earth from the database of the National Centers for Environmental Prediction (NCEP) and National Center for Atmospheric Research (NCAR) (Kalnay et al., 1996). The surface temperature in the south pole region is overestimated by the model of this study. In addition, the surface temperature is overestimated in the equatorial region, where the Hadley circulation transport heat well poleward. The effect of the atmospheric circulation is discussed in Section 4.

The free parameters (ν_0 and Q_0) for the thermal evolution are adjusted so as to reproduce the present Earth's condition (the average mantle potential temperature is 1350 °C (Herzberg et al., 2007) and the heat flow from the mantle is 100 $\mathrm{mW/m^2}$ (Turcotte and Schubert, 2002)) at 4.6 Gyr.

Surface temperature distribution and $p\mathrm{CO_2}$ in a steady state are obtained by solving Equation 2.1 and 2.29, given an insolation and $\mathrm{CO_2}$ degassing rate. However, it takes a long computational time to obtain the steady state. In order to shorten the computational time, the equations are solved as follows: (1) Separating latitudinally at every one degree (i.e., considering a system of equations which consists of 180 Equations 2.1), surface temperature distribution and insolation are obtained using an inverse matrix of Jacobian of the system of equations. The values of $p\mathrm{CO_2}$ and surface temperature at a latitude (typically, 273 K) are given as constraints. In addition, as boundary conditions, $\partial T/\partial\varphi = 0$ at $\varphi = -\pi/2$ and $\pi/2$ (i.e., Neumann boundary condition) are given. (2) The $\mathrm{CO_2}$ uptake rate is calculated with Equation 2.29 for a given $p\mathrm{CO_2}$ and calculated surface temperature distribution, and the $\mathrm{CO_2}$ degassing rate is equated with the $\mathrm{CO_2}$ uptake rate. Here, the use of this parameter set (insolation, $\mathrm{CO_2}$ degassing rate, $p\mathrm{CO_2}$, and surface temperature distribution) satisfy Equation 2.1 and 2.29. It is confirmed for several cases that the parameter sets obtained by this method and by the calculation of the time evolution are equal to each other.

The evolutionary track of climate is obtained as follow. (1) Time evolution of the mantle temperature and the $\mathrm{CO_2}$ degassing rate is calculated with Equations 2.31 and 2.41 with a time step of 10^6 years. (2) Given a semi-major axis, time evolution of insolation is obtained with Equation 2.42. (3) The climate is estimated every 10^8 year from the insolation and $\mathrm{CO_2}$ degassing rate at that time, in addition to the steady state solutions estimated from the climate models of Section 2.1. Here, the climate is assumed to be in a steady state at each time because

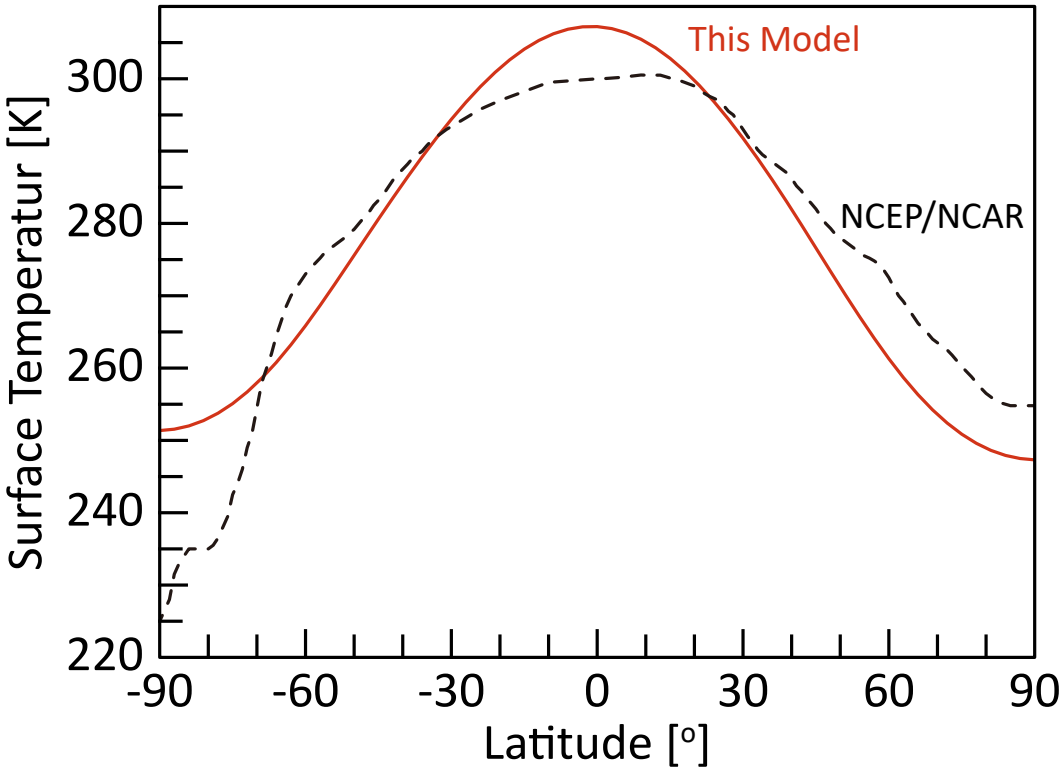

Figure 2.3: The zonally averaged surface temperatures. The red solid line represents the results from the climate models of this study, and the black dashed line represents the measurement from NCEP/NCAR temperature (Kalnay et al., 1996).

the timescale for which the residence time of CO_2 in the atmosphere-ocean system (10^6–10^7 years) is smaller than the characteristic timescale of the thermal evolution of the planetary interior and of the stellar evolution (10^8–10^9 years).

Section 3

Results

3.1 Definition of Climate Mode

3.1.1 Earth with various insolation

Figure 3.1 shows $p\mathrm{CO_2}$ and the globally-averaged surface temperature for different insolation under the condition of the present $\mathrm{CO_2}$ degassing rate of the Earth. The insolation, S, is expressed in the unit of the present solar flux for the Earth, S_0. In addition, Figure 3.1b also shows the globally-averaged surface temperature for the constant $p\mathrm{CO_2}$ (the gray line) for comparison. Here, we define two climate modes (the warm climate and the snowball cycle modes) for a hypothetical Earth in the habitable zone (HZ) according to the insolation, in addition to the two other climate modes for the planets outside of the HZ (the runaway greenhouse and snowball climate modes).

In the "warm" climate mode, the balances of both energy and atmospheric $\mathrm{CO_2}$ are achieved. Owing to the Walker feedback, i.e., the control mechanism of long-term $\mathrm{CO_2}$ levels through the chemical weathering of silicate minerals with a dependence on the surface temperature, an increase of the insolation results in a decrease of $p\mathrm{CO_2}$ (Figure 3.1a). Although the globally-averaged surface temperature increases with the insolation, the slope is gentler than that for the case of the constant $p\mathrm{CO_2}$ owing to the decrease in $p\mathrm{CO_2}$ (Figure 3.1b). In the warm climate mode, both $p\mathrm{CO_2}$ and the surface temperature are determined uniquely for each condition. This climate mode corresponds to the climate of the present Earth

(the blue diamond)

The hypothetical Earth can be globally ice-covered (a snowball state) even when the orbits are either outside the HZ or within the HZ. In the snowball state, the CO_2 uptake by chemical weathering and/or biological photosynthesis never work because all the liquid water on the planetary surface should freeze. However, the CO_2 supply due to volcanic degassing may occur on the snowball planets, and CO_2 should accumulate in the atmosphere with time. The snowball planets in the HZ may not remain globally ice-covered perpetually, and become the partially ice-covered or ice-free states (hereafter, these states are collectively referred to as a warm climate state) periodically in the evolution. Such a climate mode is classified as the "snowball cycle" mode. In Figure 3.1, the maximum and minimum values of $p\mathrm{CO}_2$ and the globally-averaged surface temperature are shown. The timescale for the variation depends both on the CO_2 degassing rate and the insolation for each planet. On the other hand, the "snowball" climate mode is defined here as the climate mode under which the hypothetical Earth is globally ice-covered perpetually and the ice-cover never melts. In other words, the snowball climate mode planet is unable to shift to the warm climate state. The boundary between the snowball cycle and snowball climate modes (i.e., the outer limit of the HZ) is at 0.44 S_0. This value is higher than the original results (0.34–0.36 S_0; Kasting et al., 1993; Kopparapu et al., 2013). The reason for the difference will be discussed later.

When $S > 1.048 S_0$, the surface temperature increases above the applicable range of the model (350 K), and $p\mathrm{CO}_2$ decreases below the applicable range of the model (1×10^{-5} bar). This implies the initiation of the runaway greenhouse, suggesting that the boundary between the warm and runaway greenhouse climate modes (i.e., the inner limit of the HZ) is 1.048 S_0. This value corresponds to the original result by Kopparapu et al. (2013) (1.0512 S_0) from which we adopted the numerical results of the planetary radiation and albedo models.

As a consequence, the HZ define in this study is between 0.44 and 1.06 S_0. It is, however, clearly shown that, even if the Earth is orbiting within the HZ and has the carbonate-silicate geochemical cycle which stabilizes $p\mathrm{CO}_2$, the Earth becomes the snowball cycle mode under the conditions of the present CO_2 degassing rate and $S < 0.8 S_0$.

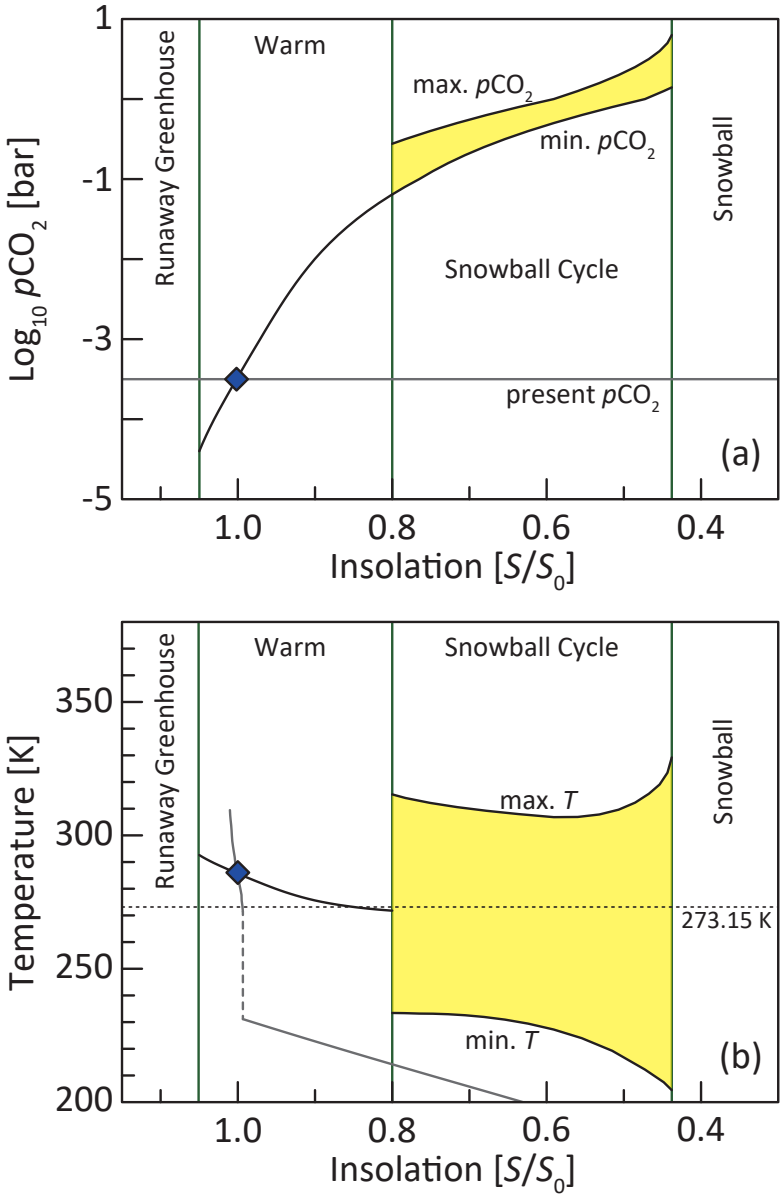

Figure 3.1: The steady state solutions of (a) pCO_2 and (b) the globally-averaged surface temperature against the insolation from the Sun which covers the habitable zone in the present solar system. The CO_2 degassing rate is assumed to be a constant value (equal to the present Earth's value). As shown, the climate in the habitable zone is divided into two climate modes. The gray lines represents the globally-averaged surface temperature when pCO_2 is constant at the present Earth's value for reference. The blue diamonds represent the Earth's condition at present.

3.1.2 Climate diversity in the habitable zone

Overall picture of climate diagram

Figure 3.2 shows the climate mode diagram as a function of the insolation and the CO_2 degassing rate due to volcanic activity. Both the horizontal and vertical axes are normalized by the present Earth's insolation (S_0) and the CO_2 degassing rate (F_{D0}), respectively. In addition to the four climate modes (runaway greenhouse climate, warm climate, snowball cycle, and snowball), there are another climate mode (warm climate cycle) and multiple climate modes condition.

Even within the habitable zone (i.e., the condition between the runaway greenhouse and snowball climate modes), either high insolation or a high CO_2 degassing rate is necessary in order for the hypothetical Earth to be in the warm climate or warm climate cycle modes: for example, if the hypothetical Earth is in the outer region of the HZ, the planet needs the CO_2 degassing rate higher than 2 F_{D0} in order to remain in the warm climate mode, otherwise it is in the snowball cycle mode.

As pointed out by previous works (Caldeira and Kasting, 1992; Kasting et al., 1993), high pCO_2 and low surface temperature may result in forming CO_2 clouds (see also Figure 3.3). However, an effect of the CO_2 clouds on radiative forcing is still unclear (Kasting et al., 1993; Forget and Pierrehumbert, 1997; Mischna et al., 2000). In Figure 3.2, insolation below which CO_2 cloud can be form at the pole is shown for reference.

Surface temperature and pCO_2 in the Warm climate mode

Figure 3.3 shows pCO_2 and globally-averaged surface temperature for the warm climate mode Earth. As explained with Figure 3.1, an increase in the insolation results in a decrease in pCO_2 owing to the Walker feedback; the decrease in pCO_2 suppress the increase in the surface temperature when the CO_2 degassing rate is constant. On the other hand, an increase in the CO_2 degassing rate results in an increase in pCO_2 if the insolation is constant, and the increase in pCO_2 also results in an increase the globally-averaged surface temperature.

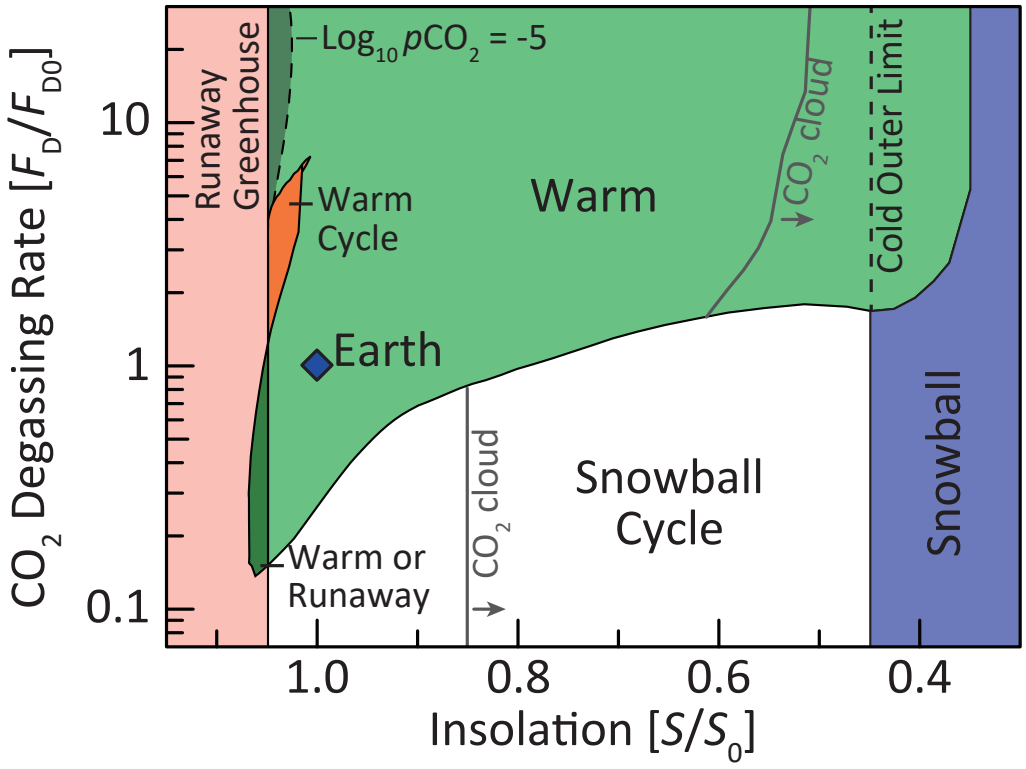

Figure 3.2: Climate mode diagram as functions of the insolation and CO_2 degassing rate. The black shaded region represents the condition where pCO_2 is below 1×10^{-5} bar (the minimum applicable limit of the model). The gray lines represent the insolation below which CO_2 cloud can be formed at the pole. The blue diamond represents the present Earth's condition. The habitable zone is between the runaway greenhouse and snowball climate modes. Note that the snowball cycle mode occupies most of the HZ when the CO_2 degassing rate is lower than roughly the present level of the Earth.

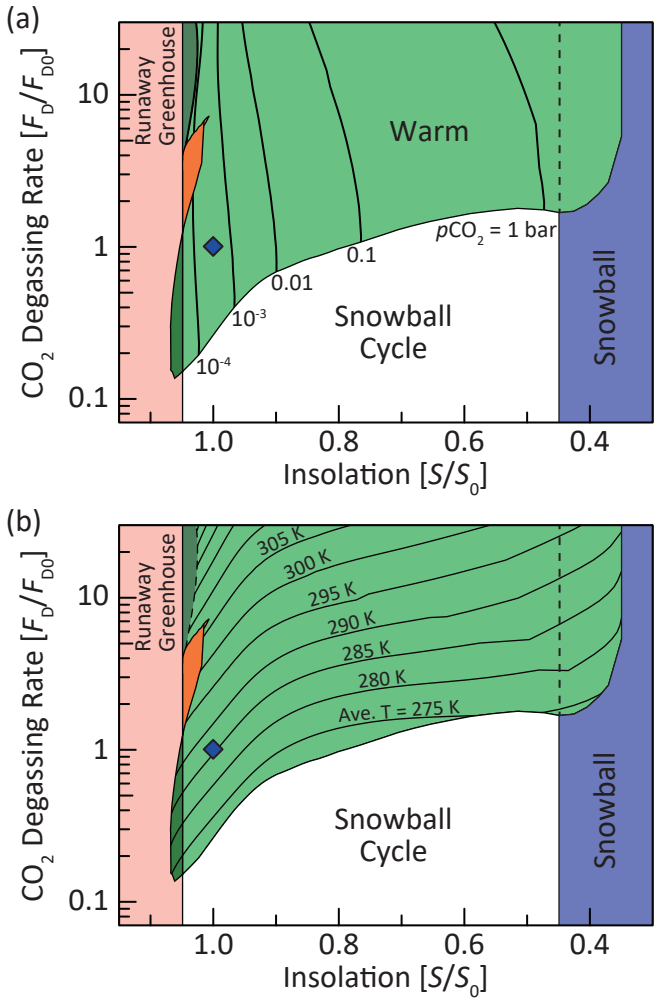

Figure 3.3: (a) The partial pressure of CO_2 in the atmosphere, and (b) the globally-averaged surface temperature as functions of the insolation and CO_2 degassing rate on the climate diagram (as same as that shown in Figure 3.2).

Snowball cycle and Warm climate cycle modes

In the "warm climate cycle" climate mode, the climate oscillates between the partially ice-covered and ice-free states as the climate in the snowball cycle mode oscillates between the snowball and warm climate states. Hereafter, these cycles are discussed in terms of multiple steady state solutions.

Figure 3.4 shows multiple climate steady state solutions for $S = 1$ and 1.04 S_0 and a CO_2 uptake rate which corresponds to each state.

When the insolation is S_0, there are the conditions for multiple steady states for 2.5×10^{-4} bar $< p\mathrm{CO}_2 < 3 \times 10^{-2}$ bar (Figure 3.4a), which is already pointed out by the previous works (e.g., North et al., 1981; Tajika, 2003): both the snowball state (the minimum latitude of the polar ice-cap (ice-line) is 0°; the blue solid line AB in Figure 3.4a) and the warm climate state (the ice-line > 0°; the red solid line CDE in Figure 3.4a) are the steady state in terms of the balance of energy. On the other hand, the black dashed line EB in Figure 3.4a represents an unstable solution due to the large ice-cap instability.

Figure 3.4b shows the relation between the CO_2 uptake rate and ice-line. When the planet is in the warm climate state, the CO_2 uptake rate is higher than 0.2 F_{D0} (the red line CDE in Figure 3.4b), and when the planet is in the snowball state, the CO_2 uptake rate is 0 (the point A in Figure 3.4b). The CO_2 uptake rate between 0 and 0.2 F_{D0} (the black dashed line AE in Figure 3.4b) corresponds to the unstable condition in terms of the energy balance (Figure 3.4a). On the other hand, the CO_2 uptake rate should balance with the CO_2 degassing rate in a steady state. If the CO_2 degassing rate is higher than 0.2 F_{D0}, a planet is in the warm climate state and in a steady state (i.e., the warm climate mode). However, if the CO_2 degassing rate is lower than 0.2 F_{D0}, the balance of the CO_2 flux cannot be achieved. As the CO_2 degassing rate decreases, the CO_2 uptake rate also decreases, and once $p\mathrm{CO}_2$ decreases lower than 2.5×10^{-4} bar, and the climate of the planet shifts from the warm climate state (the point E in Figures 3.4a and b) to the snowball state (the point E' in Figure 3.4a and the point A in b). In the snowball state, the CO_2 uptake rate (=0) is always lower than the CO_2 degassing rate, hence $p\mathrm{CO}_2$ increases with time. If CO_2 accumulate in the atmosphere more than 3×10^{-2} bar, the climate of the planet shifts from the snowball state (the point A in Figure 3.4b) to the warm climate state. Hence, the discontinuity of the CO_2 uptake rate owing to the

imbalance of energy budget is essential to the snowball cycle mode.

When the insolation is 1.04 S_0, there are multiple state solutions similar to those for $S = S_0$ (Figure 3.4c). As in the case for $S = S_0$, there is an unstable solution represented by the black dashed line BF in Figure 3.4c, which is derived from the large ice-cap instability in the climate system, and there is a corresponding discontinuity of the CO_2 uptake rate represented by the black dashed line AF in Figure 3.4c; this discontinuity results in the snowball cycle when the CO_2 degassing rate is lower than 0.2 F_{D0} as when the insolation is 1.0 S_0.

In the case for $S = 1.04S_0$, however, there is another unstable solution and discontinuity of CO_2 degassing rate, represented by the black dashed lines DE in Figures 3.4c and d. Suppose if the CO_2 degassing rate is between 2 F_{D0} and 5 F_{D0}, which corresponds to the discontinuity of the CO_2 uptake rate (Figure 3.4d, the CO_2 fluxes cannot balance. When the climate of the planet is initially in the ice-free state (the red line CD in Figure 3.4c and d), the CO_2 uptake rate is higher than the CO_2 degassing rate (Figure 3.4d). Then, pCO_2 decreases, and it finally reaches 5×10^{-5} bar, then the planet shifts from the ice-free state (the point D in Figures 3.4c and d) to the partially ice-covered state (the point D' in Figures 3.4c and d). In the partially ice-covered state, however, the CO_2 uptake rate is lower than the CO_2 degassing rate. Then, pCO_2 increases, and it finally reaches 7×10^{-5} bar, then the climate of the planet shifts from the partially ice-covered state (the point E in Figures 3.4c and d) to the ice-free state (the points E' in Figure 3.4c and d). The climate of the planet should repeat this cycle as long as the CO_2 degassing rate stays between 2 F_{D0} and 5 F_{D0}. This is defined here as the "warm climate cycle mode". The reason for the appearance of the unstable solution which results in the warm climate cycle is discussed later.

Duration of the snowball and warm climate states

In the snowball cycle mode, the hypothetical Earth fluctuates between the snowball and warm climate states. Figure 3.5a and b show the duration for which the hypothetical Earth remains in the snowball state (a "duration of the snowball state"; D_{sb}) and the warm climate state (a "duration of the warm climate state"; D_w), respectively. The increase in CO_2 degassing rate decreases the duration of the snowball state (Figure 3.5a). On the other hand, the increase in CO_2 degassing

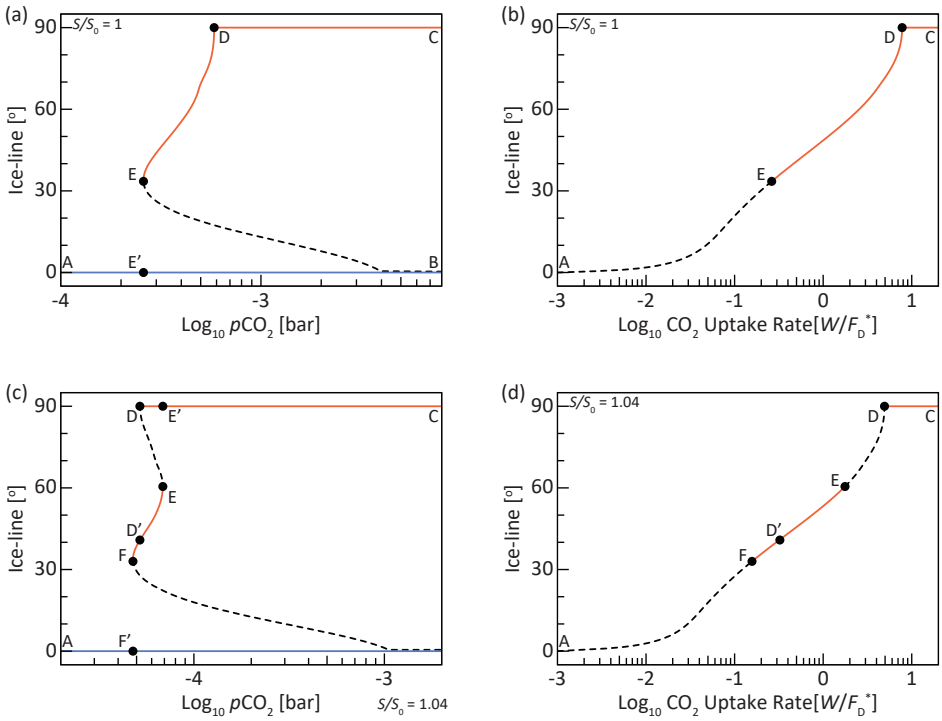

Figure 3.4: The relation between $p\mathrm{CO}_2$ and the latitudes of the termination of land polar ice caps (ice-line; (a) and (c)), and the relation between the CO_2 uptake rate and ice-line ((b) and (d)) for $S/S_0 = 1$ ((a) and (b)) and 1.04 ((c) and (d)). Red solid lines represent stable steady-state solutions for the balances of energy and CO_2 budgets. Blue solid lines represent stable steady-state solutions for the energy balance, although it is unstable owing to an imbalance of CO_2 budget. Black dashed lines represent unstable steady-state solutions. Note that ice-line is the latitude for $T = 273.15$ K.

rate increases the duration of the warm climate state (Figure 3.5b). Note that ignoring the change in the insolation and CO_2 degassing rate, the hypothetical Earth continuously remains in the warm climate state if the CO_2 degassing rate is above the critical CO_2 degassing rate between the snowball cycle and warm climate modes (i.e., if the hypothetical Earth is in the warm climate mode). A decrease in insolation increases the durations of both the snowball and warm climate states (Figure 3.5a and b) because a decrease in the insolation increases the difference in pCO_2 which is necessary for the climate jump between the snowball and warm climate states.

The duration of the snowball state is longer than the duration of the warm climate state as shown in Figure 3.5c: this figure shows the ratio between the durations of the snowball and warm climate states (i.e., $D_{\rm sb}/D_{\rm w}$), and high values shown in Figure 3.5c suggests that the duration of the snowball state is longer than the duration of the warm climate state. This is because the CO_2 uptake rate, in particular just after the deglaciation from the snowball state, is higher than the CO_2 degassing rate (note that an amount of CO_2 consumed during the warm climate state is equal to an amount of CO_2 accumulated during the snowball state). The high CO_2 uptake rate tends to result in the higher rate of net consumption of CO_2 during the warm climate state than the net accumulation rate of CO_2 during the snowball climate state (the CO_2 degassing rate). The high net consumption rate of CO_2 to the CO_2 degassing rate results in the shorter duration of the warm climate state than the duration of the snowball state. As a result, the hypothetical Earth in the snowball cycle mode is expected to be in the snowball state rather than in the warm climate state.

Warm and cold outer limits of the HZ

Figure 3.2 shows that there are two different limits for the outer limit of the HZ: one is at 0.35 S_0, which corresponds to the boundary between the warm and snowball climate modes, and the another is at 0.44 S_0, which corresponds to the boundary between the snowball cycle and snowball climate modes. The former limits (hereafter, referred to as a "warm outer limit of the HZ") corresponds to the maximum greenhouse limit proposed in the previous studies (0.34–0.36 S_0: Kasting et al., 1993; Kopparapu et al., 2013).

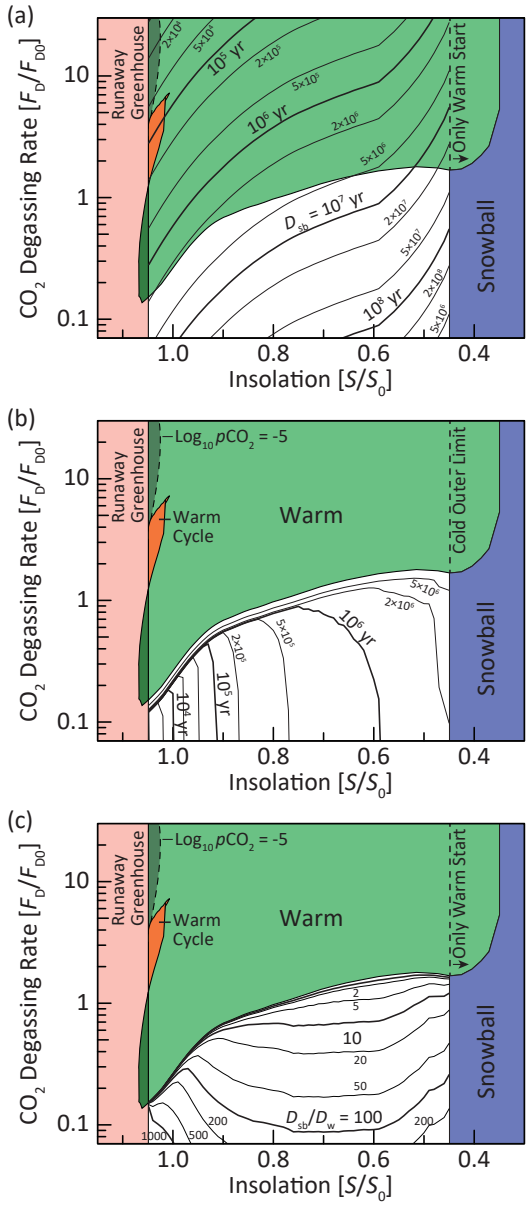

Figure 3.5: Duration of (a) the snowball state (D_{sb}) and (b) the warm climate state (D_{w}), and (c) the ratio of the duration of the snowball state to the warm climate state ($D_{\mathrm{sb}}/D_{\mathrm{w}}$).

The warm outer limit of the HZ is defined as the minimum insolation where a hypothetical Earth can keep the warm climate state. The reason why such a minimum insolation exists is that an effective insolation has a minimum (Kasting et al., 1993; Kopparapu et al., 2013). Note that the effective insolation is defined as a planetary radiation divided by co-albedo $(1 - A)$ and that the effective insolation should balance with insolation in a steady state. The blue curve in Figure 3.6 represents the relation between $p\mathrm{CO}_2$ and the effective insolation for the critical condition from the warm climate to snowball state, which is qualitatively the same as Figure 4 of Kasting et al. (1993) and Figure 5 of Kopparapu et al. (2013). As explained in the previous works, an increase in $p\mathrm{CO}_2$ results in a decrease in the effective insolation for the critical condition from the warm climate to snowball climate state owing to an decrease in a planetary radiation due to an increase in the greenhouse effect of the atmosphere until $p\mathrm{CO}_2$ becomes a certain level (> 6 bar in this study). Then, the increase in $p\mathrm{CO}_2$ results in an increase in the effective insolation because the planetary radiation saturates owing to the condensation of atmospheric CO_2, and also because the Rayleigh scattering via the atmospheric CO_2 increases (e.g., Kasting et al., 1993; Kopparapu et al., 2013). Therefore, the effective insolation for the critical condition from the warm climate to snowball climate becomes minimum (0.35 S_0; Figure 3.6). If the insolation is larger than the minimum value (0.35 S_0), a hypothetical Earth can be in the warm climate mode, otherwise it is in the snowball climate mode (e.g., Kasting et al., 1993; Kopparapu et al., 2013).

As discussed in the previous works, the condensation of CO_2 and the formation of CO_2 cloud may change the warm outer limit of the HZ, but it is still uncertain; the estimate ranges from of 0.17 to 0.53 S_0 (e.g., Kasting et al., 1993; Forget and Pierrehumbert, 1997; Mischna et al., 2000). The actual effects of CO_2 clouds depend on the size distribution of cloud particles, extent of cloud cover, and location, height, and optical depth of the cloud.

The boundary between the snowball cycle and snowball climate modes is hereafter, referred to as a "cold outer limit of the HZ", which is defined as the minimum insolation where a hypothetical Earth can shift from the snowball state back to warm climate state owing to the accumulation of the atmospheric CO_2 via the carbonate-silicate geochemical cycle. In other words, if the insolation is too low, the hypothetical Earth with the carbonate-silicate geochemical cycle cannot

go back to a warm climate state from a snowball state. The cold outer limit of the HZ is resulted from the fact that the effective insolation for the critical condition "from the snowball to warm climate" state has a minimum value (the red curve in Figure 3.6) as the warm outer limit of the HZ is resulted from the fact that the effective insolation for the critical condition "from the warm climate to snowball" state (the blue curve in Figure 3.6).

The difference between the warm and cold outer limits of the HZ, in other words, the difference between the effective insolation for the two critical conditions (the blue and red curves in Figure 3.6), is due to the difference in the surface albedo of the hypothetical Earth: ice albedo for the cold outer limit of the HZ, assuming a cold start of the planet (the initial state of the planet is a snowball state), and the value lower than the ice albedo for the warm outer limit of the HZ, assuming the warm start of the planet (the initial state of the planet is a warm climate state).

The climate of the hypothetical Earth between the warm and cold outer limits of the HZ has hysteresis. If the insolation is lower than the cold outer limit, the climate of the hypothetical Earth cannot shift from the snowball state to the warm climate state no matter how high $p\mathrm{CO}_2$ is. Hence, even the hypothetical Earth whose CO_2 degassing rate is high enough for the warm climate mode is in the snowball climate mode if the initial state of the planet is the snowball state.

Multiple climate modes at the inner limit of the habitable zone

According to Kopparapu et al. (2013, 2014), the runaway greenhouse limit is 1.05 S_0. However, as shown in Figure 3.2 (the dark green region), there is multiple climate modes in the condition beyond the runaway greenhouse limit ($S > 1.048S_0$). In these conditions, a hypothetical Earth can be in the runaway greenhouse or warm climate mode. For example, when $\log_{10} p\mathrm{CO}_2$ is -4.5 (i.e., $p\mathrm{CO}_2 = 3.2 \times 10^{-5}$ bar) and S is $1.048S_0 < S < 1.054S_0$, a planet can be either in the runaway greenhouse climate mode (the red dashed line) or the warm climate mode (the red solid line CD in Figure 3.7a). The difference is planetary albedo: the average planetary albedo for the warm climate mode (the line CD) is between 0.31 and 0.41, while the average planetary albedo at the critical condition between the runaway greenhouse and warm climate modes (the point A in Figure 3.7a) is 0.21. This is due to the existence of the partial ice-cap. The relatively high planetary

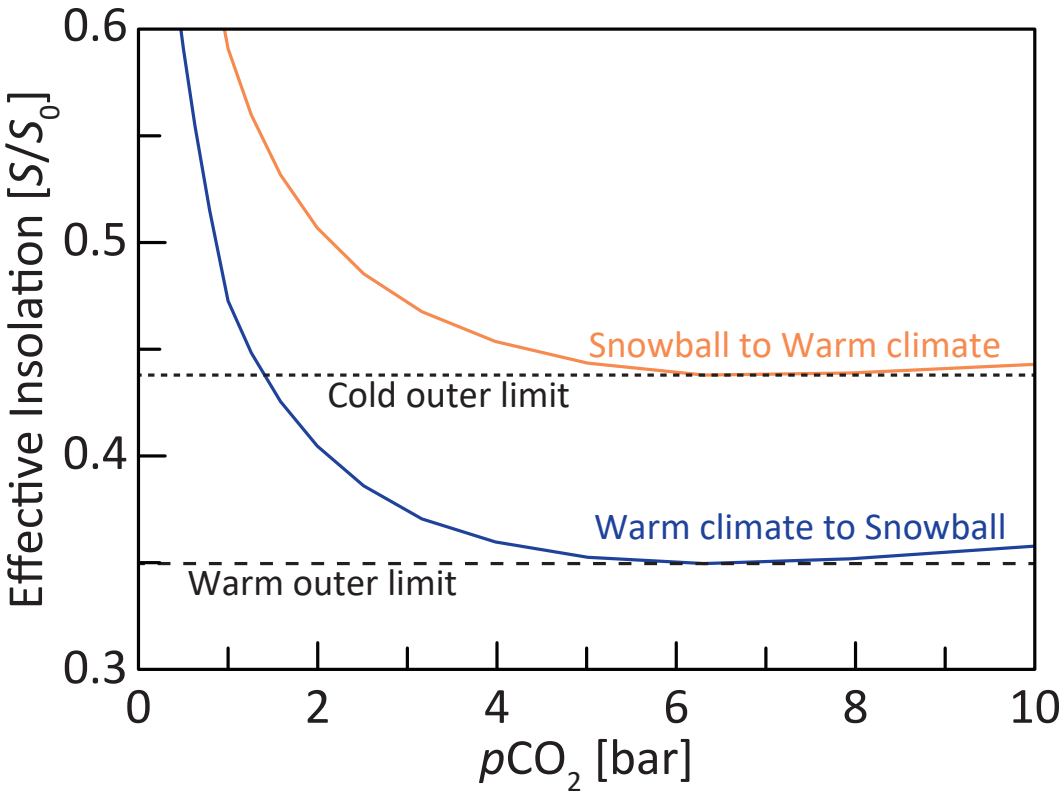

Figure 3.6: The relation between $p\mathrm{CO}_2$ and insolation between the snowball and warm climate states. The blue curve represents the critical condition from the warm climate to snowball states, which corresponds to Figure 4 of Kasting et al. (1993) and Figure 5 of Kopparapu et al. (2013), and the red curve represents the critical condition from the snowball to warm climate states. The dashed and dotted lines represent the warm and cold outer limit of the HZ, respectively.

albedo should suppress the effective insolation, and avoid the hypothetical Earth from being the runaway greenhouse climate mode.

Although there is such a condition for the multiple climate modes, a most of the Earth and Earth-like planets under such a condition may be in the runaway greenhouse climate mode, rather than in the warm climate mode. This is because a hypothetical Earth in such a condition is easy to shift from the warm climate mode to the runaway greenhouse climate mode, but is unable to shift from the runaway greenhouse climate mode to the warm climate mode. For example, as shown in Figure 3.7a and b, an increase in the insolation ($p\mathrm{CO}_2$) may result in the shift from the partial ice-covered solution (the warm climate mode) to the ice-free solution (the runaway greenhouse climate mode in this case) (from the point C to C' in Figure 3.7a, or from the point B to B' in Figure 3.7b). On the other hand, a decrease in the insolation ($p\mathrm{CO}_2$) may result in the shift to the snowball solution (from the point D to D' in Figure 3.7a, or from the point A to A' in Figure 3.7b), but the increase of the insolation ($p\mathrm{CO}_2$) may eventually result in the shift to the ice-free solution (i.e., the runaway greenhouse climate mode). Hence, both the increase and decrease in insolation or $p\mathrm{CO}_2$ may result in the shift to the runaway greenhouse climate mode. The former is intuitively understandable because the increase in either insolation or $p\mathrm{CO}_2$ results in the warmer state. The latter is because a planet shifts from the snowball state only to the ice-free state (i.e., the runaway greenhouse state in the range which is considered here) owing to the high $p\mathrm{CO}_2$.

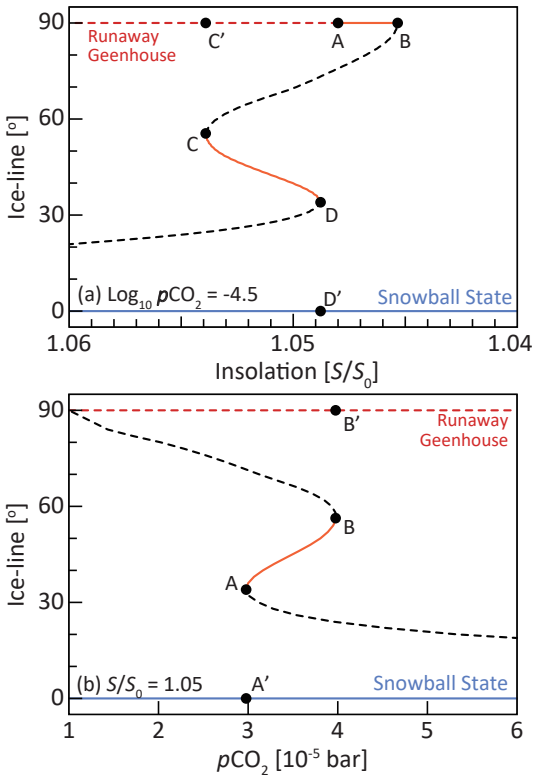

Figure 3.7: (a) The relation between insolation and ice-line under the condition of $\log_{10} pCO_2 = -4.5$, and (b) The relation between pCO_2 and ice-line under the condition of $S = 1.05S_0$. Red dashed line represents an ice-free solution, which corresponds to the runaway greenhouse climate mode. Red solid curve represents a stable, partial ice-covered solution, which corresponds to the warm climate mode. Blue solid line represents a snowball solution, which corresponds to the snowball cycle mode in which the CO_2 budget is not balanced but the energy budget is balanced. Black dashed lines represent unstable solutions.

3.2 Evolution of surface environments

In this section, the results for the evolution of the climate of the Earth and Earth-like planets considering the stellar evolution and the thermal evolution of the planet, is shown.

3.2.1 Evolution of CO_2 degassing rate and solar luminosity

Figure 3.8 shows the evolution of the average mantle temperature, the mantle viscosity, the heat flow from the mantle of the Earth, the melt production depth, the seafloor spreading rate, and the melt production volume. The average mantle temperature decreases monotonically with time (Figure 3.8a), which increases the mantle viscosity (Figure 3.8b). The decrease in the mantle temperature, combined with the increase in viscosity, results in the reduction of heat flow from the mantle (Figure 3.8c). The decreases in the mantle temperature and the heat flow from the mantle result in the decrease in the melt production depth and the seafloor spreading rate (Figure 3.8d and e). The decreases in the melt production depth and the seafloor spreading rate result in the decrease in the melt production rate. As a result, the CO_2 degassing rate is estimated to decrease monotonically with time (the blue line in Figure 3.9). In addition, Figure 3.9b compares theCO_2 degassing rate during the Phanerozoic: the blue line is the same as Figure 3.9a, the gray line is estimated using paleo-sea level and hotspot displacement (Berner, 1994), and the black line is estimated using the paleo-geography (Vérard et al., 2015). The evolutions of the CO_2 degassing rate based on the geological data also tend to decrease with time although they fluctuate on a timescale of 10^8 years or shorter. The effect of the fluctuation is discussed later. On the other hand, the solar luminosity increases with time (the red line in Figure 3.9).

3.2.2 Evolution of climate mode

Figure 3.10a shows the evolutionary tracks of the climate of a hypothetical Earth with various semi-major axis, i.e., the evolution of the insolation and the CO_2 degassing rate, overlaying on the climate diagram (Figure 3.2). For the Earth (i.e., the semi-major axis is 1 AU), the decrease in the CO_2 degassing rate and the increase in the insolation compensates with each other, and the climate remains in

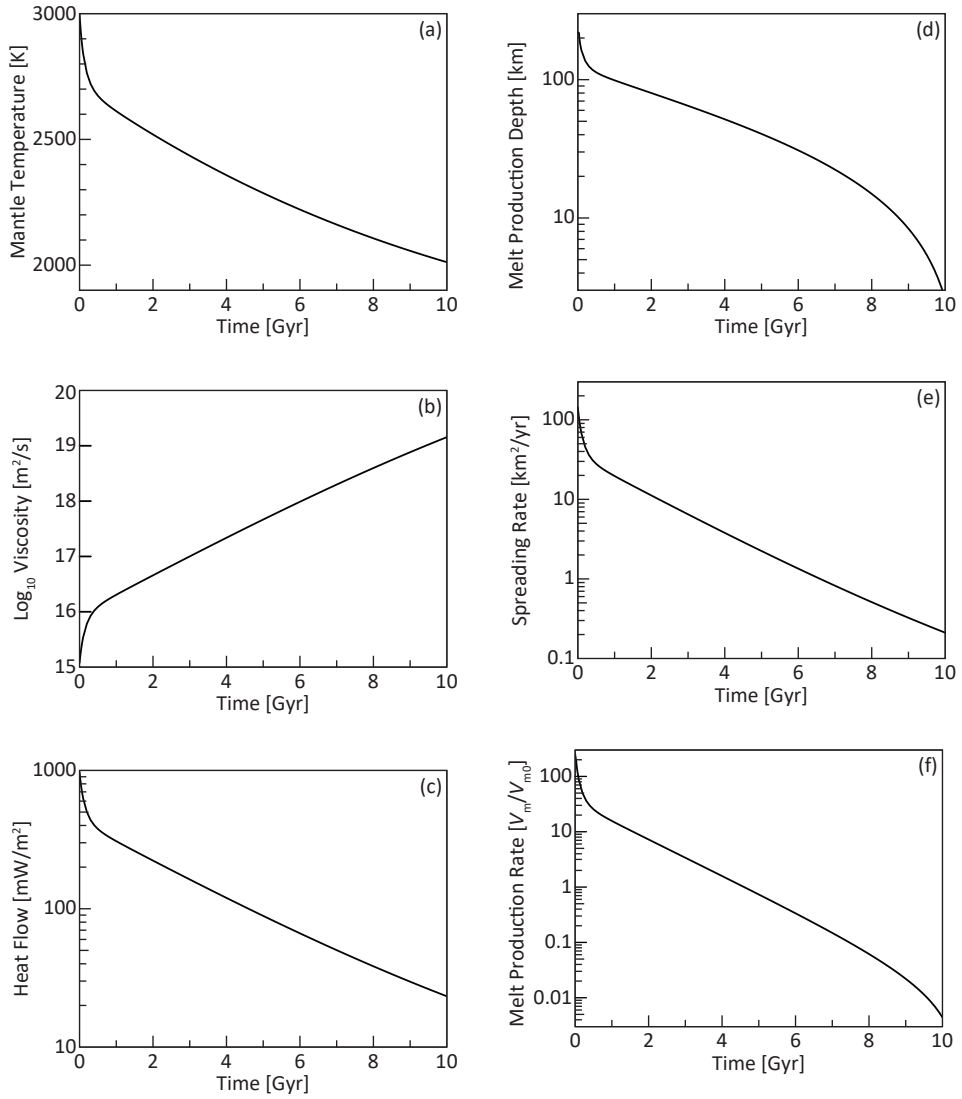

Figure 3.8: The evolution of (a) mantle temperature, (b) mantle viscosity, (c) heat flow from the mantle, (d) melt production depth, (e) seafloor spreading rate, and (f) melt production rate. The decrease in the mantle temperature increases the mantle viscosity, resulting in the decrease in the heat flow. The decrease in the mantle temperature decreases melt production depth, and the decrease in the heat flow decreases the seafloor spreading rate. These change results in the decrease in the melt production rate and the CO_2 degassing rate.

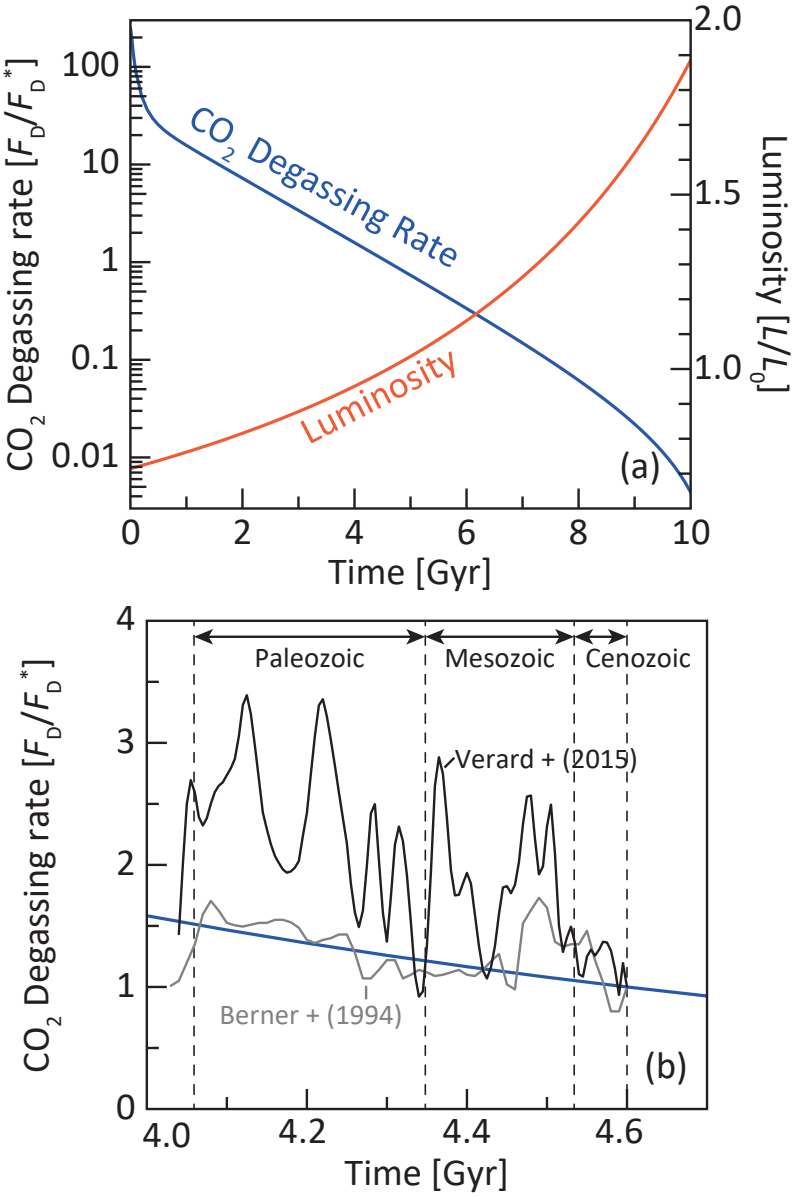

Figure 3.9: (a) The evolution of CO_2 degassing rate (blue curve) and solar luminosity (red curve. The CO_2 degassing rate decreases with time owing to the decrease in the melt production volume (Figure 3.8f), on the other hand, the luminosity increases with time. (b) Comparison the CO_2 degassing rates: a blue curve is the estimate of this study, a gray curve is the one estimated using paleo-sea level and hotspot displacement (Berner, 1994), and a black curve is the one estimated using paleo-geography (Vérard et al., 2015).

the warm climate mode for the first 5.2 Gyr. When the insolation increases to the inner limit of the HZ, the climate of the Earth becomes in the runaway greenhouse climate mode.

If the Earth is closer to the Sun, although it is in the HZ (e.g., at 0.9 AU), it may pass the warm climate cycle mode conditions, and shifts to the runaway greenhouse climate mode much earlier (< 3 Gyr) than the Earth at 1 AU (~ 5 Gyr).

On the other hand, if the Earth is farther from the Sun, but the initial insolation is larger than the warm outer limit of the HZ (e.g., at 1.2 AU), its initial climate is the warm climate mode because the initial CO_2 degassing rate is high, but the decrease in the CO_2 degassing rate with time results in the shift to the snowball cycle mode (~ 4 Gyr).

In addition, if the initial insolation is lower than the warm outer limit of the HZ (e.g., at 1.5 AU), the initial climate is the snowball climate mode (i.e., the hypothetical Earth remains in the snowball state). Then, the planet may pass the warm climate mode condition owing to the increase in the luminosity. However, if the insolation is lower than the cold outer limit of the HZ (0.45 S_0), the planet cannot shift from the snowball state to the warm climate state: in other words, the planet remains in the snowball climate mode. When the insolation increases above the cold outer limit of the HZ, the CO_2 degassing rate decreases below the critical values between the warm and snowball climate modes. The planet may, therefore, shift from the snowball climate mode to the snowball cycle mode, not to the warm climate mode.

The habitable zone is supposed to shift outward from the Sun with time owing to the solar evolution (i.e., the increase in the luminosity) (Kasting et al., 1993). The boundary for the runaway greenhouse climate mode (i.e., the inner limit for the HZ) should also shift outward from the Sun. Therefore, the closer to the Sun, the earlier the climate shifts to the runaway greenhouse climate mode (Figure 3.10b). However, while the boundary for the snowball climate mode does not shift for the first several billion years, the warm outer limit of the HZ (the black dashed line) shifts outward (Figure 3.10b). This is because the cold start planet (in other words, the planet located out of the HZ at first) cannot shift to the warm climate mode until the insolation increases above the cold outer limit of the HZ. In addition, even if the Earth is in the HZ, it shifts to the snowball cycle mode at several Gyr and then cannot keep the warm climate state owing to the decrease in the CO_2

degassing rate. The typical timescale for the shift to the snowball cycle mode is ~ 4 Gyr (e.g., Figure 3.10), and the semi-major axis at which the Earth remains in the warm climate mode longer than this timescale is limited to the inner region of the initial HZ.

Figure 3.11 shows the evolution of $p\mathrm{CO}_2$ and globally-averaged surface temperature for the Earth orbiting at 0.9 AU, 1 AU and 1.2 AU. The planets are assumed to start in the warm climate mode. The dashed lines represent the time at which the planet shift from the warm climate mode to the other climate modes. The partial pressure of the atmospheric CO_2 decreases monotonically owing to the increase in the luminosity and the decrease in the CO_2 degassing rate at any semi-major axis (Figure 3.11a). The globally-averaged surface temperature decreases rapidly at first (Figure 3.11b) owing to the rapid decrease in the CO_2 degassing rate. If the Earth is in the outer region of the HZ (e.g., at 1.2 AU), the globally-averaged surface temperature keeps decreasing, and the planet shifts to the snowball cycle mode (Figure 3.11b). On the other hand, if the Earth is in the inner region of the HZ (e.g., at 0.9 AU and 1 AU), the globally-averaged surface temperature bottoms out and increase, and the planet shift to the runaway greenhouse or warm climate cycle mode (Figure 3.11b).

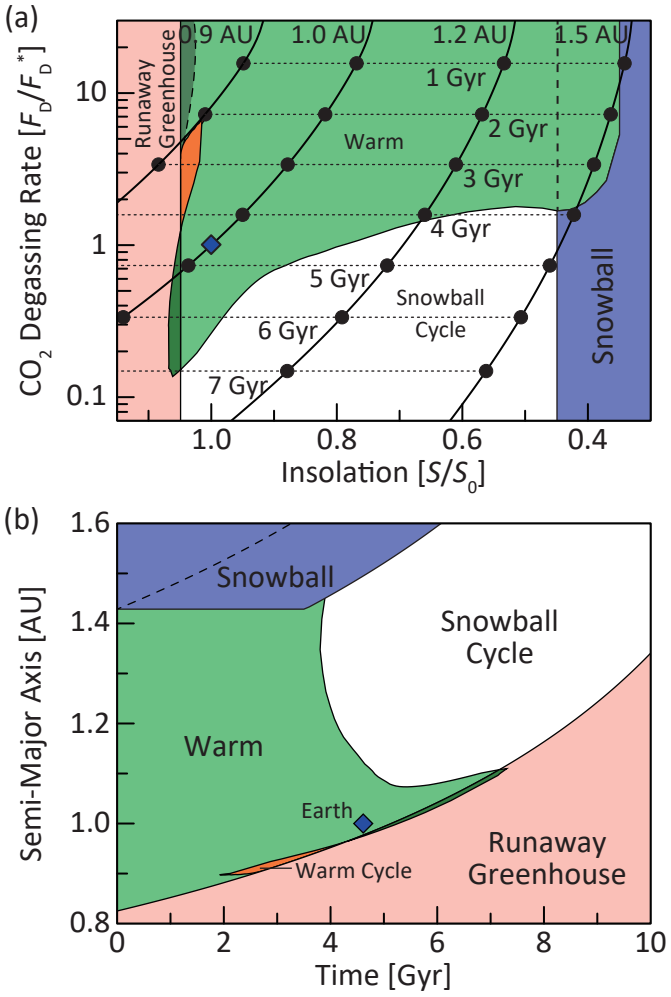

Figure 3.10: The evolution of the climate of the Earth. (a) The evolutionary tracks on the climate diagram (Figure 3.2). The black circles and black dotted lines represent time. (b) The evolution of the climate as functions of the semi-major axis and time. The black dashed line represents the evolution of the warm outer limit of the HZ and corresponds to the evolution of the maximum greenhouse limit of Kasting et al. (1993)

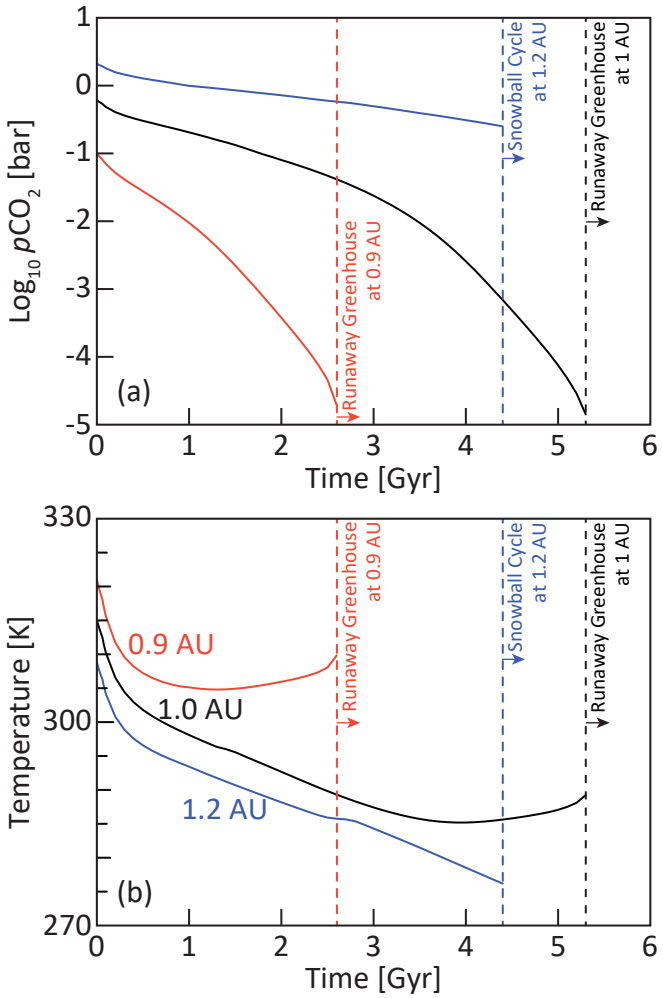

Figure 3.11: The evolution of (a) $p\mathrm{CO}_2$ and (b) globally-averaged surface temperature for the Earth at 0.9 AU, 1 AU and 1.2 AU while it is in the warm climate mode. The dashed lines represents the time at which the planet shift from the warm climate mode to the other climate modes (i.e., the runaway greenhouse, the warm climate cycle, or the snowball cycle modes).

Section 4

Discussion

4.1 Critical condition between the warm and cold climate modes

In this section, a "critical condition of the warm climate mode" is discussed: hereafter, the "critical" condition represents a condition between the warm and cold climate modes (the snowball cycle and snowball climate modes are collectively referred here to as the "cold climate modes"). In other words, the critical condition of the warm climate mode is the coldest condition in the warm climate mode.

4.1.1 Critical CO_2 degassing rate of the warm climate mode

As shown in Figure 3.2, the gradient of the boundary between the warm climate and cold climate modes in the logarithm of the critical CO_2 degassing rate and the insolation diagram is very narrow in the outer region of the HZ (i.e., low insolation condition), while the gradient is steep in the outer region of the HZ (i.e., high insolation condition). Owing to this characteristic feature, the timescale for the shift from the warm climate to snowball cycle modes is almost constant at 4 Gyr in the outer region of the HZ (Figure 3.10b).

The critical CO_2 degassing rate for a given insolation is determined by pCO_2 at the critical condition. This is because the critical CO_2 degassing rate is equal to the CO_2 uptake rate for the critical condition in a steady state, and because, considering the critical condition, only the pCO_2 changes owing to a decrease of

the insolation among the parameters which affects the CO_2 uptake rate (i.e., pCO_2, surface temperature, and the ice-line; see also Equation 2.29).

First, the factors related to the CO_2 uptake rate (i.e., pCO_2, surface temperature, and the ice-line) at the critical condition are shown in order to reveal that the dependence of the pCO_2 on the insolation is much higher than those of the other factors considering the critical condition. Figure 4.1 shows three factors (pCO_2, surface temperature, and ice-line) at the critical condition of the warm climate mode against the insolation. A reduction in the insolation results in an increase in pCO_2 owing to the Walker feedback (Figure 4.1a), and the globally-averaged surface temperature is roughly constant (273 ± 2 K) and almost independent of the insolation (Figure 4.1b).On the other hands, with the decrease in the insolation, the maximum temperature on the surface (typically, the equatorial regions) decreases while the minimum temperature (typically, the polar regions) increases, hence, the decrease in the insolation results in a decrease in the difference in the surface temperature (Figure 4.1b). This is because the decrease in the insolation also results in a decrease in the difference between the insolation at the top of the atmosphere at the equatorial region and at the polar regions and because the increase of pCO_2 due to the decrease in an insolation results in the increase of the meridional heat transport (Equation 2.15; Gierasch and Toon, 1973). The increase in the meridional heat transport tends to prohibit a partially ice-covered state; in other words, the steady state of the Earth is either the ice-free or snowball states owing to the balance of energy when the insolation is low. Therefore, the decrease in the insolation increases the critical ice-line (Figure 4.1c).

Second, the effect of the three factors on the CO_2 uptake rate is discussed in order to reveal that the CO_2 uptake rate at the critical condition depends on the pCO_2 rather than other factors considering the critical condition. As explained above, a decrease in the insolation results in an increase in pCO_2 of the critical condition of the warm climate mode, which results in an increase in the critical CO_2 uptake rate (= the critical CO_2 degassing rate in a steady state). The change in the maximum temperature (Figure 4.1b) indicates that the decrease in the insolation also decreases the surface temperature on ice-free lands, which results in a decrease in the critical CO_2 degassing rate. Note that an increase in the surface temperature on ice-covered land (e.g., an increase in the minimum temperature) with the reduction of the insolation, which compensates the decreases in the

maximum temperature and results in the almost constant globally-averaged surface temperature, does not affect the CO_2 uptake rate (= the CO_2 degassing rate). The change in the ice-line also indicates that the decrease in the insolation results in an increase the area of ice-free lands, which results in an increase in the critical CO_2 uptake rate (= the critical CO_2 degassing rate). However, the large change in the ice-covered area occurs in the outer region of the HZ (the insolation is roughly less than $0.4S_0$; Figure 4.1c). Therefore, the areal change of ice-covered lands does not affect the critical CO_2 uptake rate (= the critical CO_2 degassing rate) in the inner region of the HZ. In addition, the increase in $p\mathrm{CO}_2$ results in an increase in the critical CO_2 degassing rate by a factor of 60 in the HZ, while the surface temperature on ice-free land decreases the rate by a factor of 3. Hence, it can be said that the critical CO_2 degassing rate depends mainly on the critical $p\mathrm{CO}_2$.

In the following, in order to understand the relationship between the insolation and the critical $p\mathrm{CO}_2$ in more details, the critical $p\mathrm{CO}_2$ is re-calculated using a 0-dimensional energy balance model (the 0-D EBM, hereafter, called as a "simple model") for simplicity. The simple model is represented as follows:

$$(1 - A(T, p\mathrm{CO}_2))\frac{S}{4} = I(T, p\mathrm{CO}_2). \tag{4.1}$$

where the planetary radiation, I, and planetary albedo, A, are the same as those used in the 1D-EBM (hereafter, called a "standard model"). As explained above, the globally-averaged surface temperature and ice-line of a critical condition are almost independent of the insolation (Figure 4.1b and c). Therefore, the surface temperature is set to be 273 K, and the surface albedo is also assumed constant which is determined so that the simple model may reproduce the same critical $p\mathrm{CO}_2$ at $S = S_0$ as the value calculated by the standard model. Then, Equation 4.1 can be deformed as follows:

$$S = \frac{4I(p\mathrm{CO}_2)}{1 - A(p\mathrm{CO}_2)}. \tag{4.2}$$

The relationship between the insolation and critical $p\mathrm{CO}_2$ can be understood in terms of the relationships between $p\mathrm{CO}_2$ and planetary radiation, and also between $p\mathrm{CO}_2$ and a planetary albedo.

Figure 4.2a shows the relationships between the insolation and $p\mathrm{CO}_2$ estimated

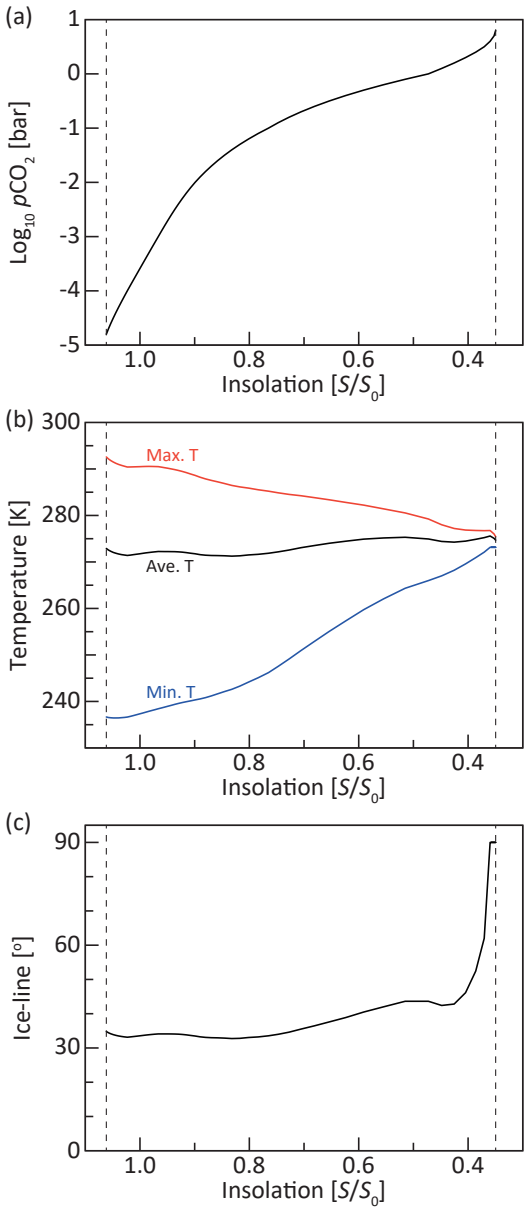

Figure 4.1: The critical condition between the warm and snowball climate modes: (a) pCO_2, (b), maximum, minimum, and globally-averaged surface temperatures, and (c) ice-line as functions of insolation. The dashed lines represent the inner limit (1.048 S_0) and the warm outer limit (0.35 S_0).

by the simple and standard models: the relationship estimated by the simple model (the red line) is consistent with the relationship by the standard model (the black dashed line, which is the same as shown in Figure 4.1a). The slight difference as seen for $S < 0.4S_0$ is owing to the changes in the ice-line: the ice-line steeply increases with the decrease in the insolation around the outer limit of the HZ (Figure 4.1c), which is not reproduced by the simple model. As a result, the surface albedo at the critical condition does not increases much in the simple model, hence, $p\mathrm{CO}_2$ estimated is slightly larger than that by the standard model (Figure 4.2a).

Figures 4.2b and c show planetary radiation and a planetary albedo at the critical condition as a function of the critical $p\mathrm{CO}_2$. An increase in the critical $p\mathrm{CO}_2$ results in a decrease in the planetary radiation (Figure 4.2b); on the other hand, the decrease in the critical $p\mathrm{CO}_2$ results in an increase in the planetary albedo owing to the increase in the Rayleigh scattering via CO_2 (Figure 4.2c). However, an effect on the insolation of the change in the planetary albedo, which is by a factor of about 1.2, is smaller than that of the planetary radiation, which is by a factor of 3.6. Hence, the relationship between the insolation and the critical $p\mathrm{CO}_2$ mainly depends on the relationship between the planetary radiation and $p\mathrm{CO}_2$ (i.e., the greenhouse effect of $p\mathrm{CO}_2$).

As a conclusion, the relationship between the insolation and critical CO_2 degassing rate depends mainly on the greenhouse effect of $p\mathrm{CO}_2$. An increase of the greenhouse effect due to the increase in $p\mathrm{CO}_2$ from 1×10^{-5} bar to 1×10^{-4} bar is naturally less than the increase in $p\mathrm{CO}_2$ from 0.1 bar to 1 bar (Figure 4.2b). Hence, a decrease in the insolation results in an increase in a logarithm of the critical $p\mathrm{CO}_2$ (and the critical CO_2 degassing rate) more steeply for highs insolation than that for low insolation (Figure 4.2a and 3.2).

4.1.2 Effect of size and distribution of continents

A decrease in land area results in an increase in $p\mathrm{CO}_2$ and globally-averaged surface temperature owing to a decrease in an efficiency of the CO_2 uptake rate (e.g., Walker et al., 1981; Marshall et al., 1988; Tajika and Matsui, 1992). According to Marshall et al. (1988), assembly of continents in the polar region results in the high $p\mathrm{CO}_2$ and high globally-averaged surface temperature, while assembly

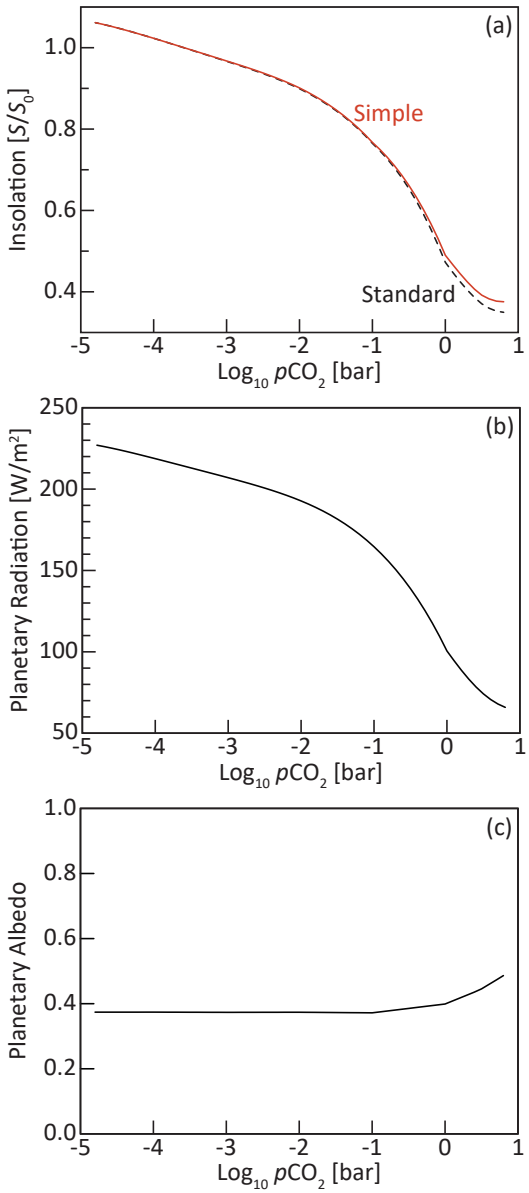

Figure 4.2: (a) Critical $p\mathrm{CO}_2$ calculated by a zero-dimensional energy balance model (red line). Black dashed line represents the critical $p\mathrm{CO}_2$ calculated by the standard model (i.e., it is same as Figure 4.1a). (b) Planetary radiation and (c) a planetary albedo as functions of $p\mathrm{CO}_2$.

of continents in the equatorial region results in the low $p\mathrm{CO}_2$ and low globally-averaged surface temperature. In this section, dependencies of a critical CO_2 degassing rate for the snowball cycle mode on the continental size and distribution are discussed.

Figure 4.3 shows the effect of land distribution on the climate stabilities of the Earth for $S = S_0$: in Figure 4.3, black lines represent a "uniform" distribution of land where the land fraction is 0.3 at any latitude, green lines represent an "Earth-like" distribution where land distribution is same as that of the present Earth, the blue lines represent a "polar" distribution, where lands assemble in the polar region, and red lines represent an "equatorial" distribution where lands assemble in the equatorial region (see Figure 4.3a). The difference between the uniform and Earth distributions is small compared with the other differences (Figure 4.3b and c). The assembly of lands in the polar region retreats the ice-line (i.e., the increases the globally-averaged surface temperature; Figure 4.3c) and increases $p\mathrm{CO}_2$ (Figure 4.3b) as pointed out by Marshall et al. (1988).

As explained above, the ice albedo feedback makes low ice-line solutions (the dashed lines of ice-line lower than about 30° in Figure 4.3b) unstable, resulting in discontinuities in a CO_2 uptake rate for the uniform, Earth-like and equatorial distributions (the dashed lines in Figure 4.3c); these discontinuities result in the snowball cycle mode (Section 3.1.2). To the contrary, for the polar distribution, there is no discontinuity in the CO_2 uptake rate (Figure 4.3c). This is because the lands assemble in latitudes higher than the critical latitude of ice-line (the boundary between the solid and dashed lines in Figure 4.3b). In other words, the decrease in the CO_2 degassing rate does not result in the climate jump from the warm climate to the snowball states. Hence, the assembly of lands in high latitude may tend to preclude a planet from being the snowball cycle mode.

Figure 4.4a shows the critical CO_2 degassing rates for various fraction of land area (land fraction; $f_{\mathrm{land}} \equiv 1 - f_{\mathrm{o}}$) with the uniform distribution. The larger the land fraction is, the higher the critical CO_2 degassing rate is, which is consistent with Marshall et al. (1988). Focusing on the critical condition, the globally-averaged surface temperature and ice-line is almost independent of the insolation (see also Figure 4.1). On the other hand, $p\mathrm{CO}_2$ depends on the insolation and the land fraction (Figure 4.4b). This is because the surface albedo of land is higher than that of ocean especially at low latitude, then higher $p\mathrm{CO}_2$ is necessary in order to

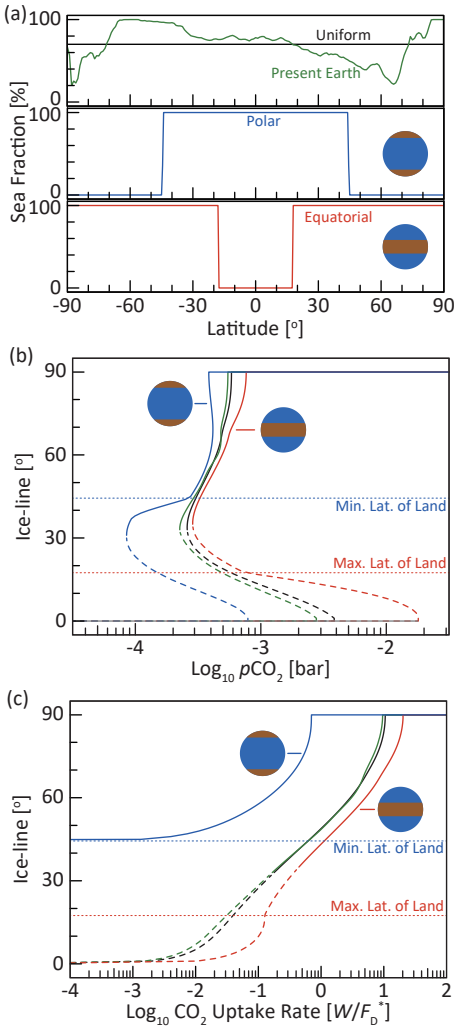

Figure 4.3: (a) Sea distribution as a function of latitude, and ice-line as functions of (b) insolation and (c) CO_2 uptake rate. Black, green, blue, and red lines represent a "uniform", "Earth-like", "polar", and "equatorial" distribution, respectively. Dashed lines represent unstable states in terms of balance of energy, and gray line represents the snowball state. Blue and red dotted lines represent the minimum latitude of lands for the polar distribution and the maximum latitude of lands for the equatorial distribution, respectively.

keep the warm climate state for the case of higher land fraction. As a result, the critical CO_2 degassing rate depends strongly on the land fraction. For example, if the critical CO_2 degassing rate is fitted with a power function of the land fraction, the exponent is 1.44, which is larger than the value indicated by Equation 2.29.

However, these calculations would overestimate the dependency on the land fraction because the difference in the land fraction may change the distribution of precipitation and evaporation (i.e., runoff). When the land fraction is small, each continent tends to be small. In such a case, there are much runoff in relatively large fraction of continents, which may increase the effective land area where the silicate weathering occurs. On the other hand, when the land fraction is large, each continent tends to be large. In such a case, inland climate may be dry with a very small precipitation, which may decrease the effective land area where the silicate weathering occurs. The distribution of runoff depends largely on geography and atmospheric dynamics, hence general circulation models (GCMs) will be required for further discussion.

4.2 Warm climate cycle mode

The warm climate cycle mode is resulted from a discontinuity of CO_2 uptake rate which is derived from unstable solutions with small ice-caps (the state where ice-line is at high latitude; Figure 3.4). An existence of such small ice-cap unstable solutions is known as a small ice-cap instability in previous works (e.g., North, 1975, 1984; Cahalan and North, 1979). The small ice-cap instability is caused by the ice albedo feedback, but is known as highly model dependent: the small ice-cap instability disappears if it is modeled so that the albedo may smoothly increase around the freezing point (e.g., Cahalan and North, 1979), or if the equinox insolation distribution (the insolation distribution in the case where the obliquity is zero) is given (e.g., North, 1975). This is because a change of an albedo at high latitude does not affect the net insolation significantly. However, the small ice-cap unstable solutions obtained in this study have different characteristic features from the unstable solution caused by the small ice-cap instability. It is indicated that a feedback other than the ice albedo feedback causes the small ice-cap unstable solutions.

Figure 4.5 shows relations between the insolation and ice-line when obliquity is

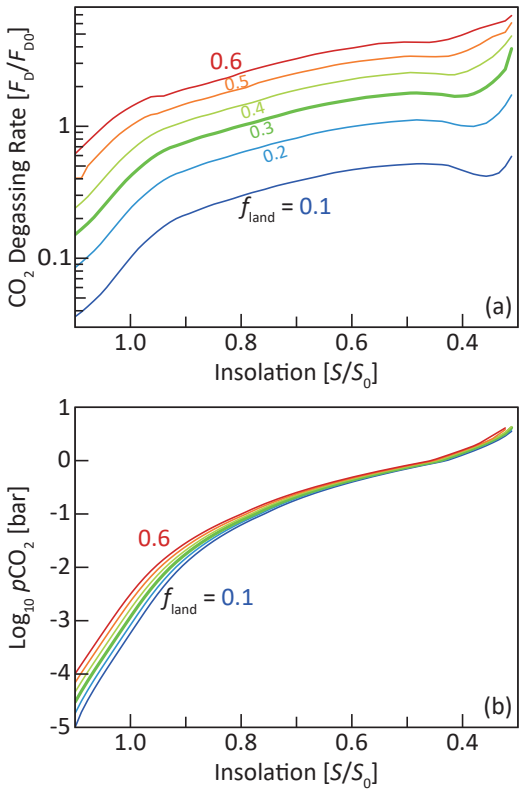

Figure 4.4: (a) The critical CO_2 degassing rate and (b) the critical pCO_2 as a function of the insolation for various land fractions (the present Earth corresponds to 0.3). The larger the land fraction is, the larger the critical CO_2 degassing rate is; however, the dependency of the critical CO_2 degassing rate on the land fraction may be overestimated because the runoff is assumed to be uniform in this model (see the text).

0. The black lines are calculated by the standard model, on the other hand, the red lines are calculated by the 1D-EBM without ice albedo feedback (the surface albedo is set to be constant at 0.4). When $p\mathrm{CO}_2$ is high ($\log_{10} p\mathrm{CO}_2 = -2$), the large ice-cap instability (unstable solutions in low latitudes) disappears without the ice albedo feedback (Figure 4.5a). However, when $p\mathrm{CO}_2$ is low ($\log_{10} p\mathrm{CO}_2 = -4.5$), while the large ice-cap instability also disappears without the ice albedo feedback, the small ice-cap unstable solutions remain even though the obliquity is zero and without the ice albedo feedback (the black line in Figure 4.5b). Hence, it is indicated that in addition to the ice albedo feedback, the other positive feedback mechanism works and results in the small ice-cap unstable solutions.

In order to discuss the feedback in the energy balance, the time-development of the surface temperature is considered. For simplicity, the obliquity is set to be zero, and the 1D-EBM (Equation 2.1) is integrated by latitude;

$$\frac{\partial}{\partial t}\int C\Delta T d\varphi = -\int \left\{\frac{S\cos\varphi}{\pi}\frac{\partial A}{\partial T} + \frac{\partial I}{\partial T}\right\}\Delta T\cos\varphi d\varphi, \tag{4.3}$$

where C is heat capacity. When a positive feedback works, the term, $S\cos\varphi/\pi \times \partial A/\partial T + \partial I/\partial T$ (hereafter, called as a "feedback factor"), must be negative at some latitudes. Equation 4.3 also suggests that the feedback at lower latitudes has more significant effect on the global balance of energy than at higher latitude because the cross-sectional area of low latitudes is larger than that of high latitudes. In addition, the larger the insolation is, the more significant the albedo-related feedback is because the net insolation is the product of the insolation and co-albedo (i.e., $1 - A$).

Figures 4.6a and 4.6b shows planetary radiation and a planetary albedo, respectively, as a function of the surface temperature for $\log_{10} p\mathrm{CO}_2 = -4.5$ and -2. Note that the surface albedo is set to be constant at 0.4 in order to exclude the ice albedo feedback. An increase in the surface temperature results in an increase in the planetary radiation. Higher $p\mathrm{CO}_2$ (i.e., $\log_{10} p\mathrm{CO}_2 = -2$) has more greenhouse effect and decreases the planetary radiation more than those for the lower $p\mathrm{CO}_2$ (i.e., $\log_{10} p\mathrm{CO}_2 = -4.5$; Figure 4.6a). Therefore, the saturation of planetary radiation occurs at higher surface temperature for higher $p\mathrm{CO}_2$ than that for lower $p\mathrm{CO}_2$ (Nakajima et al., 1992). In terms of the feedback factor, the relationship between the surface temperature and planetary radiation works

as a negative feedback (i.e., the planetary radiation increases with an increase in the surface temperature), but this effect weakens with an increase in the surface temperature, i.e., the increase in the planetary radiation becomes saturated in high surface temperatures (Figure 4.6a). On the other hand, the increase in the surface temperature results in a decrease in the planetary albedo (Figure 4.6b). This is because the increase in the surface temperature results in an increase in $p\mathrm{H_2O}$ (Note that $\mathrm{H_2O}$ is assumed to be saturated in the atmosphere), which results in an increase in the absorption of infrared radiation from the Sun in the upper atmosphere (Kasting, 1988; Kopparapu et al., 2013). In terms of the feedback factor, the relationship between the surface temperature and the planetary albedo works as a positive feedback (i.e., the planetary albedo decreases with an increase in the surface temperature, resulting in an increase in the net insolation), and this effect increases with an increase in the surface temperature owing to an exponential increase in saturated vapor pressure of $\mathrm{H_2O}$.

A combined relationship between the surface temperature and feedback factor is shown in Figure 4.6c. In Figure 4.6c, conditions are $S = S_0$, and $\varphi = 0°$. Generally speaking, the feedback factor decreases with an increase in the surface temperature. In other words, when the surface temperature is low, the feedback factor is larger than zero (i.e., a negative feedback works) owing to the steep gradient of the planetary radiation against the surface temperature, but the increase in the surface temperature results in a decrease in the feedback factor below zero (i.e., a positive feedback works) owing to the saturation of the planetary radiation and the increase in the absorption of infrared radiation from the Sun by $\mathrm{H_2O}$. The detail behavior, such as the inflection point around $T = 310\,\mathrm{K}$, depends strongly on the way of the fitting of the planetary radiation and albedo. Similarly, the local minimum around $T = 340\,\mathrm{K}$ the assumption for the fitting of the planetary albedo that the gradient of the planetary albedo is zero at 350 K (the maximum applicable range): this assumption is based on the characteristic feature that the planetary albedo has a local minimum around 350 K (e.g., Kasting, 1988).

An increase in the insolation results in a decrease in the feedback factor (Equation 4.3), therefore, this positive feedback tends to work under the high insolation condition. This is consistent with the result shown in Figure 3.2 in which the warm climate cycle mode exist only when the insolation is high. This positive feedback also tends to work at equatorial region where the surface temperature is relatively

high, hence the feedback has significant effect on the global balance of energy (see also Equation 4.3). Recall that the small ice-cap instability, which is pointed out before, is caused by the ice-albedo feedback at polar region which has less effect on the global balance of energy, and the small ice-cap instability is highly model dependent. Therefore, the small ice-cap unstable solutions caused by this positive feedback would be more robust behaviors than the small ice cap instability which is resulted from the ice albedo feedback at high latitude.

As a conclusion, the combined behavior of the planetary radiation and planetary albedo of the H_2O-rich atmosphere may act as positive feedback which results in a small ice-cap unstable solutions. And the small ice-cap unstable solutions would be more robust behaviors than the small ice-cap instability which is resulted from the ice albedo feedback at high latitude.

4.3 Neoproterozoic snowball Earth events

4.3.1 Probability of shift to snowball cycle mode

In Section 3.2, the evolutionary track of climate is explained: the luminosity increases monotonously while the CO_2 degassing rate decreases monotonously on timescale of ~1 Gyr (Figure 3.9). As a result, the Earth would remain in the warm climate mode for the first 5.2 Gyr (Figure 3.10). The CO_2 degassing rate is, however, supposed to fluctuate in a shorter timescale (~ 100 Myr) with fluctuations of the seafloor spreading rate fluctuates, as reconstructed for Phanerozoic (e.g., Gaffin, 1987; Cogne et al., 2006; Muller et al., 2008; Vérard et al., 2015). The fluctuations could be caused by Wilson cycle, which may be resulted from continental break-up and collision, and accompanied by fluctuation of the rate of volcanic CO_2 degassing. In addition, the break-up of supercontinent often begins with eruption of flood basalt caused by superplume rising from the core/mantle boundary (e.g., Yoshida and Santosh, 2011). Basalt is known for weathered much more easily than granite (e.g., Dessert et al., 2001, 2003), which results in increasing an efficiency of chemical weathering. The break-up of supercontinent Rodinia may, therefore, have caused the Neoproterozoic snowball Earth events, as combined with dispersed land-sea distribution due to the break-up of the supercontinent, which may have increased precipitation to land area for chemical

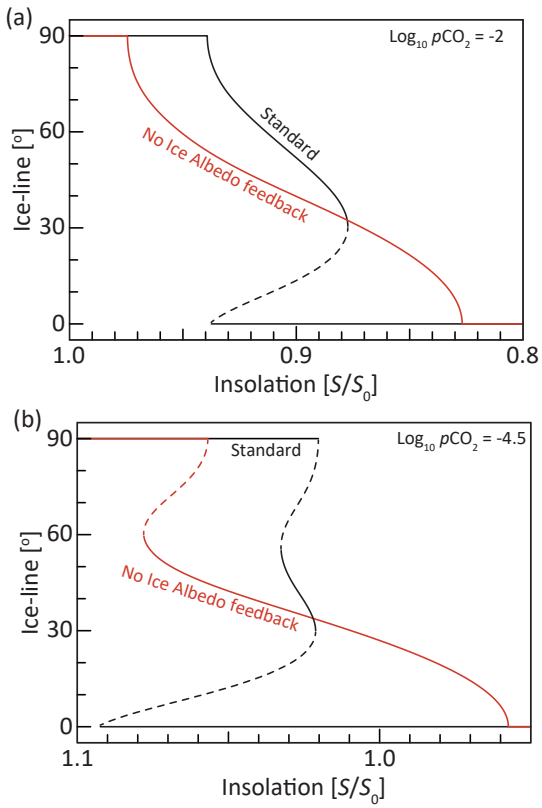

Figure 4.5: The ice-line as functions of insolation for $\log_{10} pCO_2 = -2$ (a) and -4.5 (b). The black lines are calculated by the standard model, and the red lines are calculated by the same model without ice albedo feedback. Note that the dashed lines represent unstable solutions. The small ice-cap unstable solution exist even if there is no ice albedo feedback for $\log_{10} pCO_2 = -4.5$.

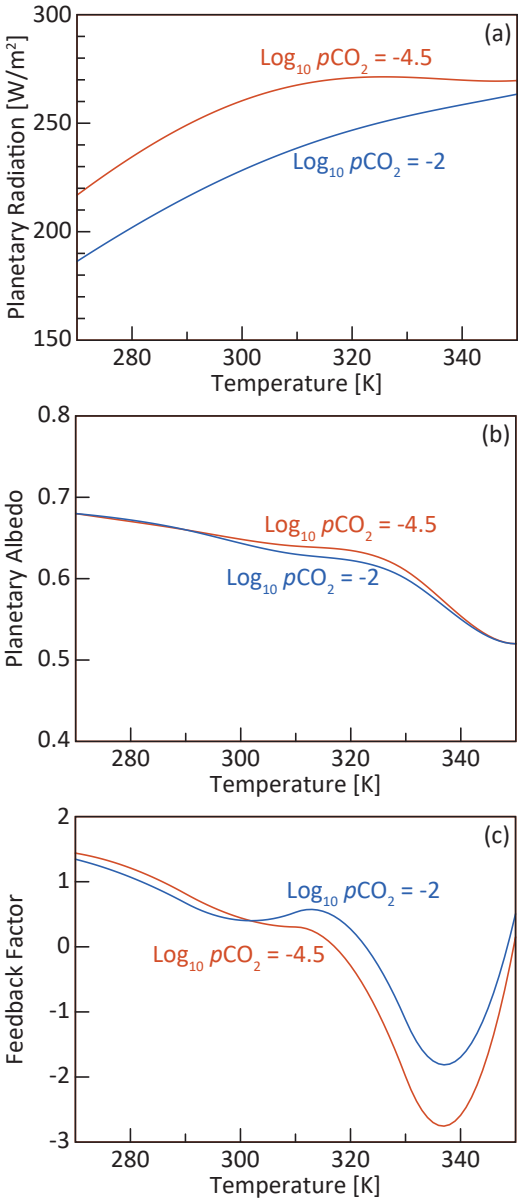

Figure 4.6: (a) Planetary radiation, (b) a planetary albedo, and (c) feedback factor as a function of the surface temperature. Insolation and latitude is assumed to be S_0 and 0°, respectively.

weathering of silicate minerals (Donnadieu et al., 2004a). Hence, such a short timescale fluctuation may result in climate change.

In order to evaluate the likelihood of the shift from the warm climate to snowball cycle modes, the CO_2 degassing rate is compared with the critical CO_2 degassing rate at each time. Here, a "snowball factor" is defined as the CO_2 degassing rate divided by the critical CO_2 degassing rate; the snowball factor for the Earth is shown in Figure 4.7. For example, the snowball factor for the present Earth is 4 (see the blue diamond in Figure 4.7), which means that the present Earth would shift to the snowball cycle mode if the CO_2 degassing rate decreases by a factor of 4 or if the efficiency of the CO_2 uptake rate increases by a factor of 4. For the first 4 Gyr, the snowball factor decreases with time (Figure 4.7). This is because the CO_2 degassing rate decreases with time (Figure 3.9) and also because the critical CO_2 degassing rate is relatively independent of time owing to weak dependency of the critical CO_2 degassing rate on the insolation when the insolation is low (Figure 3.2). On the other hand, after 4 Gyr to 5.2 Gyr, the snowball factor increases with time (Figure 4.7) although the CO_2 degassing rate still decreases with time (Figure 3.9): this is because the dependency of the critical CO_2 degassing rate on the insolation is strengthened when the insolation is high (Figure 3.2). Hence, the snowball factor becomes minimum at about 3.94 Gyr (i.e., ca 700 Ma). It corresponds roughly to the geological age when the two Neoproterozoic snowball Earth events occurred repeatedly within a very short period of time (717–660 Ma and 641–635 Ma, respectively) (e.g., Rooney et al., 2015). It is implied that the Neoproterozoic snowball Earth events could have been caused by the shift to the snowball cycle mode owing to the decrease in the CO_2 degassing rate and/or the increase in the weathering efficiency when the snowball factor was around its minimum.

4.3.2 Effect of continental growth

As discussed in Section 4.1.2, a difference in the continental size (i.e., the land fraction) may affects the critical CO_2 degassing rate. It is, therefore, important to include the continental growth to estimate the evolutionary track of the Earth's climate. In this section, the effect of continental growth is considered.

In order to discuss the effect of the continental growth, a "corrected CO_2

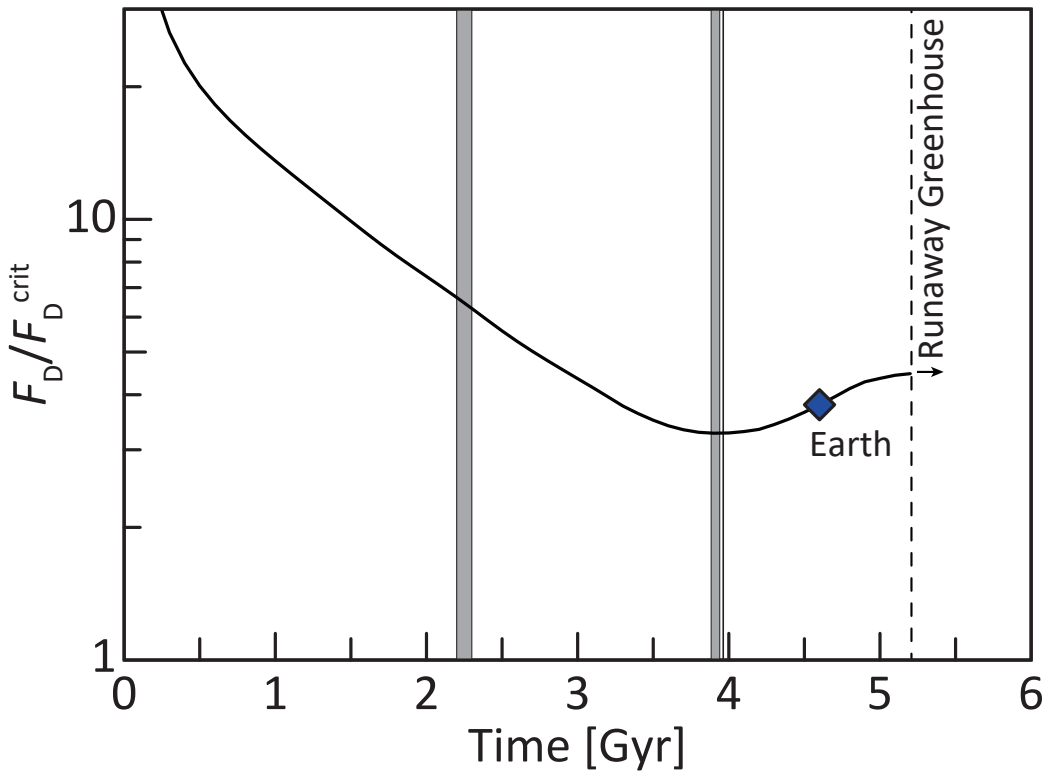

Figure 4.7: The CO_2 degassing rate divided by the critical CO_2 degassing rate at each time (called a "snowball factor") as a function of time. The blue diamond represents the present Earth's condition. The snowball factor reach a minimum at 3.9 Gyr (700 Ma from the present). The shaded regions represent the Makganyene (2.22 Ga), Sturtian (~ 717-660 Ma), and Marinoan (641-635 Ma) glaciations, respectively.

degassing rate", γ, is introduced. The CO_2 uptake rate depends on pCO_2, surface temperature (T), and a land fraction ($f_{\rm land} = 1 - f_{\rm o}$) (Equation 2.29), and the effect of the land fraction on the CO_2 uptake rate, $F_{\rm land}$, can be written as:

$$F_{\rm land}(f_{\rm land}) = \frac{W(p{\rm CO_2}, T; f_{\rm land})}{W(p{\rm CO_2}, T; 0.3)}. \tag{4.4}$$

$F_{\rm land}$, is derived from Figure 4.4a. In a steady state, the CO_2 degassing and uptake rates are balanced (i.e., $F_{\rm D} = W(p{\rm CO_2}, T; f_{\rm land}) = F_{\rm land}(f_{\rm land})W(p{\rm CO_2}, T; 0.3)$). Here, the corrected CO_2 degassing rate, γ, is defined as follows:

$$\gamma \equiv \frac{F_{\rm D}}{F_{\rm land}(f_{\rm land})}, \tag{4.5}$$

Because the case for $f_{\rm land} = 0$ cannot apply to this model, $f_{\rm land} > 0.01$ is assumed. Hence, the earliest history of the Earth may not be discussed in the following because continents might have been very small then.

During the Earth's history, the size of continents has increased with time. There are many studies on the continental growth and the many models have been proposed so far (e.g., Hurley and Rand, 1969; Fyfe, 1978; Brown, 1979; O'Nions et al., 1979; Veizer and Jansen, 1979; Armstrong and Harmon, 1981; Dewey and Windley, 1981; Allègre, 1982; McLennan and Taylor, 1982; Reymer and Schubert, 1984; McCulloch and Bennett, 1994; Condie, 1998; Rino et al., 2004, 2008; Iizuka et al., 2005). Figure 4.8 shows the recent models for the evolutions of the land fraction, which are based on the evolutions of the continental volume estimated from the age population of detrital zircons (Rino et al., 2004, 2008) and from the combination of U-Pb and Hf isotope systematics of the detrital zircons (Iizuka et al., 2005). Here, the land fraction is assumed to be proportional to the continental volume. In this study, the continental growth model proposed by Iizuka et al. (2005) is adopted because their method can reproduce the growth of the juvenile continental crust.

Figure 4.9 shows evolutionary tracks of the Earth on the climate diagram: note that the vertical axis is the corrected CO_2 degassing rate (γ) instead of the CO_2 degassing rate. The black line represents the evolutionary track the Earth's climate with the continental growth, and the white line represents the evolutionary track of the Earth's climate without the continental growth ($f_{\rm land} = 0.3$). For both

cases, $f_{\rm land}$ is set to be 0.3 after 4.6 Gyr. The corrected CO_2 degassing rate of the evolutionary track with the continental growth is larger than that without the continental growth before 4.6 Gyr. This is the case because the continental size is smaller than the present one before 4.6 Gyr. In that case, the efficiency of the CO_2 uptake is small, hence pCO_2 and surface temperature should be high in order to balance with the CO_2 degassing flux. Therefore, the continental growth contributes to the warm climate of the Earth in its early history. As shown in Figure 4.10, the snowball factor for the case with the continental growth (the black line line) has the same characteristic features as those for the case without the continental growth (the gray line): the snowball factor decreases with time for the first several Gyr, reaches a minimum around 4 Gyr, and, then, increases (Figure 4.10; see also Figure 4.7). The most important point is that the Earth is more likely to be in the warm climate mode when the continents were small and grow in its history for the first 4 Gyr (Figure 4.10).

4.3.3 Parameter study in thermal evolution model

In the standard thermal evolution model used in this study, the heat flow from the mantle is assumed to be proportional to the Rayleigh number to the power of one third (i.e., $\beta = 1/3$ in Equation 2.33). This is based on the laboratory experiments and theoretical analysis, and many studies adopted this classical relationship in the thermal evolution models (e.g., Schubert et al., 1980; Stevenson et al., 1983; McGovern and Schubert, 1989; Sandu et al., 2011). The present Urey ratio (a ration of a heat production to a heat flow from the mantle) is calculated to be 0.84 in this case, which is consistent with previous works (Schubert et al., 1980; Honda, 1995; Korenaga, 2006). However, this value is higher than the recent estimates from the observational data (0.2 to 0.49; Jaupart et al., 2015). Recent studies (e.g., Korenaga, 2010, 2006) suggest that lithosphere was stiffer in the past than that at present because relatively high mantle temperature in the past decreases H_2O content in the lithosphere. They also suggest that the mantle heat flow should be less dependent on the mantle temperature and smaller in the past than the traditional models with $\beta = 1/3$. Applying such assumptions, the present Urey ratio can be reproduced (Korenaga, 2011). In this section, the thermal evolution is re-estimated by the model with $\beta = 0$ in order to reveal the effect of these features

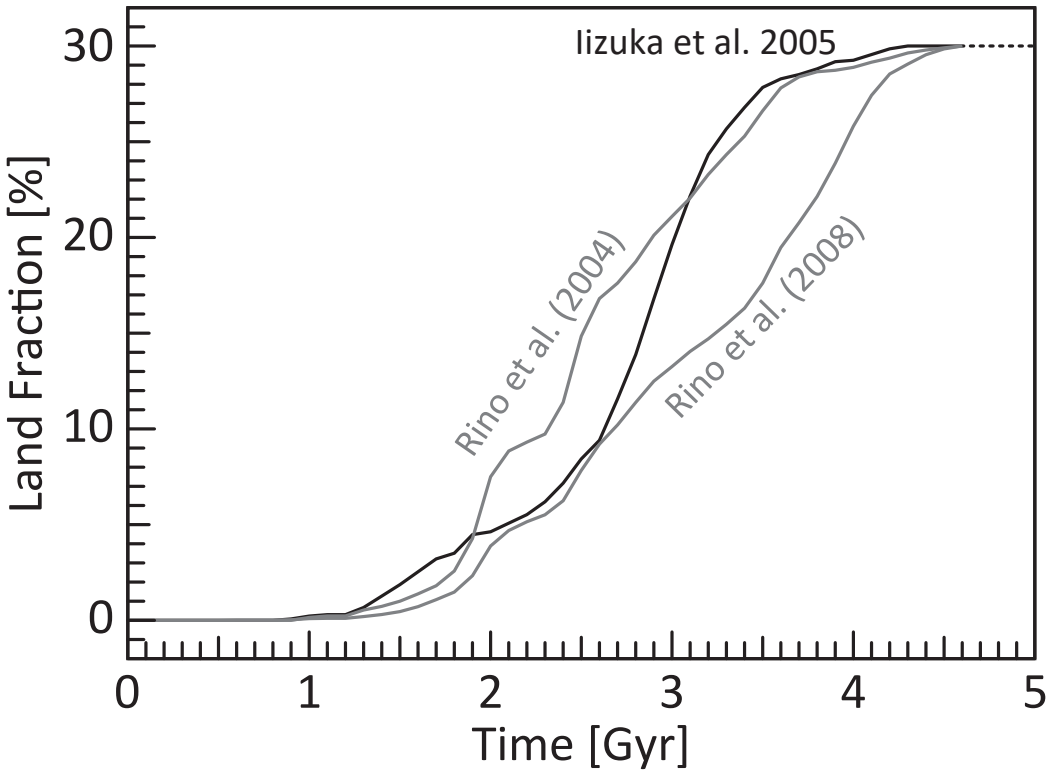

Figure 4.8: Evolution of land fraction based on recent studies of continental growth (Rino et al., 2004, 2008; Iizuka et al., 2005).

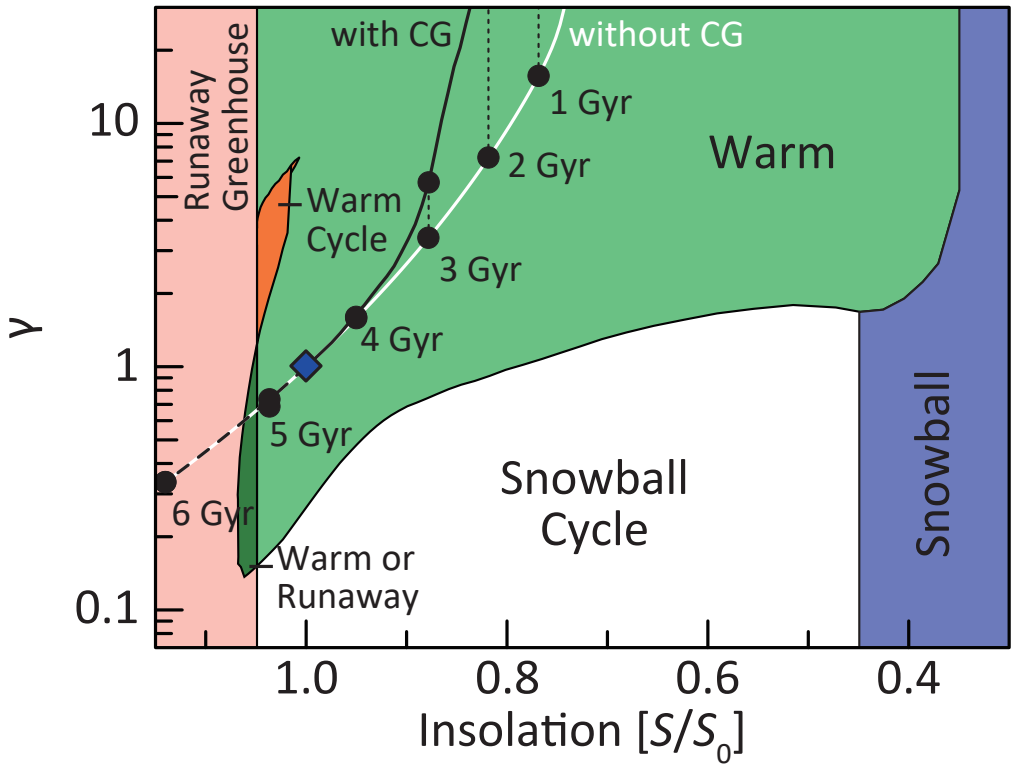

Figure 4.9: Evolutionary tracks of the climate of the Earth on the climate diagram. Vertical axis represents the corrected CO_2 degassing rate, γ. Black line represents the evolutionary track of the climate of the Earth with continental growth (CE). On the other hand, the white line represents the evolutionary track of the climate of the Earth without CE (the same as 1 AU case in Figure 3.10a).

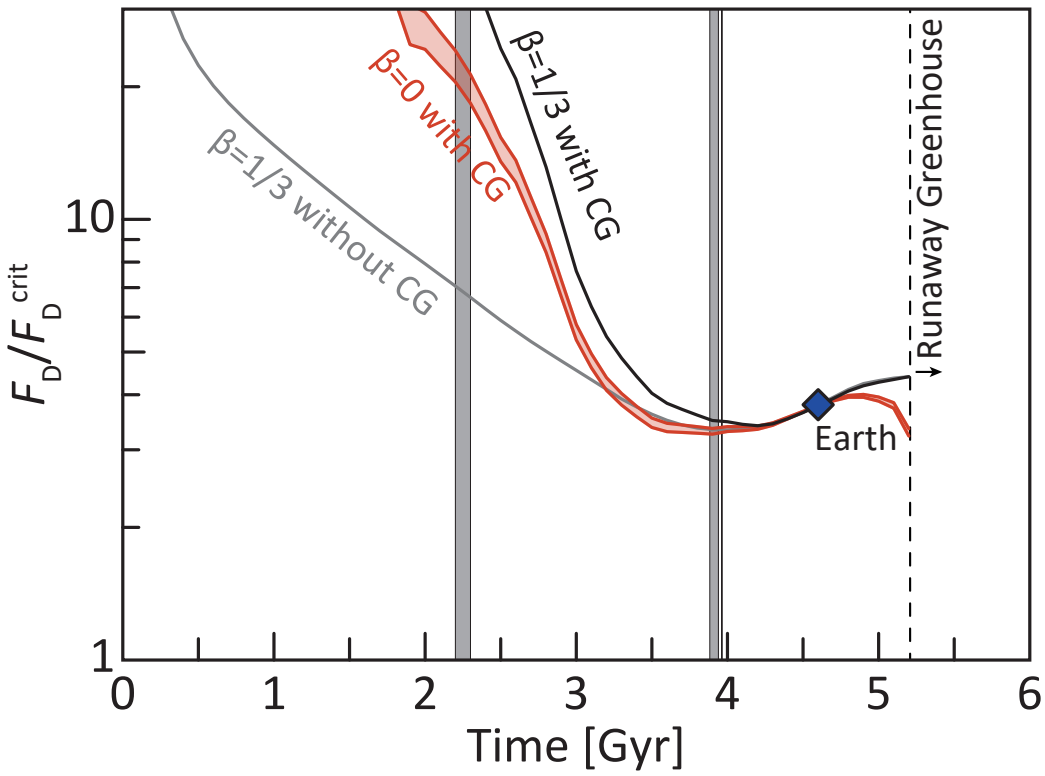

Figure 4.10: Snowball factors as functions of time (See also Figure 4.7). The gray line represents the standard case ($\beta = 1/3$ and without continental growth), the black line represents the case for $\beta = 1/3$ and with continental growth, and the red lines represent the case for $\beta = 0$ and with the continental growth. All cases show similar features: for the first several Gyr, the snowball factor decreases, then reaches its minimum around $t = 4$ Gyr.

on the climate evolution.

Figure 4.11 shows evolutions of average mantel temperature, heat flow from the mantle, heat production, and CO_2 degassing rate for the case with $\beta = 0$ and $1/3$. The initial mantle temperature is varied from 2400 K to 2700 K according to Korenaga (2011). The heat production rate is used as an adjustable parameters for both models, and the mantle viscosity and the thickness of the crust are also used as an adjustable parameters for the model with $\beta = 1/3$ and 0, respectively so that both models with $\beta = 0$ and $1/3$ may reproduce the observed heat flow and mantle temperature (hence, CO_2 degassing rate) at 4.6 Gyr (Figure 4.11). A difference of the average mantle temperature converges more rapidly for $\beta = 1/3$ than for $\beta = 0$ owing to the relatively high dependency of heat flow on the mantle temperature for $\beta = 1/3$ as pointed out in the previous work (e.g., Tajika and Matsui, 1993a).

As explained above, the adjustable parameters are determined so that the observed heat flow and mantle temperature are reproduced at 4.6 Gyr. When the mantle temperature is larger than the observed value, the heat flow for the case with $\beta = 0$ is less than that for the case with $\beta = 1/3$ owing to the relatively low dependency of heat flow on the mantle temperature for $\beta = 0$. In other words, when the mantle temperature is higher than the observed value (i.e., before 4.6 Gyr), the mantle temperature tends to decrease slower for the case with $\beta = 0$ than for the case with $\beta = 1/3$. Therefore, in order to reproduce the observe value of the mantle temperature, the heat production for the case with $\beta = 0$ is less than that for the case with $\beta = 1/3$ (Figure 4.11b). The heat production decreases with time owing to the exponential decrease in the radiogenic heat source (Figure 4.11b). When the heat flow from the mantle is less than the heat production, the mantle temperature increases till the heat flow becomes larger than the heat production (Figure 4.11a and b). Because the dependency of the heat flow from the mantle on the mantle temperature is less for $\beta = 0$ than for $\beta = 1/3$, the average mantle temperature for the case with $\beta = 0$ tends to be higher than that for the case with $\beta = 1/3$ for the first several Gyr.

On the other hand, when the mantle temperature is less than the observed value (i.e., after 4.6 Gyr), the heat flow from the mantle is larger for the case with $\beta = 0$ than for the case with $\beta = 1/3$ owing to the relatively low dependency of the heat flow from the mantle on the mantle temperature although the heat production for the case with $\beta = 0$ is less than that for the case with $\beta = 1/3$ (Figure 4.11b).

Therefore, the mantle temperature decreases faster for the case with $\beta = 0$ than for the case with $\beta = 1/3$ (Figure 4.11a).

The Urey ratio for $\beta = 0$ is in the range between 0.42 and 0.46, which is consistent is the observational data (Jaupart et al., 2015). As a result, the CO_2 degassing rate tends to decrease with time for both cases although it may increase for the first several Gyr owing to the initial increase in the mantle temperature. The CO_2 degassing rate for the case with $\beta = 0$ is less than that for the case with $\beta = 1/3$ (Figure 4.11c) because of the relatively low heat flow for $\beta = 0$ (Figure 4.11b). The fast decrease in the mantle temperature for the case with $\beta = 0$ results in the fast decrease in the CO_2 degassing rate. In addition, because, when the average mantle temperature is below a critical value ($\sim$ 1990 K), the melt is not produced in the mantle, the CO_2 degassing rate rapidly stops at around 6 Gyr (Figure 4.11c).

Even assuming $\beta = 0$, the Earth remains in the warm climate modes for the first 5.2 Gyr without the continental growth (black lines in Figure 4.12). Considering the continental growth, the corrected CO_2 degassing rate increases when the continent is small, therefore, the climate of the Earth is warmer before 4.6 Gyr than at 4.6 Gyr.

The snowball factor decreases for the first 3.9 Gyr, increases for the next 1 Gyr, and decrease again (red lines in Figure 4.10). In terms of the Earth's history, it can be said that the disturbance in the corrected CO_2 degassing rate made the Earth shifted to the snowball cycle mode, which occurred the most easily at 3.9 Gyr. It may correspond to the Neoproterozoic snowball Earth events (Figure 4.10).

4.3.4 Neoproterozoic snowball Earth events

The durations of the Neoproterozoic snowball Earth events are estimated based on $\delta^{13}C$ and Ir anomaly, and Re-Os and Ur-Pb dating (e.g., Hoffman et al., 1998; Bodiselitsch, 2005; Rooney et al., 2013, 2015; Prave et al., 2016). During the Sturtian glaciation, the snowball Earth events are supposed to last for 55 Myr to 59 Myr (e.g., Rooney et al., 2013, 2015), while it is supposed to last for 3 Myr to 15 Myr during the Marinoan glaciation (e.g., Hoffman et al., 1998; Bodiselitsch, 2005; Rooney et al., 2015; Prave et al., 2016).

According to these estimation of the snowball durations, and assuming a hard

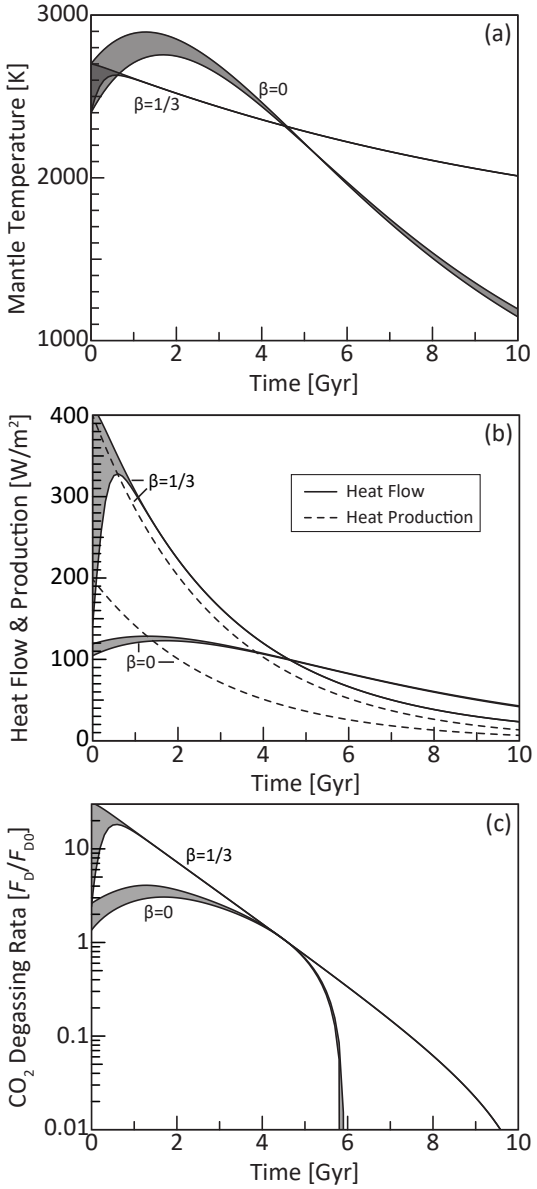

Figure 4.11: Evolution of (a) average mantle temperature, (b) heat flow from the mantle and heat production in unit of $\mathrm{W/m^2}$, and (c) CO_2 degassing rate for $\beta = 0$ and $1/3$. The initial average mantle is assumed from 2400 K to 2700 K (Korenaga, 2011).

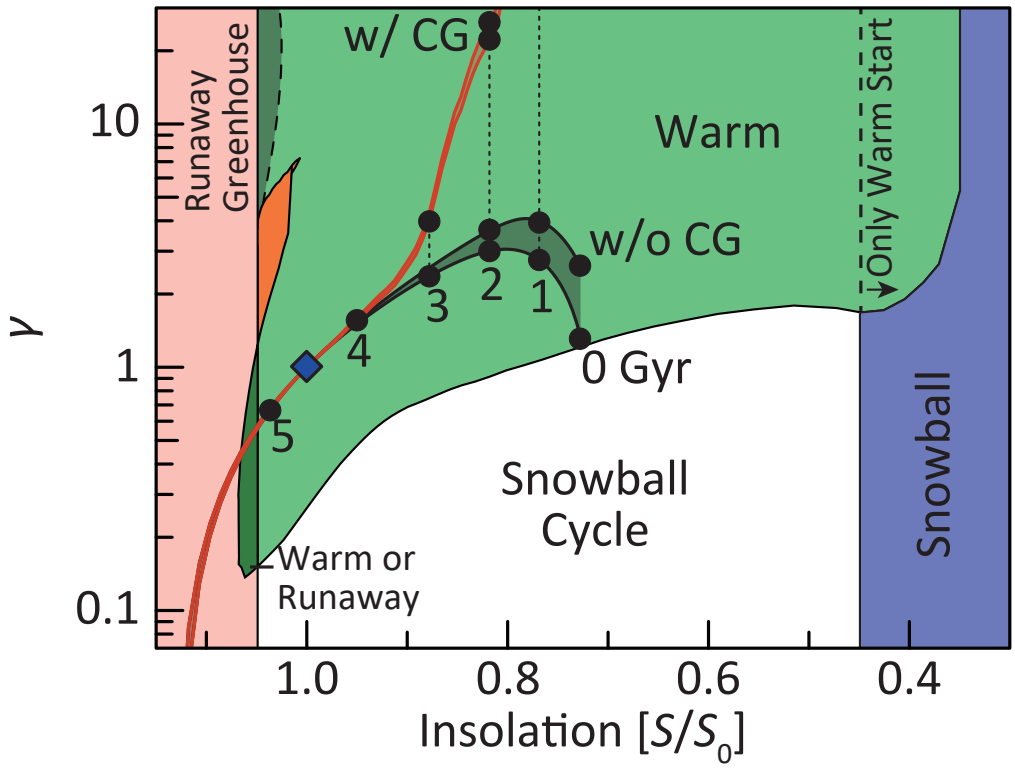

Figure 4.12: Evolutionary tracks on the climate diagram for $\beta = 0$. The black lines represent the evolutionary tracks without the continental growth, and the red lines represent the evolutionary tracks with the continental growth.

snowball Earth scenario (i.e., the case where the Earth is totally ice-covered without any open-water region), the average CO_2 degassing rates during these events can be estimated (see Figure 3.5a): the CO_2 degassing rate during the Sturtian glaciation is about 0.02 F_{D0}, and the rate during the Marinoan glaciation is 0.07 F_{D0} to 0.4 F_{D0}. These estimated CO_2 degassing rate is 80 times smaller for the Sturtian glaciation and 4 to 21 times smaller for the Marinoan glaciation than those estimated from the evolutionary track. Both correspond to the snowball cycle mode (Figure 4.13). If these estimates were correct, it might be consistent with the implication that the Neoproterozoic snowball Earth events could have been caused by the decrease in the CO_2 degassing rate.

A possibility for long snowball duration other than the decrease in the CO_2 degassing rate is a soft snowball Earth scenario (i.e., the case where there are open water regions locally while the Earth is globally ice-covered). According to Le Hir et al. (2008), if there are open water regions, atmospheric CO_2 dissolved into and acidifies oceans, which results in the promotion of the sea-floor weathering and delays the accumulation of atmospheric CO_2: for example, if there is thousands of square kilometer of open water region, it takes more than 30 Myr to build-up pCO_2 above the deglaciation threshold for the Neoproterozoic snowball states. Note that the effect of open water regions is negligible if the area of open water regions is lesser than ~ 10 km^2 (Le Hir et al., 2008).

The snowball duration of the Sturtian glaciation may correspond to that of the soft snowball case (Le Hir et al., 2008). In addition, the soft snowball case is consistent with the suggestion of Donnadieu et al. (2004a) which proposed that the continental break-up of Rodinia (e.g., Li et al., 2008) could have caused the Sturtian glaciation: this is because the superplume which broke Rodinia up may also have increased heat flow through the crust which may have produced local open water regions.

On the other hand, the snowball duration of the Marinoan glaciation is inconsistent with the soft snowball case. This is because, if the Marinoan glaciation is the soft snowball case, the CO_2 degassing rate should have been larger than 2 F_{D0} (20 % larger than that estimated in the evolutionary track) at least in order to account for the snowball duration, however, such a high CO_2 degassing rate is inconsistent with causing the snowball cycle mode.

Therefore, a scenario implied for the Neoproterozoic snowball Earth events

would be as follows. The supercontinent Rodinia started to break apart about 750 Ma (e.g., Li et al., 2008). The break-up of Rodinia changed climate over each continent, supplying much more precipitation, which increased CO_2 uptake via silicate weathering. Flood basalts, which may have triggered the break-up of Rodinia, could have also enhanced chemical weathering rate, resulting in the Sturtian snowball Earth event (Donnadieu et al., 2004a). Note that the increase in the CO_2 uptake rate corresponds to the decrease in γ in Figures 4.7 and 4.10. During the snowball state, the superplume which broke Rodinia increased heat flow through the crust, and the high heat flow melted the global ice-sheet locally, which delayed the deglaciation (Le Hir et al., 2008). Alternatively, the degassing rate of CO_2 may have been low, which delayed the deglaciation (Tajika, 2003, 2007). As a result, the Sturtian glaciation lasted for about 60 Myr (e.g., Rooney et al., 2015). The decrease in the CO_2 degassing rate (or γ) might have caused the Marinoan glaciation. For the Marinoan glaciation, the Earth was globally ice-covered without open water region. As a result, the Marinoan glaciation lasted for about 9 Myr, much shorter than the Sturtian glaciation (e.g., Rooney et al., 2015). Similar change in the CO_2 degassing and uptake rate due to the continental dispersion and reassembly may occur at other ages (e.g., the assembly and break-up of Gondwana), however, it is important to note here that the Neoproterozoic era is the most sensitive to the influence of such processes to cause snowball glaciations (Figure 4.7 and 4.10).

4.4 Hypothetical Earth around different type stars

It is expected that an Earth-like exoplanet will be discovered in the future. Such an Earth-like planet may be orbiting around stars different from the Sun, especially around a low mass star because the number of lower mass stars (i.e., M- and K-type stars) is much larger than that of higher mass stars (i.e., G- and F-type stars). According Research Consortium on Nearby Stars RECONS, there are 248 M-type stars, 44 K-type stars, 20 G-type stars and 6 F-type stars within 10 pc from the Sun. The difference in the stellar type yields the difference in the spectrum of the insolation as well as the timescale of the stellar evolution, which should affect the climate and the climate evolution of the hypothetical Earth around such stars. In this section, the climate and the climate evolution of hypothetical Earths around

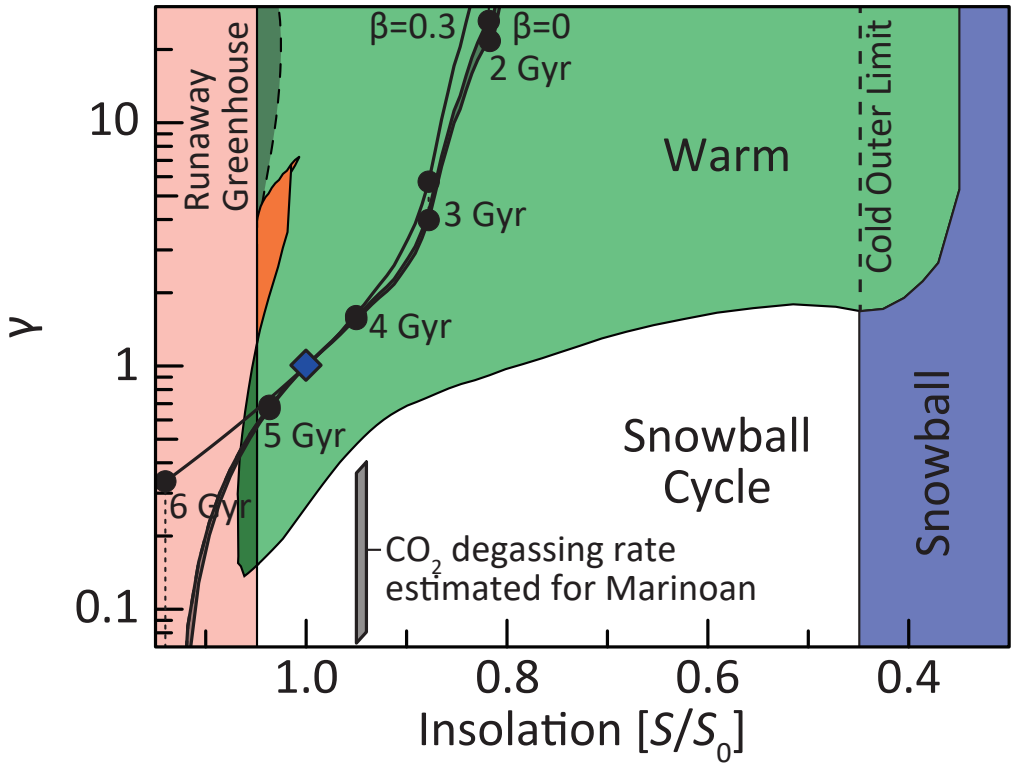

Figure 4.13: Evolutionary tracks for the cases where $\beta = 0$ and $1/3$ and the CO_2 degassing rate estimated for the Marinoan glaciation based on the snowball duration. Note that the CO_2 degassing rate for the Sturtian glaciation is smaller than the minimum limit of this diagram.

different type stars is discussed.

In the following, four types of stars (i.e., M-, K-, G-, and F-type stars) are considered. The effective temperature and mass of stars considered here are 3400 K and 0.5 $M_{\rm sun}$ for the M-type star, 4600 K and 0.8 $M_{\rm sun}$ for the K-type star, 5800 K and $M_{\rm sun}$ for the G-type star (i.e., the present Sun), and 7200 K and 1.4 $M_{\rm sun}$ for the F-type star. The planetary albedo which is affected by the spectral features of incident radiation are based on Kopparapu et al. (2013, 2014). The contribution of the visible light to the ice albedo is assumed to be 10 %, 32 %, 52 % and 67 % for M-, K-, G- and F- type star, respectively (Allard et al., 2007).

The luminosity evolutions of the stars are shown in Figure 4.14. As pointed out by the previous works (e.g., Iben, 1967), the larger stellar mass tends to result in higher luminosity. In addition, the larger stellar mass tends to have shorter timescale for the main sequence in the stellar evolution.

Figure 4.15 shows the climate mode of a hypothetical Earth as a function of insolation and CO_2 degassing rate. As pointed out by previous works (Kopparapu et al., 2013; Shields et al., 2013), the insolation is more absorbed by the planetary atmosphere for a relatively low mass star than for a relatively high mass stars because the peak wavelength of the insolation from the low mass star (i.e., the effective temperature is low) is longer than that from the high mass star (i.e., effective temperature is high), and the insolation from the low mass star is more absorbed by the planetary atmosphere and the ice surface than that from the high mass star; therefore the outer limits of the HZ for the low mass star (Figure 4.15a and b) is lower in terms of the insolation than those for the high mass star (Figure 4.15c and d). The difference between albedos for ice-covered and ice-free surface is smaller for the case of the low mass star than for the case of the high mass star (Allard et al., 2007; Shields et al., 2013). Therefore, the difference between the warm and cold outer limit of the HZ is located at lower incident flux for the low mass star than that for the high mass star (Figure 4.15).

The critical CO_2 degassing rate of the hypothetical Earth around the low mass star is also lower than that around the high mass star although the values are confined in the similar range in the outer region of the HZ for each type of star (Figure 4.15). As the ice albedo of the hypothetical Earth for the low mass star is lower than that for the high mass star, the planetary albedo of the hypothetical Earth under the critical condition of the warm climate tends to be lower around

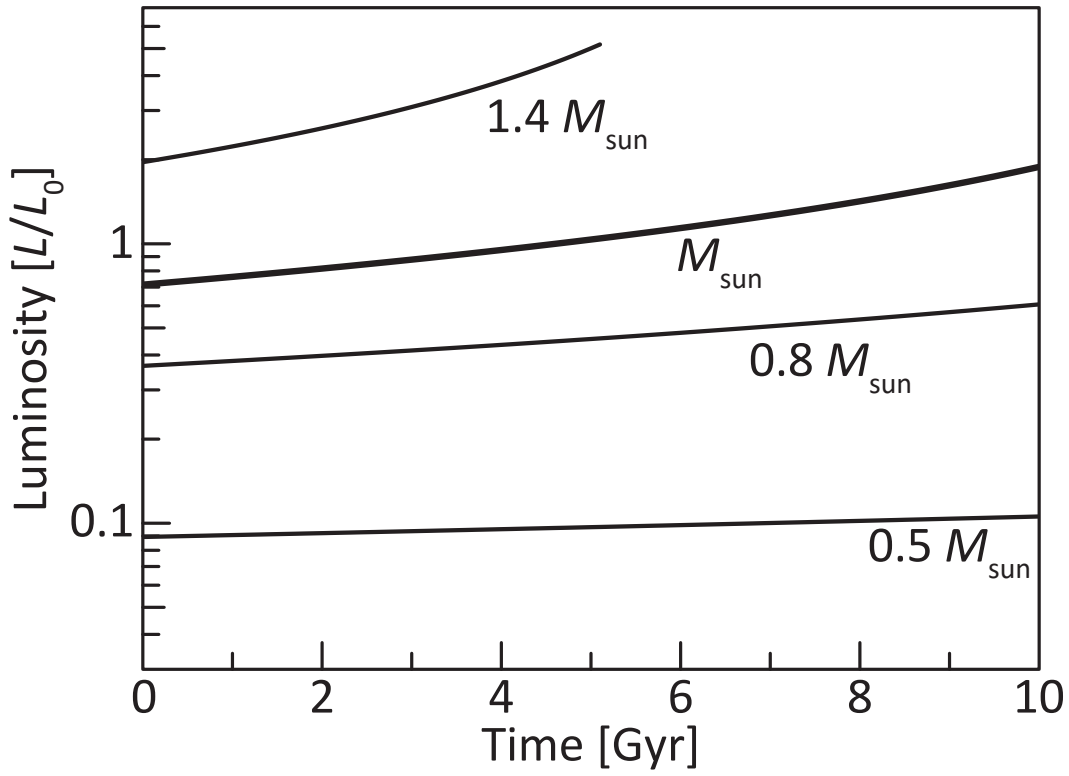

Figure 4.14: The relation between time and luminosity for stars with various mass. The luminosity is in the unit of the present solar luminosity of our Sun, L_0

the low mass star than around the high mass star, hence $p\mathrm{CO_2}$ of the hypothetical Earth around the low mass star tends to be lower than that of the planet around the high mass star if the insolation and the $\mathrm{CO_2}$ degassing rate are the same. Therefore, the critical $\mathrm{CO_2}$ uptake rate (= the critical $\mathrm{CO_2}$ degassing rate) tends to be lower if the planet is around the low mass star than around the high mass star. Because the critical ice-line tends to increase with a decrease in the insolation (see also Section 4.1), the increase in the critical ice-line (i.e., the decrease in the ice-covered region) results in the shrink of the effect of the difference in the ice albedo.

Figure 4.16 shows the climate evolution of the hypothetical Earth as a function of time and semi-major axis. The luminosity of a low mass star is smaller than that of a high temperature (e.g., Iben, 1967), therefore the inner limits of the HZ is closer to the central star for the low mass star than that for the high mass star (Figure 4.16) as suggested by previous works (e.g., Kasting et al., 1993; Kopparapu et al., 2013). In addition, the luminosity of the low mass star increases more slowly than that of the high mass star (e.g., Iben, 1967), the inner limits of the HZ moves outward more slowly for the low mass star than for the high mass star (Figure 4.16) as suggested by previous works (e.g., Kasting et al., 1993).

However, the climate of the hypothetical Earth in the HZ is dependent on the $\mathrm{CO_2}$ degassing rate in addition to the insolation, and the evolution of the $\mathrm{CO_2}$ degassing rate should depend on the thermal evolution of the planet itself, and is independent from the stellar evolution. Since the critical $\mathrm{CO_2}$ degassing rate is similar among these types of stars in the outer region of the HZ as explained above, the climate of the hypothetical Earth evolves from the warm climate mode to the snowball cycle mode on a similar timescale (about 4 Gyr in the outer region of the HZ; Figure 4.16). Although the timescale for which the hypothetical Earth is in the HZ is longer for the low mass star than for the high mass star (Kasting et al., 1993), the timescale for which the hypothetical Earth is actually in the warm climate mode would be limited by the planetary evolution and almost independent from the stellar type. After a certain age, the hypothetical Earth in the HZ is in the snowball cycle mode. In the snowball cycle mode, the hypothetical Earth is mainly, not in the warm climate state, but in the snowball state (Figure 3.5). Therefore, such a planet is likely to be observed as the snowball planet in the HZ.

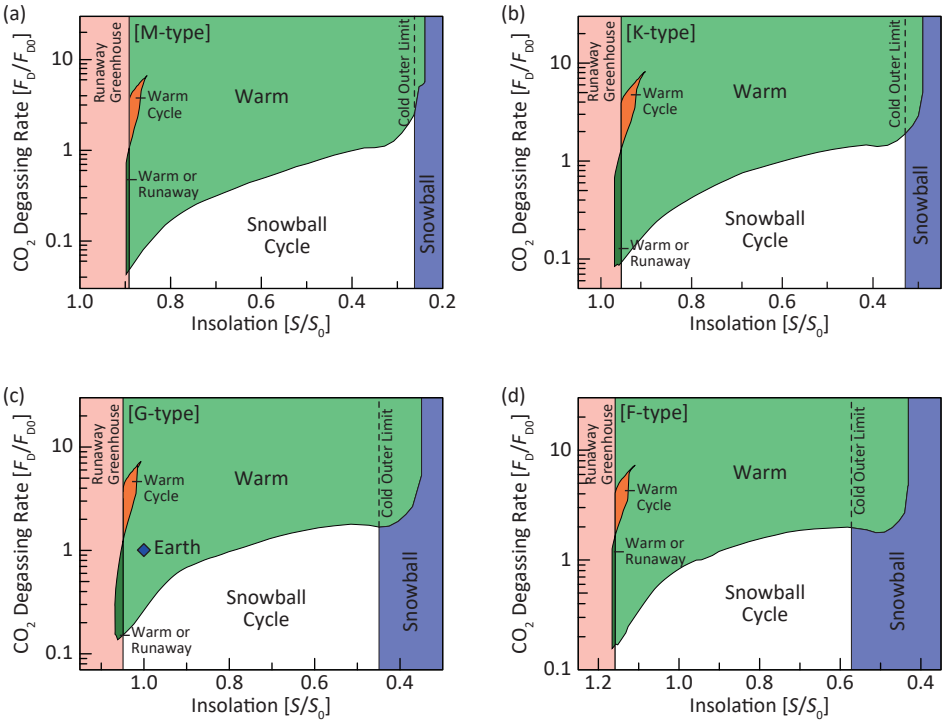

Figure 4.15: Climate diagrams for the hypothetical Earth around different type stars: (a) M-type star ($T_{\rm eff}$ = 3400 K), (b) K-type star ($T_{\rm eff}$ = 4600 K), (c) G-type star ($T_{\rm eff}$ = 5800 K) which is the same as Figure 3.2, (d) F-type star ($T_{\rm eff}$ = 7200 K).

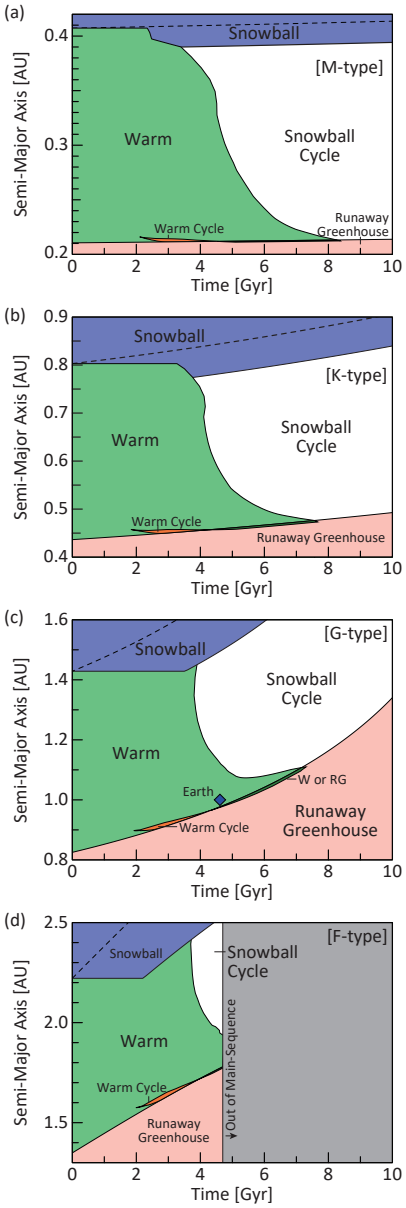

Figure 4.16: Evolution of climate mode for the hypothetical Earth around different type stars: (a) M-type star ($T_{\rm eff}$ = 3400 K and $M_{\rm s} = 0.5 M_{\rm sun}$), (b) K-type star ($T_{\rm eff}$ = 4600 K and $M_{\rm s} = 0.8 M_{\rm sun}$), (c) G-type star ($T_{\rm eff}$ = 5800 K and $M_{\rm s} = M_{\rm sun}$) which is the same as Figure 3.10b, (d) F-type star ($T_{\rm eff}$ = 7200 K and $M_{\rm s} = 1.4 M_{\rm sun}$).

4.5 Atmospheric dynamics and other uncertainties

In this study, 1D-EBM is used in order to estimate the surface temperature distribution of the Earth for a wide range of parameter space. However, the 1D-EBM does not consider the atmospheric dynamics and water cycle. Here, the influence of these factors are discussed.

As shown in Figure 2.3, the heat is transported poleward effectively in the equatorial region owing to the Hadley circulation, which is not reproduced by the 1D-EBM. As a result, the surface temperature in the equatorial region is supposed to be overestimated by the 1D-EBM. Considering the effective heat transport via the Hadley circulation, the expansion of the ice tends to be prevented as long as the sea ice tends to be out of the Hadley cell (Donnadieu et al., 2004b). However, when the sea ice reaches to the Hadley cell, the surface temperature in the equatorial region would decrease rapidly because the cool air on the sea ice is transported to the equatorial region by the Hadley circulation (Bendtsen, 2002; Donnadieu et al., 2004b).

In addition to the atmospheric circulation, clouds may affect the initiation of the global glaciation. A decrease in the surface temperature decreases clouds in the equatorial region, resulting in a decrease of planetary albedo. This mechanism works as a negative feedback which prevents the Earth from global glaciations (e.g., Hyde et al., 2000), although whether or not the decrease in the cloud indeed occurs depends largely on the cloud parameterization (Poulsen et al., 2001).

As a result, considering the atmospheric dynamics, the critical $p\mathrm{CO}_2$ below which the Earth is globally ice-covered is estimated to be 1×10^{-4}–2×10^{-3} bar for $S = 0.94S_0$ (e.g., Jenkins and Smith, 1999; Donnadieu et al., 2004b,a; Voigt et al., 2011; Liu et al., 2013, 2016). The values are similar to or somewhat low relative to the one estimated from 1D-EBM (2×10^{-3} bar), hence it may indicate that the critical $p\mathrm{CO}_2$ condition would be lower than that estimated with 1D-EBM in this study. However, even though the critical $p\mathrm{CO}_2$ is low ($\sim 2.5 \times 10^{-4}$ bar), global glaciations could occur under the same condition of the CO_2 degassing rate, if the continents are dispersed in the equatorial region and there is the region covered with flood basalts (Donnadieu et al., 2004a). This is because on the dispersed continents in the equatorial region, there are much precipitation compared to that on a supercontinent, and also because eruption of flood basalts enhances

weatherability (Donnadieu et al., 2004a). These effects are unable to be considered in the EBM.

In summarize, the critical condition estimated here may have uncertainties derived from model limitations and other factors which affects the critical condition. Thus, the quantitative results obtained in this study might be tentative. Studies using GCMs to verify the detailed behaviors of the climate system under the wide range of parameter space should be required in the future. Nonetheless, the basic concepts outlined in this study should provide a new framework for better understanding of the stability and evolution of the climate of the Earth, and, also, those of the Earth-like planets in the habitable zone of exoplanetary systems.

Section 5

Conclusions

The Earth has basically been warm sufficient to hold liquid water on the surface during the history, although the insolation from the Sun is supposed to have increased. This issue, the faint young Sun problem, is considered to be solved by the negative feedback (Walker feedback) mechanism due to the temperature-dependency of chemical weathering rate, which is the process of CO_2 consumption in the long-term carbonate-silicate geochemical cycle. However, the applicable limit for the Walker feedback mechanism has not been known so far. In order to reveal the condition under which the Walker feedback mechanism is able to warm the Earth, the climate of the Earth is estimated with a one-dimensional energy balance model coupled with a carbon cycle model against various insolation and CO_2 degassing rate, and the evolution of the climate is estimated with the stellar evolution model and the planetary thermal evolution model.

When a CO_2 degassing rate is high enough, the Earth in the habitable zone (HZ) can be in the warm climate mode which corresponds to the present Earth. However, when the CO_2 degassing rate is below a certain critical value, the Earth is either in the snowball climate mode or in the snowball cycle mode, even when the planet is orbiting within the HZ. The critical CO_2 degassing rate depends mainly on insolation and pCO_2 through the greenhouse effect of CO_2. There are two different outer limit of the HZ owing to the limit of the greenhouse effect of CO_2 and the ice-albedo feedback: one is the minimum insolation at which the climate of the Earth is able to be in the warm climate mode (the warm outer limit), and the another is the minimum insolation at which the climate of the Earth is able to

recover from the snowball state (the cold outer limit). The climate of the Earth has hysteresis between the warm and cold outer limits. In addition to the warm and snowball cycle modes, there may be a warm climate cycle mode where the Earth fluctuates between the partially ice-covered and no ice-sheet states. This climate mode is resulted from the small ice-cap unstable solution due to the dependencies of the planetary albedo and the planetary radiation on the surface temperature through the amount of water vapor in the atmosphere in addition to the ice-albedo feedback.

The climatic evolution of the Earth depends mainly on the evolution of the luminosity, and CO_2 degassing rate, and the continental growth. The Earth is supposed to have remained in the warm climate mode owing to the high CO_2 degassing rate and small continental size in the past. However, disturbance in CO_2 degassing rate may shift the Earth to the snowball cycle mode. The evolution of the snowball factor, which is the CO_2 degassing rate divided by the critical CO_2 degassing rate, suggests that the Earth is most susceptible to snowball glaciations at about 700 Ma (i.e., the Neoproterozoic era). This might be able to explain why two discrete snowball Earth events occurred repeatedly within 100 million years during the Neoproterozoic.

The hypothetical Earth in the outer HZ of extra-solar planetary systems may evolve in the warm climate mode for the first 4 Gyr, which is determined by the thermal evolution of the planetary interiors, and, then, evolves in the snowball cycle mode after 4 Gyr, which is independent from the stellar type. After 4 Gyr, the hypothetical Earth is in the snowball cycle mode and likely to be observed as the snowball planet.

References

F. Allard, N. F. Allard, D. Homeier, J. Kielkopf, M. J. McCaughrean, and F. Spiegelman. K–H_2 quasi-molecular absorption detected in the T-dwarf ϵ Indi Ba. *Astronomy and Astrophysics*, 474(2):L21–L24, 2007. doi: 10.1051/0004-6361:20078362.

C. J. Allègre. Chemical geodynamics. *Tectonophysics*, 81(3-4):109–132, 1982. doi: 10.1016/0040-1951(82)90125-1.

D. Ambrose. The vapour pressures and critical temperatures of acetylene and carbon dioxide. *Transactions of the Faraday Society*, 52:772–781, 1956. doi: 10.1039/TF9565200772.

R. L. Armstrong and R. S. Harmon. Radiogenic isotopes: The case for crustal recycling on a near-steady-state no-continental-growth earth [and discussion]. *Philosophical Transactions of the Royal Society A: Mathematical, Physical and Engineering Sciences*, 301(1461):443–472, 1981. doi: 10.1098/rsta.1981.0122.

J. Bendtsen. Climate sensitivity to changes in solar insolation in a simple coupled climate model. *Climate Dynamics*, 18(7):595–609, 2002. doi: 10.1007/s00382-001-0198-4.

R. A. Berner. A model for atmospheric CO_2 over Phanerozoic time. *American Journal of Science*, 291(4):339–376, 1991. doi: 10.2475/ajs.291.4.339.

R. A. Berner. GEOCARB II: A revised model of atmospheric CO_2 over Phanerozoic time. *American Journal of Science*, 294(1):56–91, 1994. doi: 10.2475/ajs.294.1.56.

R. A. Berner and Z. Kothavala. GEOCARB III: A revised model of atmospheric CO_2 over Phanerozoic time. *American Journal of Science*, 301(2):182–204, 2001. doi: 10.2475/ajs.301.2.182.

R. A. Berner, A. C. Lasaga, and R. M. Garrels. The carbonate-silicate geochemical cycle and its effect on atmospheric carbon dioxide over the past 100 million years. *American Journal of Science*, 283(7):641–683, 1983. doi: 10.2475/ajs.283.7.641.

B. Bodiselitsch. Estimating duration and intensity of neoproterozoic snowball glaciations from ir anomalies. *Science*, 308(5719):239–242, 2005. doi: 10.1126/science.1104657.

G. C. Brown. The changing pattern of batholith emplacement during earth history. In *Origin of Granite Batholiths*, pages 106–115. Springer Nature, 1979. doi: 10.1007/978-1-4684-0570-5_9.

R. F. Cahalan and G. R. North. A stability theorem for energy-balance climate models. *Journal of the Atmospheric Sciences*, 36(7):1178–1188, 1979. doi: 10.1175/1520-0469(1979)036<1178:ASTFEB>2.0.CO;2.

K. Caldeira and J. F. Kasting. Susceptibility of the early Earth to irreversible glaciation caused by carbon dioxide clouds. *Nature*, 359(6392):226–228, 1992. doi: 10.1038/359226a0.

U. R. Christensen. Thermal evolution models for the Earth. *Journal of Geophysical Research*, 90(B4):2995, 1985. doi: 10.1029/JB090iB04p02995.

J. Cogne, E. Humler, and V. Coutillot. Mean age of oceanic lithosphere drives eustatic sea-level change since Pangea breakup. *Earth and Planetary Science Letters*, 245(1-2):115–122, 2006. doi: 10.1016/j.epsl.2006.03.020.

K. C. Condie. Episodic continental growth and supercontinents: a mantle avalanche connection? *Earth and Planetary Science Letters*, 163(1-4):97–108, 1998. doi: 10.1016/s0012-821x(98)00178-2.

C. Dessert, B. Dupré, L. M. François, J. Schott, J. Gaillardet, G. Chakrapani, and S. Bajpai. Erosion of deccan traps determined by river geochemistry: impact on

the global climate and the 87sr/86sr ratio of seawater. *Earth and Planetary Science Letters*, 188(3-4):459–474, 2001. doi: 10.1016/S0012-821X(01)00317-X.

C. Dessert, B. Dupré, J. Gaillardet, L. M. François, and C. J. Allègre. Basalt weathering laws and the impact of basalt weathering on the global carbon cycle. *Chemical Geology*, 202(3-4):257–273, 2003. doi: 10.1016/j.chemgeo.2002.10.001.

J. F. Dewey and B. F. Windley. Growth and differentiation of the continental crust. *Philosophical Transactions of the Royal Society A: Mathematical, Physical and Engineering Sciences*, 301(1461):189–206, 1981. doi: 10.1098/rsta.1981.0105.

Y. Donnadieu, Y. Goddéris, G. Ramstein, A. Nédélec, and J. Meert. A 'snowball Earth' climate triggered by continental break-up through changes in runoff. *Nature*, 428(6980):303–306, 2004a. doi: 10.1038/nature02408.

Y. Donnadieu, G. Ramstein, F. Fluteau, D. Roche, and A. Ganopolski. The impact of atmospheric and oceanic heat transports on the sea-ice-albedo instability during the neoproterozoic. *Climate Dynamics*, 22(2-3):293–306, mar 2004b. doi: 10.1007/s00382-003-0378-5.

K. A. Eriksson. Sedimentation patterns in the Barberton mountain land, south Africa, and the Pilbara block, Australia: Evidence for Archean rifted continental margins. *Tectonophysics*, 81(3-4):179–193, 1982. doi: 10.1016/0040-1951(82)90128-7.

F. Forget and R. T. Pierrehumbert. Warming early Mars with carbon dioxide clouds that scatter infrared radiation. *Science*, 278(5341):1273–1276, 1997. doi: 10.1126/science.278.5341.1273.

W. S. Fyfe. The evolution of the earth's crust: Modern plate tectonics to ancient hot spot tectonics? *Chemical Geology*, 23(1-4):89–114, 1978. doi: 10.1016/0009-2541(78)90068-2.

S. Gaffin. Phase difference between sea level and magnetic reversal rate. *Nature*, 329(6142):816–819, 1987. doi: 10.1038/329816a0.

P. J. Gierasch and O. B. Toon. Atmospheric pressure variation and the climate of Mars. *Journal of the Atmospheric Sciences*, 30(8):1502–1508, 1973. doi: 10.1175/1520-0469(1973)030<1502:APVATC>2.0.CO;2.

D. O. Gough. Solar interior structure and luminosity variations. *Solar Physics*, 74 (1):21–34, 1981. doi: 10.1007/BF00151270.

R. M. Haberle, D. Tyler, C. P. McKay, and W. L. Davis. A model for the evolution of CO_2 on Mars. *Icarus*, 109(1):102–120, 1994. doi: 10.1006/icar.1994.1079.

J. Haqq-Misra, R. K. Kopparapu, N. E. Batalha, C. E. Harman, and J. F. Kasting. Limit cycles can reduce the width of the habitable zone. *The Astrophysical Journal*, 827:120, 2016. doi: 10.3847/0004-637X/827/2/120.

C. Herzberg, P. D. Asimow, N. Arndt, Y. Niu, C. M. Lesher, J. G. Fitton, M. J. Cheadle, and A. D. Saunders. Temperatures in ambient mantle and plumes: Constraints from basalts, picrites, and komatiites. *Geochemistry, Geophysics, Geosystems*, 8(2):Q02006, 2007. doi: 10.1029/2006GC001390.

M. M. Hirschmann. Mantle solidus: Experimental constraints and the effects of peridotite composition. *Geochemistry, Geophysics, Geosystems*, 1(10): 2000GC000070, 2000. doi: 10.1029/2000GC000070.

P. F. Hoffman and D. P. Schrag. The snowball Earth hypothesis: testing the limits of global change. *Terra Nova*, 14(3):129–155, 2002. doi: 10.1046/j.1365-3121.2002.00408.x.

P. F. Hoffman, A. J. Kaufman, G. P. Halverson, and D. P. Schrag. A Neoproterozoic snowball Earth. *Science*, 281(5381):1342–1346, 1998. doi: 10.1126/science.281.5381.1342.

S. Honda. A simple parameterized model of earth's thermal history with the transition from layered to whole mantle convection. *Earth and Planetary Science Letters*, 131:357–369, 1995. doi: 10.1016/0012-821X(95)00034-A.

J. R. Hurley, O. R. Pols, and C. A. Tout. Comprehensive analytic formulae for stellar evolution as a function of mass and metallicity. *Monthly Notices of the Royal Astronomical Society*, 315(3):543–569, 2000. doi: 10.1046/j.1365-8711.2000.03426.x.

P. M. Hurley and J. R. Rand. Pre-drift continental nuclei. *Science*, 164(3885): 1229–1242, 1969. doi: 10.1126/science.164.3885.1229.

W. T. Hyde, T. J. Crowley, S. K. Baum, and W. R. Peltier. Neoproterozoic 'snowball earth' simulations with a coupled climate/icesheet model. *Nature*, 405(6785): 425–429, 2000. doi: 10.1038/35013005.

I. Iben. Stellar evolution within and off the main sequence. *Annual Review of Astronomy and Astrophysics*, 5(1):571–626, 1967. doi: 10.1146/annurev.aa.05.090167.003035.

T. Iizuka, T. Hirata, T. Komiya, S. Rino, I. Katayama, A. Motoki, and S. Maruyama. U-Pb and Lu-Hf isotope systematics of zircons from the Mississippi river sand: Implications for reworking and growth of continental crust. *Geology*, 33(6): 485, 2005. doi: 10.1130/g21427.1.

H. Jacobowitz, W. L. Smith, H. B. Howell, F. W. Nagle, and J. R. Hickey. The first 18 months of planetary radiation budget measurements from the nimbus 6 ERB experiment. *Journal of the Atmospheric Sciences*, 36(3):501–507, 1979. doi: 10.1175/1520-0469(1979)036<0501:TFMOPR>2.0.CO;2.

C. Jaupart, S. Labrosse, F. Lucazeau, and J.-C. Mareschal. *Temperatures, Heat, and Energy in the Mantle of the Earth*, volume 7, chapter 7.06, pages 223–270. Elsevier BV, 2015. doi: 10.1016/B978-0-444-53802-4.00126-3.

G. S. Jenkins and S. R. Smith. GCM simulations of snowball earth conditions during the late proterozoic. *Geophysical Research Letters*, 26(15):2263–2266, aug 1999. doi: 10.1029/1999GL900538.

E. Kalnay, M. Kanamitsu, R. Kistler, W. Collins, D. Deaven, L. Gandin, M. Iredell, S. Saha, G. White, J. Woollen, Y. Zhu, A. Leetmaa, R. Reynolds, M. Chelliah, W. Ebisuzaki, W. Higgins, J. Janowiak, K. C. Mo, C. Ropelewski, J. Wang, R. Jenne, and D. Joseph. The NCEP/NCAR 40-year reanalysis project. *Bulletin of the American Meteorological Society*, 77(3):437–471, 1996. doi: 10.1175/1520-0477(1996)077<0437:TNYRP>2.0.CO;2.

J. F. Kasting. Runaway and moist greenhouse atmospheres and the evolution of Earth and venus. *Icarus*, 74(3):472–494, 1988. doi: 10.1016/0019-1035(88)90116-9.

J. F. Kasting, D. P. Whitmire, and R. T. Reynolds. Habitable zones around main sequence stars. *Icarus*, 101(1):108–128, 1993. doi: 10.1006/icar.1993.1010.

J. F. Kasting, A. Pavlov, and J. L. Siefert. A coupled ecosystem-climate model for predicting the methane concentration in the Archean atmosphere. *Origins of Life and Evolution of the Biosphere*, 31(3):271–285, 2001. doi: 10.1023/A:1010600401718.

J. L. Kirschvink. *The Proterozoic Biosphere: Multidisciplinary Study*, chapter Late Proterozoic Low-Latitude Global Glaciation: the snowball Earth, pages 51–52. Cambridge University Press, 1992.

J. L. Kirschvink, E. J. Gaidos, L. E. Bertani, N. J. Beukes, J. Gutzmer, L. N. Maepa, and B. Steinberger. Paleoproterozoic snowball Earth: Extreme climatic and geochemical global change and its biological consequences. *Proceedings of the National Academy of Sciences*, 97(4):1400–1405, 2000. doi: 10.1073/pnas.97.4.1400.

K. Y. A. Kondrat'ev. *Radiation in the Atmosphere*, chapter Albedo of the underlying surface and clouds, pages 411–452. Academic Press, 1969.

R. E. Kopp, J. L. Kirschvink, I. A. Hilburn, and C. Z. Nash. The paleoproterozoic snowball Earth: A climate disaster triggered by the evolution of oxygenic photosynthesis. *Proceedings of the National Academy of Sciences*, 102(32):11131–11136, 2005. doi: 10.1073/pnas.0504878102.

R. K. Kopparapu, R. Ramirez, J. F. Kasting, V. Eymet, T. D. Robinson, S. Mahadevan, R. C. Terrien, S. Domagal-Goldman, V. Meadows, and R. Deshpande. Habitable zones around main-sequence stars: new estimates. *The Astrophysical Journal*, 765(2):131, 2013. doi: 10.1088/0004-637X/765/2/131.

R. K. Kopparapu, R. M. Ramirez, J. SchottelKotte, J. F. Kasting, S. Domagal-Goldman, and V. Eymet. Habitable zones around main-sequence stars: depen-

dence on planetary mass. *The Astrophysical Journal Letters*, 787(2):L29, 2014. doi: 10.1088/2041-8205/787/2/L29.

J. Korenaga. *Archean Geodynamics and Environments*, chapter Archean geodynamics and the thermal evolution of Earth, pages 7–32. Wiley-Blackwell, 2006. doi: 10.1029/164GM03.

J. Korenaga. Urey ratio and the structure and evolution of earth's mantle. *Reviews of Geophysics*, 46(2), jun 2008. doi: 10.1029/2007RG000241.

J. Korenaga. Scaling of plate tectonic convection with pseudoplastic rheology. *Journal of Geophysical Research*, 115(B11):B11405, 2010. doi: 10.1029/2010JB007670.

J. Korenaga. Thermal evolution with a hydrating mantle and the initiation of plate tectonics in the early Earth. *Journal of Geophysical Research*, 116(B12): B12403, 2011. doi: 10.1029/2011JB008410.

L. R. Kump, S. L. Brantley, and M. A. Arthur. Chemical weathering, atmospheric CO_2, and climate. *Annual Review of Earth and Planetary Sciences*, 28(1): 611–667, 2000. doi: 10.1146/annurev.earth.28.1.611.

G. Le Hir, G. Ramstein, Y. Donnadieu, and Y. Goddéris. Scenario for the evolution of atmospheric pCO_2 during a snowball Earth. *Geology*, 36(1):47, 2008. doi: 10.1130/G24124A.1.

Z. X. Li, S. V. Bogdanova, A. S. Collins, A. Davidson, B. De Waele, R. E. Ernst, I. C. W. Fitzsimons, R. A. Fuck, D. P. Gladkochub, J. Jacobs, K. E. Karlstrom, S. Lu, L. M. Natapov, V. Pease, S. A. Pisarevsky, K. Thrane, and V. Vernikovsky. Assembly, configuration, and break-up history of Rodinia: A synthesis. *Precambrian Research*, 160(1-2):179–210, 2008. doi: 10.1016/j.precamres.2007.04.021.

K. N. Liou. *An introduction to atmospheric radiation*. Academic press, 2nd. edition, 2002.

Y. Liu, W. R. Peltier, J. Yang, and G. Vettoretti. The initiationof Neoproterozoic "snowball" climate in CCSM3: the influence of paleocontinental configuration. *Climate of the Past*, 9:2555–2577, 2013. doi: 10.5194/cp-9-2555-2013.

Y. Liu, W. R. Peltier, J. Yang, G. Vettoretti, and J. Wang. Strong effects of tropical ice-sheet coverage and thickness on the hard snowball Earth bifurcation point. *Climate Dynamics*, jul 2016. doi: 10.1007/s00382-016-3278-1.

H. G. Marshall, J. C. G. Walker, and W. R. Kuhn. Long-term climate change and the geochemical cycle of carbon. *Journal of Geophysical Research: Atmospheres*, 93(D1):791–801, 1988. doi: 10.1029/JD093iD01p00791.

M. T. McCulloch and V. C. Bennett. Progressive growth of the earth's continental crust and depleted mantle: Geochemical constraints. *Geochimica et Cosmochimica Acta*, 58(21):4717–4738, 1994. doi: 10.1016/0016-7037(94)90203-8.

P. J. McGovern and G. Schubert. Thermal evolution of the Earth: effects of volatile exchange between atmosphere and interior. *Earth and Planetary Science Letters*, 96(1-2):27–37, 1989. doi: 10.1016/0012-821x(89)90121-0.

S. M. McLennan and S. R. Taylor. Geochemical constraints on the growth of the continental crust. *The Journal of Geology*, 90(4):347–361, 1982. doi: 10.1086/628690.

K. Menou. Climate stability of habitable Earth-like planets. *Earth and Planetary Science Letters*, 429:20–24, 2015. doi: 10.1016/j.epsl.2015.07.046.

M. Mischna, J. F. Kasting, A. Pavlov, and R. Freedman. Influence of carbon dioxide clouds on early martian climate. *Icarus*, 145(2):546–554, 2000. doi: 10.1006/icar.2000.6380.

S. J. Mojzsis, T. M. Harrison, and R. T. Pidgeon. Oxygen-isotope evidence from ancient zircons for liquid water at the Earth's surface 4300 Myr ago. *Nature*, 409(6817):178–181, 2001. doi: 10.1038/35051557.

R. D. Muller, M. Sdrolias, C. Gaina, B. Steinberger, and C. Heine. Long-term sea-level fluctuations driven by ocean basin dynamics. *Science*, 319(5868):1357–1362, 2008. doi: 10.1126/science.1151540.

S. Nakajima, Y.-Y. Hayashi, and Y. Abe. A study on the "runaway greenhouse effect" with a one-dimensional radiative–convective equilibrium model. *Jour-*

nal of the Atmospheric Sciences, 49(23):2256–2266, 1992. doi: 10.1175/1520-0469(1992)049<2256:ASOTGE>2.0.CO;2.

T. Nakamura and E. Tajika. Stability and evolution of the climate system of Mars. *Earth, Planets and Space*, 53(8):851–859, 2001. doi: 10.1186/BF03351682.

G. R. North. Analytical solution to a simple climate model with diffusive heat transport. *Journal of the Atmospheric Sciences*, 32(7):1301–1307, 1975. doi: 10.1175/1520-0469(1975)032<1301:ASTASC>2.0.CO;2.

G. R. North. The small ice cap instability in diffusive climate models. *Journal of the Atmospheric Sciences*, 41(23):3390–3395, 1984. doi: 10.1175/1520-0469(1984)041<3390:TSICII>2.0.CO;2.

G. R. North, R. F. Cahalan, and J. A. Coakley, Jr. Energy balance climate models. *Reviews of Geophysics and Space Physics*, 19(1):91–121, 1981. doi: 10.1029/RG019i001p00091.

A. P. Nutman, J. H. Allaart, D. Bridgwater, E. Dimroth, and M. Rosing. Stratigraphic and geochemical evidence for the depositional environment of the early archaean isua supracrustal belt, southern west greenland. *Precambrian Research*, 25(4):365–396, 1984. doi: 10.1016/0301-9268(84)90010-X.

R. K. O'Nions, N. M. Evensen, and P. J. Hamilton. Geochemical modeling of mantle differentiation and crustal growth. *Journal of Geophysical Research*, 84 (B11):6091, 1979. doi: 10.1029/jb084ib11p06091.

A. A. Pavlov, M. T. Hurtgen, J. F. Kasting, and M. A. Arthur. Methane-rich Proterozoic atmosphere? *Geology*, 31(1):87, 2003. doi: 10.1130/0091-7613(2003)031<0087:MRPA>2.0.CO;2.

D. Pollard and J. F. Kasting. Snowball Earth: A thin-ice solution with flowing sea glaciers. *Journal of Geophysical Research*, 110(C7):C07010, 2005. doi: 10.1029/2004JC002525.

O. R. Pols, K-P Schröder, J. R. Hurley, C. A. Tout, and P. P. Eggleton. Stellar evolution models for Z = 0.0001 to 0.03. *Monthly Notices of the Royal Astronomical Society*, 298(2):525–536, 1998. doi: 10.1046/j.1365-8711.1998.01658.x.

C. J. Poulsen, R. T. Pierrehumbert, and R. L. Jacob. Impact of ocean dynamics on the simulation of the neoproterozoic "snowball earth". *Geophysical Research Letters*, 28(8):1575–1578, 2001. doi: 10.1029/2000GL012058.

A. R. Prave, D. J. Condon, K. H. Hoffmann, S. Tapster, and A. E. Fallick. Duration and nature of the end-cryogenian (Marinoan) glaciation. *Geology*, 44(8):631–634, 2016. doi: 10.1130/G38089.1.

N. A. Rayner, D. E. Parker, E. B. Horton, C. K. Folland, L. V. Alexander, E. C. Rowell, D. P.and Kent, and A. Kaplan. Global analyses of sea surface temperature, sea ice, and night marine air temperature since the late nineteenth century. *Journal of Geophysical Research*, 108(D14):4407, 2003. doi: 10.1029/2002JD002670.

RECONS. URL `http://www.recons.org/`. Accessed: 2016-12-07.

A. Reymer and G. Schubert. Phanerozoic addition rates to the continental crust and crustal growth. *Tectonics*, 3(1):63–77, 1984. doi: 10.1029/tc003i001p00063.

F. M. Richter and D. P. McKenzie. On some consequences and possible causes of layered mantle convection. *Journal of Geophysical Research: Solid Earth*, 86 (B7):6133–6142, 1981. doi: 10.1029/JB086iB07p06133.

S. Rino, T. Komiya, B. F. Windley, I. Katayama, A. Motoki, and T. Hirata. Major episodic increases of continental crustal growth determined from zircon ages of river sands: implications for mantle overturns in the early Precambrian. *Physics of the Earth and Planetary Interiors*, 146(1-2):369–394, 2004. doi: 10.1016/j.pepi.2003.09.024.

S. Rino, Y. Kon, W. Sato, S. Maruyama, M. Santosh, and D. Zhao. The Grenvillian and pan-African orogens: World's largest orogenies through geologic time, and their implications on the origin of superplume. *Gondwana Research*, 14(1-2): 51–72, 2008. doi: 10.1016/j.gr.2008.01.001.

A. D. Rooney, F. A. Macdonald, J. V. Strauss, F. O. Dudas, C. Hallmann, and D. Selby. Re-Os geochronology and coupled Os-Sr isotope constraints on the sturtian snowball earth. *Proceedings of the National Academy of Sciences*, 111 (1):51–56, 2013. doi: 10.1073/pnas.1317266110.

A. D. Rooney, J. V. Strauss, A. D. Brandon, and F. A. Macdonald. A cryogenian chronology: Two long-lasting synchronous neoproterozoic glaciations. *Geology*, 43(5):459–462, 2015. doi: 10.1130/G36511.1.

C. Sagan and G. Mullen. Earth and Mars: Evolution of atmospheres and surface temperatures. *Science*, 177(4043):52–56, 1972. doi: 10.1126/science.177.4043.52.

C. Sandu, A. Lenardic, and P. McGovern. The effects of deep water cycling on planetary thermal evolution. *Journal of Geophysical Research*, 116(B12):404, 2011. doi: 10.1029/2011jb008405.

L. Schaefer and D. Sasselov. The persistence of oceans on Earth-like planets: insights from the deep-water cycle. *The Astrophysical Journal*, 801(1):40, 2015. doi: 10.1088/0004-637x/801/1/40.

D. P. Schrag, R. A. Berner, P. F. Hoffman, and G. P. Halverson. On the initiation of a snowball Earth. *Geochemistry, Geophysics, Geosystems*, 3(6):1–21, 2002. doi: 10.1029/2001GC000219.

G. Schubert and T. Spohn. Two-layer mantle convection and the depletion of radioactive elements in the lower mantle. *Geophysical Research Letters*, 8(9): 951–954, 1981. doi: 10.1029/GL008i009p00951.

G. Schubert, P. Cassen, and R. E. Young. Subsolidus convective cooling histories of terrestrial planets. *Icarus*, 38(2):192–211, 1979. doi: 10.1016/0019-1035(79)90178-7.

G. Schubert, D. Stevenson, and P. Cassen. Whole planet cooling and the radiogenic heat source contents of the Earth and Moon. *Journal of Geophysical Research: Solid Earth*, 85(B5):2531–2538, 1980. doi: 10.1029/JB085iB05p02531.

D. W. Schwartzman and T. Volk. Biotic enhancement of weathering and the habitability of Earth. *Nature*, 340(6233):457–460, 1989. doi: 10.1038/340457a0.

D. W. Schwartzman and T. Volk. Biotic enhancement of weathering and surface temperatures on earth since the origin of life. *Palaeogeography, Palaeoclimatology, Palaeoecology*, 90(4):357–371, 1991. doi: 10.1016/S0031-0182(12)80035-6.

A. L. Shields, V. S. Meadows, C. M. Bitz, R. T. Pierrehumbert, M. M. Joshi, and T. D. Robinson. The effect of host star spectral energy distribution and ice-albedo feedback on the climate of extrasolar planets. *Astrobiology*, 13(8): 715–739, 2013. doi: 10.1089/ast.2012.0961.

N. H. Sleep. Thermal history and degassing of the Earth: Some simple calculations. *The Journal of Geology*, 87(6):671–686, 1979. doi: 10.1086/628459.

D. Stevenson, T. Spohn, and G. Schubert. Magnetism and thermal evolution of the terrestrial planets. *Icarus*, 54(3):466–489, 1983. doi: 10.1016/0019-1035(83) 90241-5.

E. Tajika. *Evolution of the Atmosphere and Ocean of the Earth: Global Geochemical Cycles of C, H , O , N, and S, and Degassing History Coupled with Thermal History*. phdthesis, The University of Tokyo, 1992.

E. Tajika. Faint young Sun and the carbon cycle: implication for the Proterozoic global glaciations. *Earth and Planetary Science Letters*, 214:443–453, 2003. doi: 10.1016/S0012-821X(03)00396-0.

E. Tajika. Long-term stability of climate and global glaciations throughout the evolution and of the Earth. *Earth Planets Space*, 59:293–299, 2007. doi: 10.1186/BF03353107.

E. Tajika. Analysis of carbon cycle system during the neoproterozoic: Implication for snowball Earth events. In G. S. Jenkins, M. A. S. McMenamin, C. P. McKay, and L. Sohl, editors, *The Extreme Proterozoic: Geology, Geochemistry, and Climate*, chapter Analysis of carbon cycle system during the Neoproterozoic: implication for snowball Earth events, pages 45–54. Wiley-Blackwell, 2013. doi: 10.1029/146GM05.

E. Tajika and T. Matsui. Evolution of terrestrial proto-CO_2 atmosphere coupled with thermal history of the Earth. *Earth and Planetary Science Letters*, 113: 251–266, 1992. doi: 10.1016/0012-821X(92)90223-I.

E. Tajika and T. Matsui. Evolution of seafloor spreading rate based on ^{40}Ar degassing history. *Geophysical Research Letters*, 20(9):851–854, 1993a. doi: 10.1029/93GL00731.

E. Tajika and T. Matsui. Degassing history and carbon cycle of the earth: From an impact-induced steam atmosphere to the present atmosphere. *Lithos*, 30(3-4): 267–280, 1993b. doi: 10.1016/0024-4937(93)90040-J.

C. A. Tout, O. R. Pols, P. P. Eggleton, and Z. Han. Zero-age main-sequence radii and luminosities as analytic functions of and mass and metallicity. *Monthly Notices of the Royal Astronomical Society*, 281(1):257–262, 1996. doi: 10.1093/mnras/281.1.257.

D. L. Turcotte and G. Schubert. *Geodynamics*. Cambridge University Press, New York, 2nd. edition, 2002. doi: 10.1017/cbo9780511807442.

J. Veizer and S. L. Jansen. Basement and sedimentary recycling and continental evolution. *The Journal of Geology*, 87(4):341–370, 1979. doi: 10.1086/628425.

C. Vérard, C. Hochard, P. O. Baumgartner, G. M. Stampfli, and M. Liu. Geodynamic evolution of the Earth over the Phanerozoic: Plate tectonic activity and palaeoclimatic indicators. *Journal of Palaeogeography*, 4(2):167–188, 2015. doi: 10.3724/sp.j.1261.2015.00072.

A. Voigt, D. S. Abbot, R. T. Pierrehumbert, and J. Marotzke. Initiation of a Marinoan snowball Earth in a state-of-the-art atmosphere-ocean general circulation model. *Climate of the Past*, 7(1):249–263, 2011. doi: 10.5194/cp-7-249-2011.

T. Volk. Feedbacks between weathering and atmospheric CO_2 over the last 100 million years. *American Journal of Science*, 287(8):763–779, 1987.

M. P. Vukalovich and V. V. Altunin. *Thermophysical Properties of Carbon Dioxide*. Wellingborough, Collets, 1968.

J. C. G. Walker, P. B. Hays, and J. F. Kasting. A negative feedback mechanism for the long-term stabilization of Earth's surface temperature. *Journal of Geophysical Research*, 86(C10):9776–9782, 1981. doi: 10.1029/JC086iC10p09776.

S. G. Warren, W. J. Wiscombe, and J. F. Firestone. Spectral albedo and emissivity of CO_2 in martian polar caps: model results. *Journal of Geophysical Research*, 95(B9):14717–14741, 1990. doi: 10.1029/JB095iB09p14717.

S. A. Wilde, J. W. Valley, W. H. Peck, and C. M. Graham. Evidence from detrital zircons for the existence of continental crust and oceans on the Earth 4.4 Gyr ago. *Nature*, 409(6817):175–178, 2001. doi: 10.1038/35051550.

D. M. Williams and J. F. Kasting. Habitable planets with high obliquities. *Icarus*, 129(1):254–267, 1997. doi: 10.1006/icar.1997.5759.

J. T. Wilson. Did the atlantic close and then re-open? *Nature*, 211(5050):676–681, 1966. doi: 10.1038/211676a0.

M. Yoshida and M. Santosh. Supercontinents, mantle dynamics and plate tectonics: A perspective based on conceptual vs. numerical models. *Earth-Science Reviews*, 105(1-2):1–24, 2011. doi: 10.1016/j.earscirev.2010.12.002.

Y. Zhang. Degassing history of earth. In *Treatise on Geochemistry*, pages 37–69. Elsevier BV, 2014. doi: 10.1016/B978-0-08-095975-7.01302-4.